Measurement of the $\psi(2S)$ Polarization in $p\bar{p}$ Collisions at $\sqrt{s} = 1.8$ TeV

by

Ching-Yuk Paul Ngan

B.S. Physics
University of Rochester

Submitted to the Department of Physics
in partial fulfillment of the requirements for the degree of

Doctor of Philosophy

at the

MASSACHUSETTS INSTITUTE OF TECHNOLOGY

February 2001

© Ching-Yuk Paul Ngan, MMI. All rights reserved.

Author . . . .
Department of Physics
September 20, 2000

Certified by . . . .
Paris Sphicas
Professor
Thesis Supervisor

Accepted by . . . .
Thomas J. Greytak
Professor
Associate Department Head for Education

Measurement of the $\psi(2S)$ Polarization in $p\bar{p}$ Collisions at
$\sqrt{s} = 1.8$ TeV

by

Ching-Yuk Paul Ngan

Submitted to the Department of Physics
on September 20, 2000, in partial fulfillment of the
requirements for the degree of
Doctor of Philosophy

Abstract

We present a measurement of the polarization of $\psi(2S)$ mesons produced in p p̄ col-
lisions at $\sqrt{s} = 1.8\,\text{TeV}$ with the CDF detector at Fermilab. This measurement is a
sensitive test of the calculations based on the Non-relativistic QCD (NRQCD) fac-
torization mechanism, which are able to account for the unexpectedly large cross
section for charmonium production in p p̄ collisions (roughly a factor 50 above the
Color Singlet Model). These calculations also predict that directly produced char-
monia should approach 100% transverse polarization for high transverse momentum
of the onium state. We consider $\psi(2S)$ mesons, reconstructed using the decay mode
$\psi(2S) \to \mu^+\mu^-$ in a $110\ \text{pb}^{-1}$ data sample of p p̄ collisions. The polarization of prompt
$\psi(2S)$ is extracted to be $-0.54 \pm 0.48(stat.) \pm 0.04(syst.)$ for $9 < P_T(\psi(2S)) < 20$
GeV/c.

Thesis Supervisor: Paris Sphicas
Title: Professor

Acknowledgments

I would like to thank my advisor, Paris Sphicas, for his guidance and support. His leadership and wisdom have benefited my thesis research greatly. I am also grateful for the freedom and independence he entrusted me throughout my graduate career. I would like to thank Sham Sumorok and Gerry Bauer for their invaluable assistance to the analysis. They deserve a great deal of credit for the completion of this work.

Many thanks to my CDF collaborators, especially to the members of the B physics group. Jonathan Lewis, Michael Schmidt, Barry Wicklund, Joe Kroll, and Manfred Paulini have made comments and suggestions that contributed to the improvement of this analysis.

It was a privilege to be a part of the CDF-MIT group. Troy, Petar, Tushar, Jeff, Dejan, Ken, Wasiq, Andreas, Konstantin, Sasha, Ivan, Michael, Ilya, Steve, Christoph, and Frank have made my life at Fermilab easier and more enjoyable.

I would like to thank Peggy Berkovitz, Pat Solakoff, Larry Rosenson, Steve Pavlon, Roger Gaul, Sandra Fowler, and Carol Picciolo for their assistance in administrative and academic matters.

I would like to thank Tom Ferbel, who introduced me to high energy physics ten years ago. His care and support, even after I graduated from college and moved on to graduate school, is greatly appreciated.

I am grateful to Ling-Cherd, John, KK, Paul, Ming-Jer, Jianming & Li, Thomas, Kin, Leonel, Peter, Man-Fai, Jenny, Brian, and Jimmy for their friendship and kindness.

I would like to thank the congregations of the Wheaton Chinese Alliance Church and the Chinese Evangelical Church of Metropolitan Boston for their love and support. I will always remember the fellowship in Feiyang, BCBSG, and HKSBS.

Highest gratitude to the One who created the universe and makes the study of His creation in the most fundamental level more meaningful.

I am indebted to my family for their love, encouragement, and support. To my parents, Pei-Tzeng & Lai-Fai, I dedicate this thesis.

Contents

List of Figures

9

13

List of Tables

Chapter 1

Phenomenology of Charmonium Production in $p\bar{p}$ Collisions

1.1 Introduction

The "Standard Model" is the currently accepted theory of elementary particles and their interactions. In particular, the strong force that binds quarks into hadrons is described by Quantum Chromodynamics (QCD). The cross section of hadron production can thus be calculated in the framework of QCD. Several years ago, however, the prompt production cross section of ψ' measured by the CDF collaboration was found to be about 50 times larger than the QCD-based prediction (Color Singlet Model). This has been known as the "CDF ψ' Anomaly". One of the leading explanations proposed for the anomaly is the Non-relativistic QCD (NRQCD) factorization mechanism. It succeeds in describing the data, with the caveat that several free parameters need to be input from experiment. On the other hand, it also predicts ψ' to be transversely polarized at large transverse momentum. Therefore, measuring the polarization of ψ' is a test of the NRQCD factorization mechanism.

This thesis reports a measurement of the ψ' polarization, a first measurement of the polarization of a quarkonium state at the Tevatron. In this chapter, we review the phenomenology of charmonium production in $p\bar{p}$ collisions and the motivation

for polarization measurements of the ψ mesons[1]. The next chapter summarizes the relevant parts of the Fermilab accelerator and the CDF detector. The various analysis components for the polarization measurement are described in Chapters 3-6. We present the results in Chapter 7.

1.1.1 The Discovery of the ψ Meson

Before 1974, there were only three known quarks: u, d, and s. This changed with the "November Revolution" when experiments at Brookhaven[1] and SLAC[2] found evidence of a narrow resonance with a mass of about 3.1 GeV/c^2. The Brookhaven group called the new particle "J", while the SLAC group called it "ψ". Nowadays, "J/ψ" is commonly used as the name of this particle.

The extreme narrowness of the J/ψ ruled out any possibility of explaining it in terms of the known quarks. Thus, it was soon interpreted as the lowest bound states of a new quark and its anti-quark, $c\bar{c}$. This new fourth quark, c (for charm), had in fact been postulated some years before by Glashow, Iliopoulos, and Maiani[3], in connection with the nonexistence of strangeness-changing neutral weak currents.

Two weeks after observing the first resonance, the SLAC group reported a second resonance at 3.7 GeV/c^2[4]. This was later determined to be a radial excitation, now called the ψ' or $\psi(2S)$. This and other $c\bar{c}$ bound states are referred to using the generic name "charmonium".

1.1.2 Charmonium States

Charmonia are bound states of a charm quark and its anti-quark. They are "atoms" of the strong force which is described by Quantum Chromodynamics (QCD). The internal dynamics of the charmonium system is similar to the hydrogen atom or the positronium system. Thus the charmonium states can be classified using the spectroscopic notation $n\,^{2S+1}L_J$. This notation represents a charmonium state[2] with

---

[1] In this thesis, ψ is used as a generic symbol for both J/ψ and $\psi(2S)$ mesons.

[2] As will be discussed in the next section, the $c\bar{c}$ pair before binding to form a charmonium state can carry a color quantum number. Thus a superscript in parenthesis is needed to indicate the two

the principal quantum number n, the spin S, the orbital angular momentum L, and the total angular momentum J. The different orbital angular momentum states are referred to as S, P, D,... waves for $L = 0, 1, 2, ...$ The η_c is the lightest charmonium state, where the $c\bar{c}$ pair is in an S-wave state and the quark spins anti-parallel, i.e. $S = 0$. The next higher state is the J/ψ. This is the S-wave state with parallel spins. Its excited states are denoted by $\psi(nS)$ or ψ', ψ'', ... The P-wave states with parallel spins are denoted as χ_{cJ}, where $J = 0, 1, 2$. χ_c is a generic term that refers to any of the χ_{cJ}. The mass spectrum of the various charmonium states is shown in Figure 1-1.

CHARMONIA MASS SPECTRUM
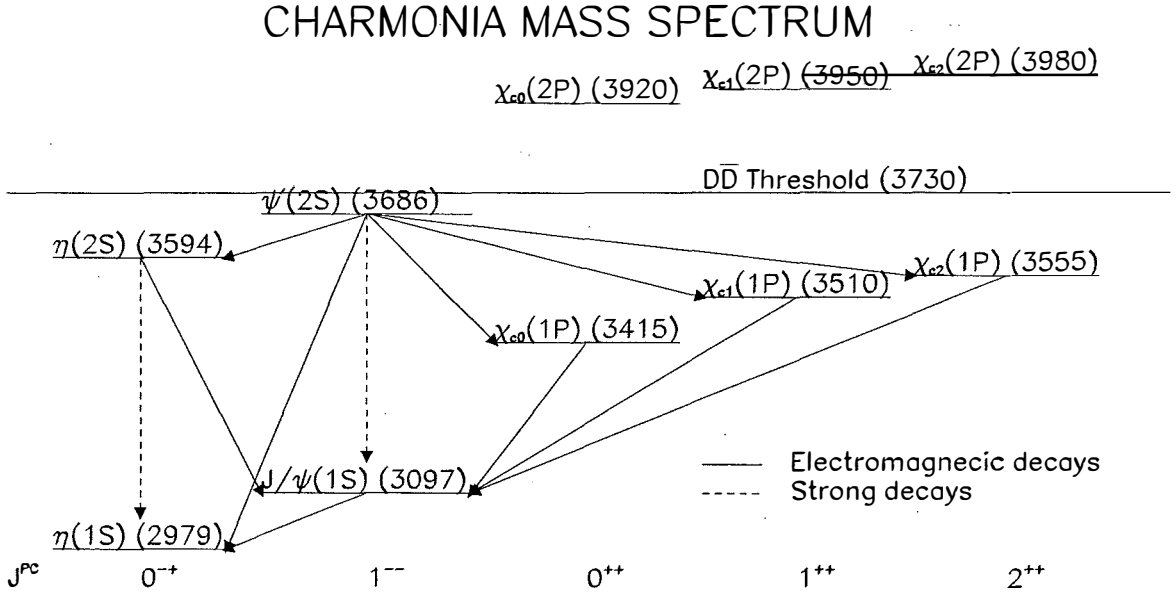
Figure 1-1: The mass spectrum of the charmonium states.

In QCD, the total angular momentum J, the parity P, and the charge conjugation C are exactly conserved quantum numbers. Hence the charmonium states can also be labeled by the quantum numbers J^{PC}. Parity inverts the coordinate system so that a vector $\vec{r}$ becomes $-\vec{r}$. Charge conjugation is the act of replacing every particle with its anti-particle. For mesons[3], $P = (-1)^{L+1}, C = (-1)^{L+S}$, where S and L

possible color states of a $c\bar{c}$ pair: [1] for color-singlet and [8] for color-octet.

[3]Mesons are strongly interacting particles built from quark-antiquark pair. Since quarks have

are the spin and the orbital angular momentum respectively. The conservation of these quantum numbers in the strong interaction has implications for the production and decay of the charmonium states. For example, the conservation of the charge conjugation governs the number of gluons a charmonium state can couple to. Since a gluon has a negative charge conjugation number, a state consisting of N gluons has $C = (-1)^N$. Thus, the χ_c, with even charge conjugation, can only couple to states with an even number of gluons, while the ψ, with odd charge conjugation, only couples to states with an odd number of gluons. In the latter case, the fact that the ψ is in a color-singlet state, implies that the minimum number of gluons it can couple to is three. This will have important effects on the relative rates of production for different charmonium states.

Charmonium mesons are easy to reconstruct in their leptonic decay signature. CDF has reconstructed a large sample of J/ψ's using the decay mode $J/\psi \rightarrow \mu^+\mu^-$. The statistics for the $\psi(2S)$ is nevertheless more limited due to its smaller production cross section and lower leptonic branching fraction: $Br(\psi \rightarrow \mu^+\mu^-)$ is 6% for J/ψ, but only 0.8% for $\psi(2S)$ [5].

1.2 Charmonium Production in $p\bar{p}$ Collisions

Much progress has been made in understanding the production of charmonium in high energy hadronic collisions in the last decade[4]. Specifically, the anomalously large cross sections for ψ mesons observed by the CDF Collaboration[7, 8] triggered a lot of theoretical interest. The inadequacy of the Color Singlet Model and the importance of the fragmentation mechanism were confirmed. Subsequently, the significance of the contributions from color-octet states was realized and included in an effort to reconcile the predictions with the data.

The production of charmonium mesons in $p\bar{p}$ collisions at the center of mass energy

---

half-integral spin, it follows that the mesons are characterized by integral spin. Charmonia, consisting of $c\bar{c}$ pair, are mesons.

[4]A recent review article on the production of heavy quarkonium in high-energy colliders can be found in Ref.[6].

of $\sqrt{s} = 1.8$ TeV at the Tevatron can be separated into two categories. One is those that come from the weak decay of b flavored hadrons. The other is prompt production that comes either directly from QCD processes, or indirectly through cascade decays from higher charmonium states which were also produced from direct QCD processes. This second mechanism is called "prompt" because the point at which a charmonium state is produced cannot be resolved experimentally from the primary vertex, the interaction point of the colliding $p\bar{p}$ beams. On the other hand, charmonia from B decays are characterized by displaced secondary vertices. This is because at the energy scale of the Tevatron, B hadrons are produced with considerable transverse momenta and will travel detectable distances before decaying weakly. Using a silicon vertex detector, these two categories can be separated experimentally by their different decay length distributions.

In the following, the phenomenology of charmonium production, both prompt and B-decay, in $p\bar{p}$ collisions is reviewed.

1.2.1   Prompt Production

Prompt charmonium is produced essentially at the $p\bar{p}$ collision point. In some charmonium states, the prompt production can be further sub-divided into two components: direct and indirect. The former is produced directly via the strong interaction, whereas the latter comes from the decay of a heavier charmonium state. For example, in addition to the direct component, prompt J/ψ also has feed-down due to decays of directly produced heavier states such as χ_c and $\psi(2S)$ mesons. The feed-down, about 30% from χ_c and 10% from $\psi(2S)$, need to be either removed or accounted for when making comparisons between data and theoretical predictions. On the other hand, $\psi(2S)$ does not have the complications of feed-down from excited states and is therefore a clean channel to study the production mechanisms of prompt charmonium.

Previous predictions for direct production of charmonium mesons were based on the Color Singlet Model. However, they underestimate the production cross sections by more than an order of magnitude when compared to the measurement by CDF. This led to the realization of the significance of fragmentation at high P_T. Recently,

calculations based on the non-relativistic QCD (NRQCD) factorization formalism are able to account for the observed cross sections by including the color-octet production mechanism. Other alternate models include the Color Evaporation Model. All of these models predicate on the factorization of charmonium production into a two-step mechanism: the perturbative production of a $c\bar{c}$ pair from hard scattering, followed by the non-perturbative binding of the $c\bar{c}$ pair into a charmonium state.

1.2.1.1   Color Singlet Model

As its name suggests, the Color Singlet Model (CSM)[9] requires the $c\bar{c}$ pair from the perturbative production to be in a *color-singlet* state. At the Tevatron, the leading order diagram for the production of a $c\bar{c}$ pair is via gluon fusion, $gg \rightarrow c\bar{c}+g$, as shown in Figure 1-2. In order to conserve both the color quantum number and G parity, the
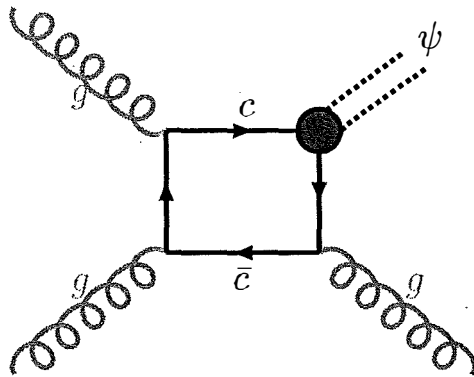
Figure 1-2: Leading order Feynman diagram for ψ production from gluon fusion.

$c\bar{c}$ pair must be attached to three gluons. Such a $c\bar{c}$ pair is characterized by a spatial separation of order $1/m_c$ or smaller, which is essentially point-like when compared with the length scale associated with the charmonium wave-function. Therefore, the amplitude for this *short-distance* part can be calculated using perturbative QCD. All the non-perturbative dynamics associated with the hadronization of the $c\bar{c}$ pair into a charmonium state can be absorbed into the wave-function factors. No gluons with energy less than $\mathcal{O}(m_c)$ in the charmonium rest frame are emitted. Thus, the

inclusive differential cross sections for producing ψ and χ_{cJ} can be expressed as

$$d\sigma(\psi + X) = d\hat{\sigma}(c\bar{c}(^3S_1^{(1)}) + X)|R_\psi(0)|^2, \qquad (1.1)$$

$$d\sigma(\chi_{cJ} + X) = d\hat{\sigma}(c\bar{c}(^3P_J^{(1)}) + X)|R'_{\chi_c}(0)|^2, \qquad (1.2)$$

where $^3S_1^{(1)}$ and $^3P_J^{(1)}$ are the spectroscopic notation[5] for the color singlet angular momentum states. $R_\psi(0)$ is the non-relativistic radial wave-functions at the origin for ψ, while $R'_{\chi_c}(0)$ is the derivative of the non-relativistic radial wave-functions at the origin for χ_c. Such non-perturbative parameters can be determined from decays of charmonium states. For example, $R_\psi(0)$ can be calculated from the ψ electronic width:

$$\Gamma(\psi \rightarrow e^+e^-) \approx \frac{4\alpha^2}{9m_c^2}|R_\psi(0)|^2. \qquad (1.3)$$

Thus the CSM can predict the absolute production rates of charmonium states.

When compared to the differential cross sections for prompt ψ measured by the CDF Collaboration[7, 8], however, the predictions from the Color Singlet Model at lowest order in α_s failed dramatically. In particular, the predictions fall almost two orders of magnitude below the data at large transverse momentum P_T[6].

From a phenomenological point of view, the CSM has several shortcomings. First, the factorization assumption implicit in Equations (1.1) and (1.2) may no longer hold when higher order radiative corrections are included. In fact, in the case of P-waves, the radiative corrections contain infrared divergences that cannot be factored into $|R'_{\chi_c}(0)|^2$[10]. The CSM also neglects relativistic corrections and excludes color octet states from contributing to charmonium production.

---

[5]The spectroscopic notation $^{2S+1}L_J^{(1,8)}$ represents the angular momentum state of a $c\bar{c}$ pair with the spin S, the orbital angular momentum L, and the total angular momentum J. The superscript in parenthesis indicates the two possible color states of a $c\bar{c}$ pair with [1] for color-singlet and [8] for color-octet.

1.2.1.2 Fragmentation

In 1993, Braaten and Yuan[11] realized that heavy quarkonium at *large* transverse momentum (P_T) is produced primarily by fragmentation[6]. Fragmentation refers to the process for the formation of a hadron from a high P_T parton $(q, \bar{q}$ or $g)$. At the Tevatron, the dominant process is through gluon fragmentation[7], $gg \to g^*g$ with $g^* \to c\bar{c}(^3S_1^{(1)}) + gg$, shown in Figure 1-3. This diagram is of $\mathcal{O}(\alpha_s^5)$, two orders in α_s higher than the gluon fusion process discussed in the previous section. However, it turns out at high $P_T(\gg m_c)$, this diagram is enhanced by a factor of $(P_T/m_c)^2$.
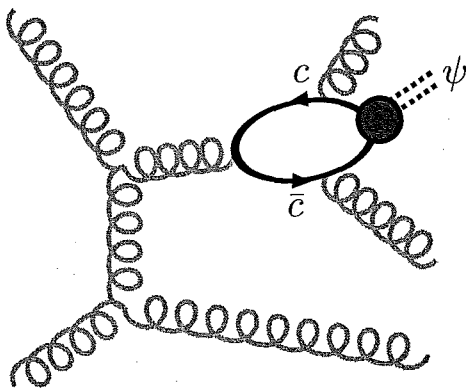
Figure 1-3: Leading order Feynman diagram for ψ production from gluon fragmentation.

The fragmentation mechanism of charmonium production is based on the factorization theorem of perturbative QCD [12]. It states that a diagram contributing to the inclusive cross section can be divided into a hard scattering sub-diagram and a soft hadronization sub-diagram. The hard part contains hard partons that have jet-like sub-diagrams and the soft part includes soft gluon lines that can couple to any of the jet-like sub-diagrams. After summing over all possible connections of the soft gluons,

---

[6]Historically, the realization of the significant role of fragmentation in charmonium production at high P_T came after the Color Singlet Model. However, it has become common that when people refer to the predictions from Color Singlet Model, the contribution from the fragmentation mechanism is also included.

[7]Charm quark fragmentation is also possible, but its contribution is much smaller at the energy scale of the Tevatron.

it turns out the effects of the soft part cancel in such a way that its contribution to the inclusive cross section can be factored into fragmentation functions.

Mathematically, the asymptotic form of the inclusive differential cross section for producing a hadron H with momentum P in $p\bar{p}$ collisions is

$$d\sigma(p\bar{p} \to H(P) + X) = \sum_{ijk} \int_0^1 dx_j F_{j/p}(x_j) \int_0^1 dx_k F_{k/\bar{p}}(x_k)$$

$$\times \int_0^1 dz d\hat{\sigma}(jk \to i(P/z) + X) D_{i \to H}(z), \qquad (1.4)$$

where $F_{j/p}$ and $F_{k/\bar{p}}$ are structure functions describing the densities of partons j and k for the colliding p and $\bar{p}$, $d\hat{\sigma}$ is the differential cross section for producing a parton i with momentum P/z in the parton subprocesses $j + k \to i + X$, and $D_{i \to H}(z)$ is the fragmentation function. The sum extends over all partons i, j and k which run over $q, \bar{q}$ and g. The parton cross section $d\hat{\sigma}$ can be calculated using perturbative QCD. All the non-perturbative dynamics involved in the formation of the hadron H is contained in the fragmentation function $D_{i \to H}(z)$, which gives the probability for a parton i to form a hadron H with momentum fraction z. The factorization theorem states that fragmentation functions are independent of the perturbative process that produces the fragmenting partons. Therefore one can, for example, use the fragmentation functions determined from e^+e^- annihilation data, to predict the production rate of the hadron H in jets produced in $p\bar{p}$ collisions. In the case of charmonium production, the fragmentation functions can also be calculated either analytically or numerically using perturbative QCD[11]. Equation (1.4) holds to all orders in perturbation theory.

As mentioned in the previous section, the radiative corrections for P-waves contain infrared divergences. Such divergences cause problems in calculating the fragmentation functions since the fragmentation contributions $(g \to c\bar{c}(^3P_J^{(1)}) + g)$ appear as next-to-leading order corrections for χ_c. To remedy this problem, the contributions from color-octet states have to be included. This will be discussed in more detail in the next section.

A comparison of the direct $\psi(2S)$ cross section measured by the CDF Collaboration[8] and the predictions of the Color Singlet Model with the fragmentation mechanism included[13] is shown in Figure 1-4 (b). Whereas adding the fragmentation contribu-

tion enhances the production rate at high P_T, the data still exceeds the predicted rate by factors of 50 to 100. This striking disagreement is commonly referred to as the "CDF ψ' anomaly." A similar discrepancy is also found in the case of J/ψ after the contribution from χ_c feed-down is removed, as shown in Figure 1-4 (a). Apparently, the CSM is not sufficient to account for the direct production of charmonia.
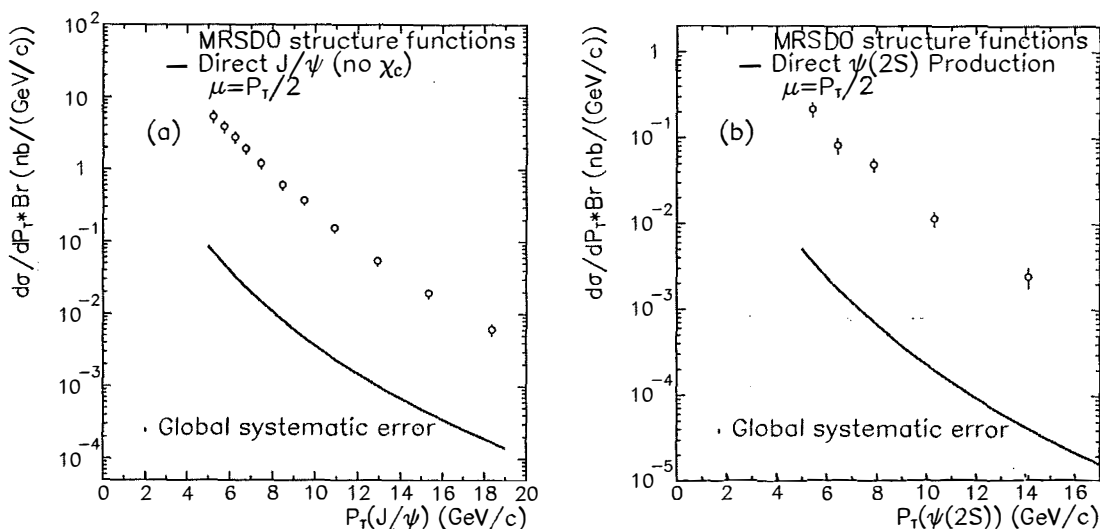
Figure 1-4: Direct J/ψ (a) and $\psi(2S)$ (b) cross sections from CDF data, compared to the predictions from the CSM with fragmentation mechanism included. The χ_c contribution to the J/ψ cross section has been removed.

In summary, at the Tevatron the direct charmonium production at small P_T was thought to be dominated by short distance processes because fragmentation processes are suppressed by powers of α_s. At sufficiently large P_T, fragmentation processes would dominate as they are enhanced by powers of $(P_T/m_c)^2$. The crossover point between the two for ψ is estimated to be at $P_T \approx 2m_\psi$[11].

1.2.1.3 Color Octet and Factorization Approach within Non-relativistic QCD (NRQCD)

The color-octet production mechanism[8] predicates that a $c\bar{c}$ pair produced in the hard scattering can be in a *color-octet* state, before binding to form a colorless charmonium meson. The non-perturbative transition of the $c\bar{c}$ pair from a color-octet state to a color-singlet state is achieved by radiating a soft gluon during hadronization.

The color-octet mechanism was first applied to the decay and production of the P-wave charmonium states[15]. As noted in Section 1.2.1.1, the radiative corrections contain logarithmic infrared divergences that cannot be factored into $|R'_{\chi_c}(0)|^2$. Such a divergence arises when a soft gluon radiates from either the c or the $\bar{c}$ that form the color-singlet ^3P_J bound state. Using the color-octet mechanism, the divergence can be factored into a matrix element $\langle \mathcal{O}_8^{\chi_c} \rangle$ that is proportional to the probability for a point-like $c\bar{c}$ pair in a color-octet $^3S_1$ state to form χ_c plus anything. Therefore, for perturbative consistency, a color-octet term should be added to Equation (1.2) of the Color Singlet Model.

As mentioned in Section 1.2.1.1, another shortcoming of the Color Singlet Model is that it does not take relativistic corrections into account. Potential model calculations indicate that v^2 is about $\frac{1}{3}$ for charmonium, where v is the typical relative velocity of the c and $\bar{c}$ in charmonium. Given v^2 is numerically of the same order as α_s, relativistic corrections suppressed by powers of v^2 may not be negligible. Understanding the structure of the relativistic corrections to charmonium production requires unraveling the different energy scales in the problem. Apart from the charm quark mass scale m_c, a charmonium bound state involves three lower scales: $m_c v$, the typical momentum of the charm quark or the inverse charmonium size; $m_c v^2$, the scale of binding energies, and Λ_{QCD}, the scale of non-perturbative effects in QCD. A powerful tool to keep track of this scale hierarchy is non-relativistic QCD (NRQCD)[16]. NRQCD is an effective field theory in which the heavy quark and anti-quark are

---

[8]In the past, people used to call this production mechanism the "Color Octet Model". Recently, such predictions are more commonly referred to as the "NRQCD factorization formalism". See Ref.[14] for a theorist's viewpoint on this.

treated non-relativistically. In 1995, Bodwin, Braaten, and Lepage[17] developed a theoretical framework for inclusive quarkonium production based on NRQCD. With a double expansion in powers of α_s and v, this framework allows one to calculate both perturbative corrections to any order in α_s, and relativistic corrections to any order in v^2.

The NRQCD framework also provides a factorization formula for inclusive charmonium cross sections in which all effects of the scale m_c are separated from the effects of lower energy scales. This corresponds to a factorization of a short distance scale $1/m_c$ in which a $c\bar{c}$ pair is produced from a long distance scale $1/(m_c v^2)$ in which the $c\bar{c}$ pair binds into a charmonium. Specifically, the inclusive differential cross sections for producing a charmonium state can be expressed as

$$d\sigma(\psi + X) = \sum_n d\hat{\sigma}(c\bar{c}(n) + X)\langle \mathcal{O}_n^\psi \rangle, \tag{1.5}$$

where $d\hat{\sigma}$ is the inclusive cross section for producing a $c\bar{c}$ pair in a specific color and angular momentum state n, and $\langle \mathcal{O}_n^\psi \rangle$ is the corresponding NRQCD matrix element. The short distance part $d\hat{\sigma}$ can be calculated via a perturbation expansion in $\alpha_s(m_c)$. The long distance factor $\langle \mathcal{O}_n^\psi \rangle$ is proportional to the probability for a point-like $c\bar{c}$ pair in the state n to form a ψ meson.

The factorization formula (1.5) contains an infinite series of matrix elements $\langle \mathcal{O}_n^\psi \rangle$. But it can be truncated to a finite number of terms using the power counting (or "velocity scaling") rules[15] of NRQCD. These rules provide an order of magnitude estimate for the matrix elements which scale with powers of v. Therefore, the relative importance of the various terms in the factorization formula is determined by the order in v of the matrix element $\langle \mathcal{O}_n^\psi \rangle$ and by the order in α_s of the parton cross section $d\hat{\sigma}$. The velocity scaling[18] for the leading matrix elements of ψ and χ_c are listed in Table 1.1. One can see that in the limit $v \to 0$, the NRQCD matrix elements reduce to those of the CSM, which are in turn related to the charmonium wave function at the origin:

$$\langle \mathcal{O}_1^\psi(^3S_1) \rangle = \frac{9}{2\pi}|R_\psi(0)|^2, \tag{1.6}$$

$$\langle \mathcal{O}_1^{\chi_{cJ}}(^3P_J) \rangle = (2J+1)\frac{9}{2\pi}|R'_{\chi_c}(0)|^2. \tag{1.7}$$

29

Thus, formulae (1.1) and (1.2) of the CSM are restored.

$H = \psi(1^{--})$	Color-singlet						Color-octet					
$X =$	$^1S_0$	$^3S_1$	$^1P_1$	^3P_J	$^3D_{J'}$	$^1D_2$	$^1S_0$	$^3S_1$	$^1P_1$	^3P_J	$^3D_{J'}$	$^1D_2$
NRQCD	v^8	1	v^8	v^8	v^8	v^{12}	v^4	v^4	v^8	v^4	v^8	v^{12}
CSM	0	1	0	0	0	0	0	0	0	0	0	0
$H = \chi_{cJ}(J^{++})$												
NRQCD	v^6	v^6	v^{10}	v^2	v^{10}	v^{10}	v^6	v^2	v^6	v^6	v^6	v^{10}
CSM	0	0	0	v^2	0	0	0	0	0	0	0	0

Table 1.1: Velocity scaling for leading matrix elements $\langle \mathcal{O}_c^H(X) \rangle$.

From Table 1.1, it can be seen that the leading order (in v) color-octet matrix elements for the ψ are $\langle \mathcal{O}_8^\psi(^1S_0) \rangle$, $\langle \mathcal{O}_8^\psi(^3S_1) \rangle$, and $\langle \mathcal{O}_8^\psi(^3P_J) \rangle$, all of which are suppressed by a factor v^4 relative to the leading color-singlet matrix element $\langle \mathcal{O}_1^\psi(^3S_1) \rangle$. However, Braaten and Fleming[19] observed that the color-octet terms could dominate, if the parton cross section $d\hat{\sigma}$ multiplying the color-singlet matrix element is suppressed by powers of α_s or by small kinematic parameters such as m_c^2/P_T^2. Recall from the previous section that charmonium at large P_T is produced primarily by gluon fragmentation to a color-singlet $c\bar{c}$ pair. Such a process is of $\mathcal{O}(\alpha_s^5)$. In prompt $\psi(2S)$ production, this prediction was about a factor of 30-50 below data. Braaten and Fleming proposed that gluon fragmentation to an intermediate color-octet $c\bar{c}$ pair in a $^3S_1$ state could be the missing piece. The Feynman diagram for this process is illustrated in Figure 1-5. Since the $c\bar{c}$ pair is in a color-octet state, the gluons originally attached to the $c\bar{c}$ pair to conserve color in the CSM can now be moved to the "blob" where non-perturbative hadronization takes place. This would result in an enhancement of the production cross section as those non-perturbative gluons are soft and have a large phase space. Notice this perturbative process is of $\mathcal{O}(\alpha_s^3)$, two powers of α_s less than gluon fragmentation in the CSM. Thus the color-octet term that comes with the matrix element $\langle \mathcal{O}_8^\psi(^3S_1) \rangle$ may well be numerically important. $\langle \mathcal{O}_8^\psi(^1S_0) \rangle$ and $\langle \mathcal{O}_8^\psi(^3P_J) \rangle$ are also linked to parton cross sections that are of $\mathcal{O}(\alpha_s^4)$.

Therefore, the suppression by v^4 in the color-octet matrix elements can potentially be overcome. The relative importance of the color-singlet term versus the color-octet terms can only be assessed after determining the values of the color-octet matrix elements. Unfortunately, they can only be obtained by fitting to data.
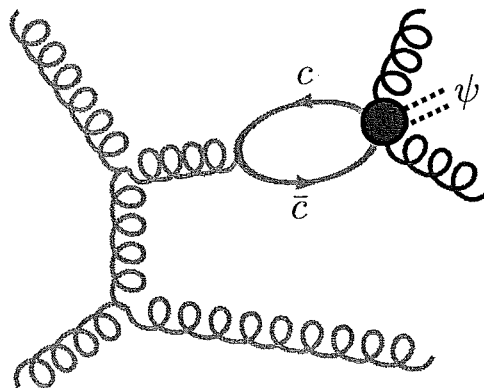
Figure 1-5: Feynman diagram for ψ production from gluon fragmentation in the color octet model. This process corresponds to the color-octet matrix element $\langle \mathcal{O}_8^\psi(^3S_1) \rangle$.

As in the CSM, Equation (1.4) can be applied to calculate the inclusive differential cross section of heavy quarkonium H through the color-octet fragmentation mechanisms. Using the NRQCD factorization approach, the fragmentation functions can be expressed in the general form

$$D_{i \to H}(z) = \sum_n d_{i \to n}(z) \langle \mathcal{O}_n^H \rangle, \tag{1.8}$$

where $d_{i \to n}(z)$ is the short-distance coefficient that can be computed perturbatively and $\langle \mathcal{O}_n^H \rangle$ is the corresponding NRQCD matrix element for a specific $c\bar{c}$ state.

Fitting the magnitudes of the differential cross sections to the CDF data[8], Cho and Leibovich[20] extracted the matrix element values:

$$\langle \mathcal{O}_8^{J/\psi}(^3S_1) \rangle = (6.6 \pm 2.1) \times 10^{-3} \text{GeV}^3 \tag{1.9}$$

$$\frac{\langle \mathcal{O}_8^{J/\psi}(^3P_0) \rangle}{m_c^2} + \frac{\langle \mathcal{O}_8^{J/\psi}(^1S_0) \rangle}{3} = (2.2 \pm 0.5) \times 10^{-2} \text{GeV}^3 \tag{1.10}$$

$$\langle \mathcal{O}_8^{\psi(2S)}(^3S_1) \rangle = (4.6 \pm 1.0) \times 10^{-3} \text{GeV}^3 \tag{1.11}$$

$$\frac{\langle \mathcal{O}_8^{\psi(2S)}(^3P_0) \rangle}{m_c^2} + \frac{\langle \mathcal{O}_8^{\psi(2S)}(^1S_0) \rangle}{3} = (5.9 \pm 1.9) \times 10^{-3} \text{GeV}^3. \tag{1.12}$$

The P_T shapes of the cross section data are well described by these fits, as can be seen in Figure 1-6 (a) and (b) for J/ψ and $\psi(2S)$ respectively. Only the linear combination $\langle\mathcal{O}_8^\psi(^3P_0)\rangle/m_c^2 + \langle\mathcal{O}_8^\psi(^1S_0)\rangle/3$ can be extracted because the differential cross sections from $^1S_0^{(8)}$ and $^3P_0^{(8)}$ have similar shapes in the transverse momentum range $5\text{GeV} \leq P_T \leq 20\text{GeV}$. These two channels are found to be significant at low $P_T(< 10\text{GeV})$[20, 21], since they fall as $d\hat{\sigma}/dP_T^2 \sim 1/P_T^6$. The contribution from $^3S_1^{(8)}$, which exhibits scaling as $d\hat{\sigma}/dP_T^2 \sim 1/P_T^4$, dominates at high P_T. For a comparison, the $^3S_1^{(1)}$ color-singlet channel at the same leading order in α_s behaves at large P_T like $1/P_T^8$. This is a much steeper fall than that observed in the data. The fitted matrix elements have magnitudes of the order 10^{-3} GeV^3. These are qualitatively consistent with the v^4 suppression relative to $\langle\mathcal{O}_1^\psi(^3S_1)\rangle$[9], as given by the NRQCD power counting rules.
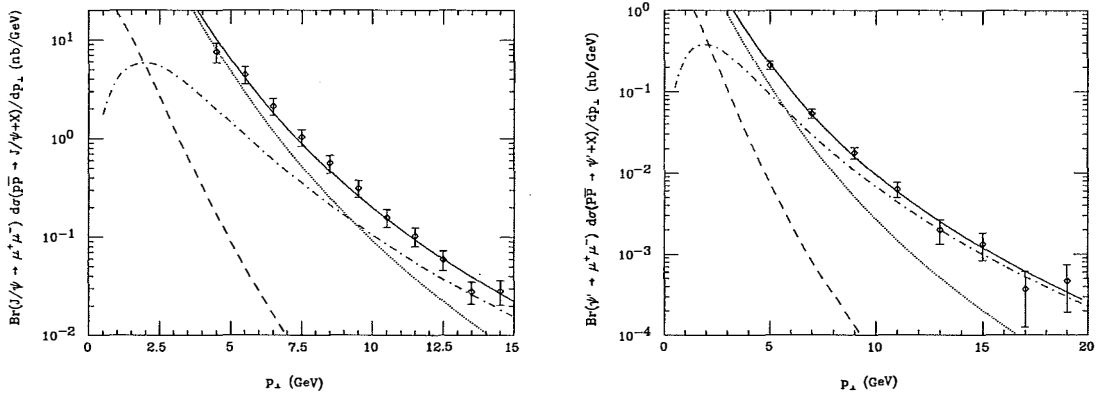
Figure 1-6: Results of fitting the theoretical predictions[20] to the direct (a) J/ψ and (b) $\psi(2S)$ differential cross sections measured by CDF. The dashed curve depicts the color-singlet contribution. The dot-dashed curve illustrates the $^3S_1^{(8)}$ component, and the dotted curve denotes the combined cross section due to $^1S_0^{(8)}$ and $^3P_0^{(8)}$. The solid curve is the sum of the color-singlet and color-octet contributions and represents the total theoretical prediction. All curves are multiplied by the branching fraction $\text{Br}(\psi \to \mu^+\mu^-)$.

---

[9]For example, the color-singlet matrix element of J/ψ is determined from its decay rates to lepton pairs to be $\langle\mathcal{O}_1^{J/\psi}(^3S_1)\rangle = 1.1 \pm 0.1$ GeV^3[22].

Further studies[23] on the extraction of the matrix elements have taken higher-order QCD effects into account. When the effective intrinsic transverse momentum (k_T) of partons due to the initial-state radiation of gluons is included, the fitted value of $\langle \mathcal{O}_8^\psi(^3P_0)\rangle/m_c^2 + \langle \mathcal{O}_8^\psi(^1S_0)\rangle/3$ is found to decrease by a factor of five whereas $\langle \mathcal{O}_8^\psi(^3S_1)\rangle$ remains the same. The choice of the parton distribution functions in the calculation can also change the fitted values of the matrix elements by as much as a factor of two.

The NRQCD factorization formalism states that the matrix elements are universal, i.e. they are the same for different production processes and energies. Therefore, the matrix elements extracted from one experiment can be used to make predictions for other experiments. Using the color-octet matrix elements extracted from CDF, Cacciari and Kraemer[24] examined the color-octet contributions to the inelastic J/ψ photoproduction, $\gamma + p \to J/\psi + X$, at the HERA ep collider. Their prediction appears to be one order of magnitude larger than the data. The discrepancy is particularly striking at large z, where z is the fraction of the photon energy transferred to the J/ψ meson in the proton rest frame. The prediction shows a distinct rise in cross section as $z \to 1$, which is not observed by the H1[25] and ZEUS[26] collaborations at HERA. Further studies show that effects such as soft-gluon resummation[27], k_T smearing[28] and the breakdown of NRQCD factorization near $z = 1$[29] can account for the discrepancy. Therefore, non-universality of the color-octet matrix elements cannot be concluded.

1.2.1.4 Color Evaporation Model

The Color Evaporation Model (CEM)[30] assumes that all $c\bar{c}$ pairs with invariant mass between $2m_c$ and the open charm threshold $2m_D$ produce charmonium states. Unlike the Color Singlet Model, the short-distance $c\bar{c}$ pair is not required to be in a color-singlet state since there is infinite time for soft gluons to readjust the color of the $c\bar{c}$ before it appears as an asymptotic ψ meson. Whereas this is similar in spirit to the NRQCD factorization formalism, the CEM ignores the hierarchy of matrix elements in the v expansion. In this model, the sum of the cross sections of all charmonium

states is given by

$$\sigma_{onium} = \frac{1}{9} \int_{2m_c}^{2m_D} dm \frac{d\sigma_{c\bar{c}}}{dm},$$ (1.13)

where the cross section for producing à $c\bar{c}$ pair, $\sigma_{c\bar{c}}$, is integrated over the invariant mass m of the $c\bar{c}$ pair up to the open charm threshold. The coefficient 1/9 accounts for the probability that the $c\bar{c}$ pair is asymptotically in a color singlet state. To determine the cross section for a specific charmonium state such as J/ψ, a free parameter ρ_ψ is introduced:

$$\sigma_\psi = \rho_\psi \sigma_{onium}.$$ (1.14)

Since ρ_ψ is not predicted in the model, the normalization of the cross section is uncertain. Nevertheless, the factor ρ_ψ is required to be a universal constant independent of the production process. It can be either extracted by fitting to data or estimated from statistical counting method. For example, ρ_ψ is determined to be ≈ 0.5 from J/ψ photo-production[31].

In general, the predictions from the CEM agree fairly well with much of the data[31]. Nevertheless, its prediction of the universality of the ratio ρ_χ/ρ_ψ is not supported by a comparison of charmonium production in fixed target collisions and photo-production[32].

1.2.2 Production from B Decays

Another major source of charmonium in $p\bar{p}$ collisions is from decays of b flavored hadrons. At the Tevatron, a b quark can be produced through several QCD processes such as gluon fusion, gluon splitting, and flavor excitation. The produced b quark then fragments into a B hadron which subsequently decays through the weak interaction into a ψ meson and other particles. The inclusive branching fractions for B hadrons decaying into ψ mesons are approximately 1.1% for J/ψ and 0.4% for $\psi(2S)$[5].

The theoretical predictions for charmonium production from B decays are based on next-to-leading order (NLO) calculations in QCD[33]. A comparison of the inclusive cross sections for charmonium production from B decays shows the data are

34

higher than the predictions by a factor of 2-4 (3-4) depending on the transverse momentum P_T of the J/ψ ($\psi(2S)$) meson[8].

A more recent calculation is able to make predictions with good agreement to data[34]. The formation of the b flavored hadrons is described in the QCD parton model with fragmentation functions fitted to e^+e^- data at LEP on B meson production[35]. The inclusive $B \to \psi + X$ decay[10] can be divided into $B \to b$ and $b \to \psi + X$. The transition $B \to b$ is described by the parton model with a structure function parametrized to the Peterson form[36]. In the NRQCD framework, the decay $b \to \psi + X$ is represented by a sum of products, each of which consists of a short-distance coefficient for the creation of a $c\bar{c}$ pair in a specific angular momentum and color state, and a non-perturbative matrix element for the hadronization of the pair to a ψ meson. As discussed in Section 1.2.1.3, the NRQCD matrix elements can be determined from fitting the CDF data sample of direct ψ hadroproduction, though only a linear combination of $\langle \mathcal{O}_8^\psi(^3P_0) \rangle$ and $\langle \mathcal{O}_8^\psi(^1S_0) \rangle$ is extracted[20]. However, it turns out by fitting the CLEO data[37] of ψ production from B decay, $\langle \mathcal{O}_8^\psi(^3P_0) \rangle$ and $\langle \mathcal{O}_8^\psi(^1S_0) \rangle$ can be extracted separately. As a result, the P_T spectra of the charmonium states from B decays are predicted. Figure 1-7 (a) and (b) show good agreement between CDF data on J/ψ and $\psi(2S)$ production from B decays and the LO and NLO predictions[34]. The theoretical uncertainty is estimated to be of order $\pm 25\%$ for $P_T \geq 13$ GeV.

1.3 Charmonium Polarization in $p\bar{p}$ Collisions

Whereas the NRQCD predictions are capable of describing the CDF data, they come with a price of introducing matrix elements which are free parameters that have to be determined from fitting to data. This means the NRQCD factorization formalism

---

[10]In the case of J/ψ, in addition to $B \to J/\psi + X$, it also has two feed-down modes: $B \to \psi(2S) + X$ followed by $\psi(2S) \to J/\psi + X$, and $B \to \chi_c + X$ followed by $\chi_c \to J/\psi + \gamma$. The contribution of the feed-down from $\psi(2S)$ and χ_c is accounted for by including the respective branching fractions and assuming that the J/ψ mesons receive the full momentum of the primary charmonium states.
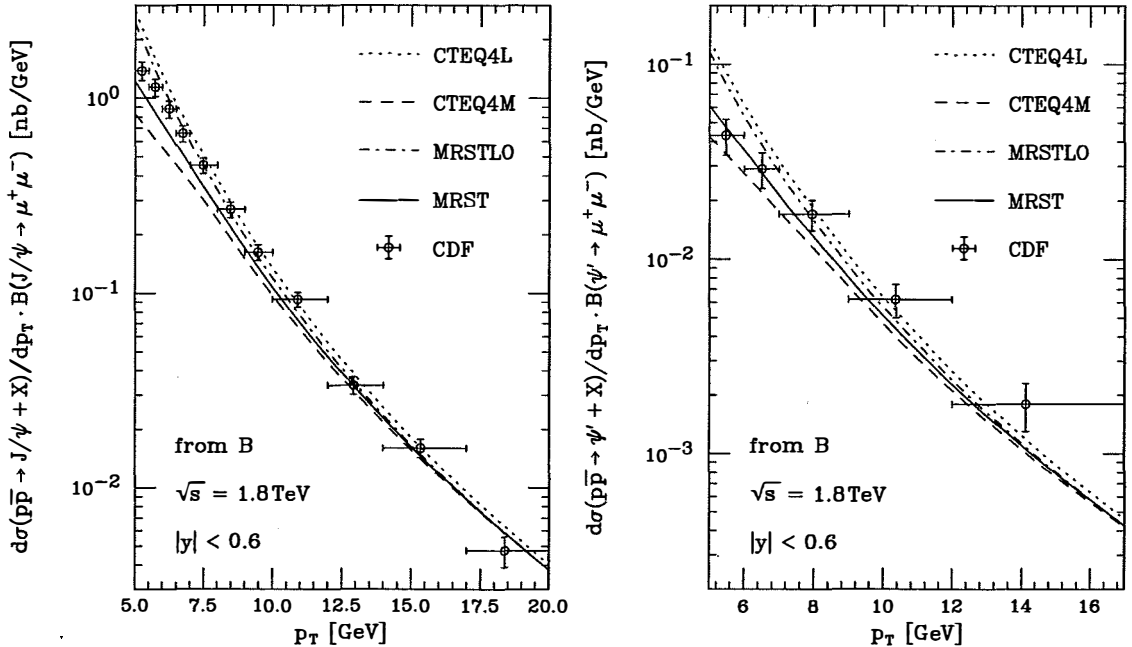
Figure 1-7: The CDF data on the inclusive hadroproduction of b hadrons decaying to (a) J/ψ and (b) $\psi(2S)$ mesons are compared with LO and NLO predictions evaluated with CTEQ4[38] and MRST[39] proton PDF's.

can predict the shape of the transverse momentum (P_T) distribution in charmonium production, but not the absolute normalization. In addition, the test of the universality of the NRQCD matrix elements extracted from the Tevatron and HERA data is, to date, not conclusive. Therefore, while the formalism looks promising, it still lacks a stringent test. The NRQCD formalism also predicts that directly produced ψ mesons are transversely polarized (helicity[11]$= \pm 1$) at large P_T. Thus, a polarization measurement of direct ψ mesons at the Tevatron will serve as a decisive test of the NRQCD factorization approach.

Besides, such a measurement would help to distinguish the different models for charmonium production. For example, one distinct feature of the Color Evaporation Model is that it predicts directly produced charmonia are essentially unpolarized[40]. This follows from the premise that the polarization information of the $c\bar{c}$ pair is lost

---

[11]Helicity is defined as the projection of the spin of a particle in the direction of its motion. Zero helicity corresponds to longitudinal polarization.

due to the multiple soft-gluon exchanges. Zero polarization is in agreement with the measurements of the ψ polarization made in fixed target experiments[41].

Experimentally, knowledge of the polarization would also help decrease the systematic uncertainties on the acceptance of ψ decays, hence improving the measurement of cross sections.

Measuring the charmonium polarization involves the study of its decay angular distribution. From spin formalism (Appendix A), the angular distribution of $\psi \to \mu^+ \mu^-$ decay is given by:

$$I(\cos \theta^*) = \frac{3}{2(\alpha + 3)}(1 + \alpha \cos^2 \theta^*),$$

where α is the polarization, and θ^* is the angle between the μ^+ three-momentum vector in the ψ rest frame and the direction of ψ in the Lab frame. Unpolarized ψ mesons would have $\alpha = 0$ whereas $\alpha = 1$ and -1 correspond to fully transverse and longitudinal polarizations. The above equation for the angular distribution applies to ψ mesons from both prompt production and B decays. In the following subsections, the NRQCD predictions on the charmonium polarizations from these two mechanisms will be discussed.

1.3.1 Polarization in Prompt Production

Recall from Section 1.2.1.3 that in the NRQCD factorization formalism, the charmonium production cross sections at large P_T are dominated by gluon fragmentation via color-octet mechanism into ${}^3S_1^{(8)} c\bar{c}$ pairs. The fragmenting gluon, being effectively on-shell at high $P_T (\gg 2m_c)$, is transversely polarized like a massless photon. The ${}^3S_1^{(8)} c\bar{c}$ pair, and subsequently the ψ mesons, inherit the gluon's polarization. This is a consequence of the heavy-quark spin symmetry of NRQCD, which implies the emission of soft gluons during hadronization does not flip the spin of a heavy quark[42]. Therefore, at leading order in α_s, the NRQCD factorization formalism predicts directly produced ψ mesons[12] to asymptotically approach 100% transverse polarization

---

[12]Recall that "prompt" and "direct" are equivalent in meaning for $\psi(2S)$, whereas "prompt" J/ψ includes both the direct production and the feed-down from excited charmonium states.

as their P_T increases.

There are three sources of corrections that can cause the breaking of the transverse polarization of ψ mesons. First, the NRQCD spin symmetry is violated when higher order (in v) terms are taken into account. Using power counting rules, Beneke and Rothstein[43] estimated corrections of $\mathcal{O}(v^4)$ could reduce α by $3-4\%$. Another source of correction comes from QCD corrections to the fragmentation function. The $\mathcal{O}(\alpha_s^4)$ fragmentation processes include contributions from LO $^1S_0^{(8)}$, $^3P_J^{(8)}$ and NLO $^3S_1^{(8)}$. Since radiation of a hard gluon can change the polarization of a $c\bar{c}$ pair, the $\mathcal{O}(\alpha_s^4)$ contributions can break the transversality of the $\mathcal{O}(\alpha_s^3)$ $^3S_1^{(8)}$ process. This correction decreases with P_T as $1/(\ln P_T)$ and is estimated to be from 6% to 4% in the range $5 < P_T < 25$ GeV[43]. Third, non-fragmentation processes can contribute to depolarization. As discussed in Section 1.2.1.3, the color-octet $^1S_0^{(8)}$ and $^3P_J^{(8)}$ production channels, which do not have a fragmentation interpretation at leading order in α_s, dominates at low $P_T(< 10\text{GeV})$. These two channels are found to have a significant longitudinal polarization fraction and therefore reduce the transverse polarization in the low P_T region[21].

Taking the depolarization effects due to QCD radiation and the non-fragmentation processes into account, Beneke and Krämer[21] calculated the polarization for directly produced ψ mesons. The matrix elements used in the calculation were extracted from the CDF cross section data. The polarization α as a function of P_T is shown in Figure 1-8. The solid curve represents the contributions from $^3S_1^{(8)}$ color-octet state only, while the shaded band is obtained from including the $^1S_0^{(8)}$ and $^3P_J^{(8)}$ channels as well. The band also reflects the statistical uncertainties in the extraction of these color-octet matrix elements. One can see that the $^1S_0^{(8)}$ and $^3P_J^{(8)}$ states reduce the polarization significantly. At low P_T, the theoretical prediction is compatible with zero polarization. As P_T increases, the polarization becomes more and more transverse. Notice that the P_T dependence of α is identical for J/ψ and $\psi(2S)$, since the ratios of their NRQCD matrix elements were fixed when fitting to data. In the case of the observed J/ψ polarization, the contributions due to χ_c and $\psi(2S)$ feed-down need to be removed when comparing data to this prediction.

polar angle asymmetry α in $\psi \to \mu^+\mu^-$

$^3S_1^{(8)}$ only

CTEQ4L

P_T (GeV)
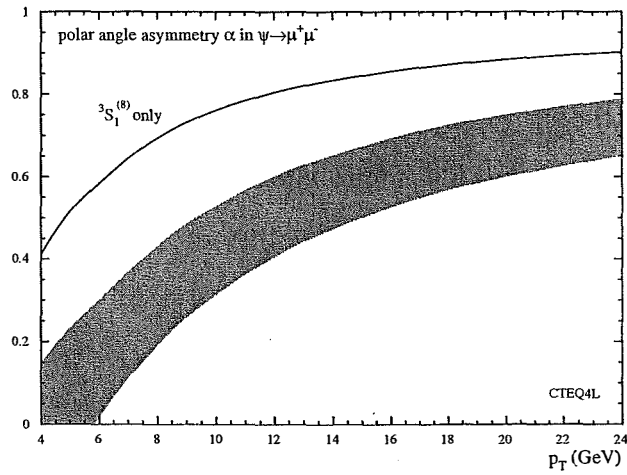
Figure 1-8: The polarization parameter α as a function of P_T for directly produced ψ mesons. Beneke and Krämer[21] derived this prediction based on the NRQCD factorization formalism. The shaded band shows unpolarized charmonium at low P_T but becomes more transversely polarized as P_T increases. The solid curve is obtained by excluding the contributions from $^1S_0^{(8)}$ and $^3P_J^{(8)}$ states. It shows the importance of depolarization effects of these states.

Recently, using the NRQCD factorization formalism, Braaten, Kniehl, and Lee[44] presented a similar calculation on the polarization of prompt charmonium. The P_T dependence of α for the $\psi(2S)$ meson is shown in Figure 1-9. A transverse polarization at large $\psi(2S)$ P_T is also predicted. In addition, Braaten and company analyzed the polarization of *prompt J/ψ* by including the contributions due to χ_c and $\psi(2S)$ feeddown. They calculated the prompt cross section $\sigma[J/\psi]$ by summing the direct J/ψ cross section and the cross sections for χ_{cJ} and $\psi(2S)$ weighted by their branching fractions of decaying into J/ψ. On the other hand, the prompt cross section $\sigma[\psi_L]$ of longitudinally polarized J/ψ is equal to the sum of the direct cross section and the cross sections for each of the spin (J) and helicity (λ) states χ_{cJ}^{λ} and $\psi(2S)^{\lambda}$ weighted by the branching fractions and by the probability for the polarized state to decay into ψ_L. The polarization can then be determined using:

$$\alpha = \frac{\sigma[J/\psi] - 3\sigma[\psi_L]}{\sigma[J/\psi] + \sigma[\psi_L]}.$$

The resulting prediction on the prompt polarization for J/ψ is shown as the shaded band in Figure 1-10. The band indicates the uncertainties obtained by combining in quadrature the errors from the color-octet matrix elements, the parton distribution functions, the renormalization and factorization scale, and the charm quark mass. Also displayed in Figure 1-10 are the polarizations for the three components of prompt J/ψ. The solid line represents the central curve of α for direct J/ψ, the dashed line for J/ψ from χ_c, and the dotted line for J/ψ from $\psi(2S)$. In the moderate P_T region, the contributions from $\psi(2S)$ and χ_c add to give an increase in the transverse polarization of prompt J/ψ compared to direct J/ψ, while they tend to cancel each other in the high P_T region. Still, a large polarization value around 0.7 for prompt J/ψ is predicted at $P_T = 20$ GeV/c.

1.3.2 Polarization from B Decays

A prediction for J/ψ polarization in B decays is provided by the authors of Ref.[45]. They calculated the amplitudes for the four-quark Fermi interactions $b \rightarrow c\bar{c}s$ and $b \rightarrow c\bar{c}d$, which describe the short-distance physics for the process $b \rightarrow J/\psi + X$.
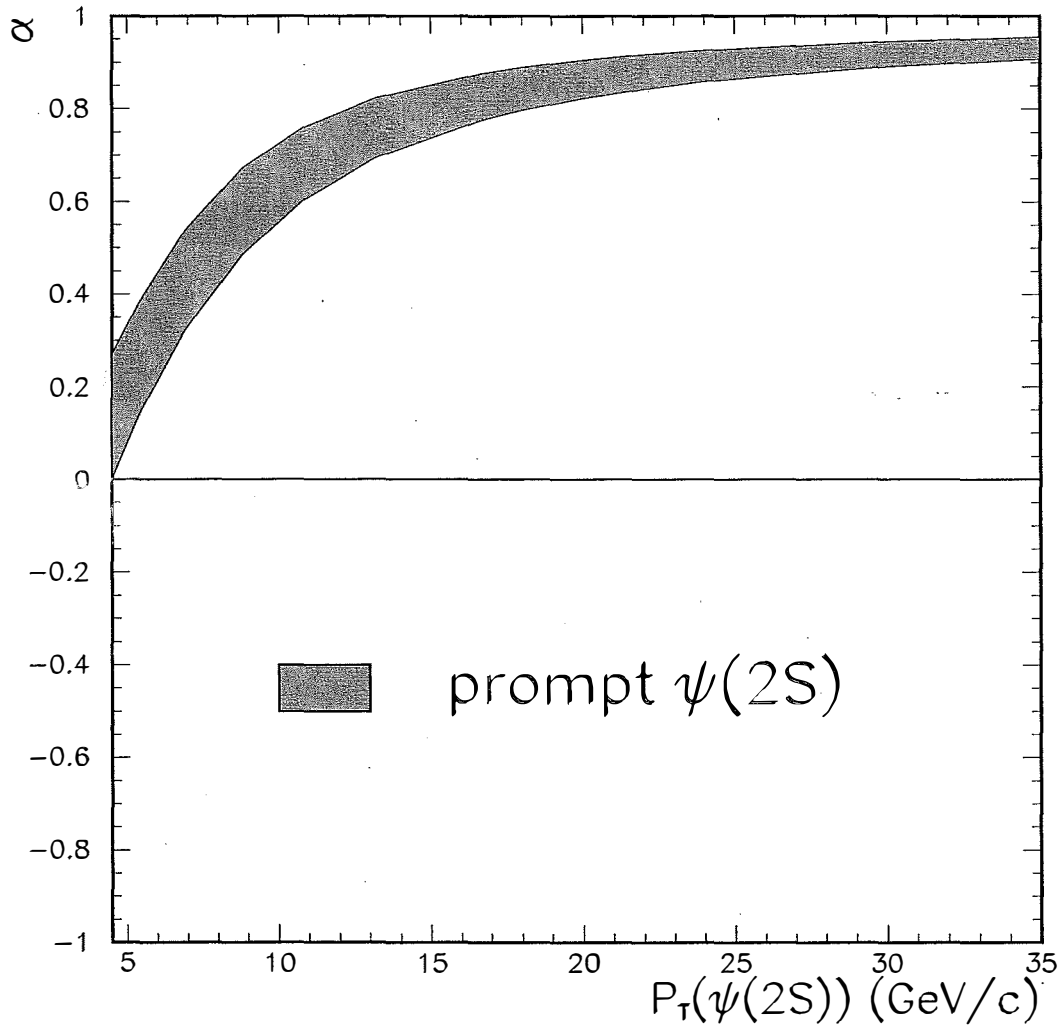
Figure 1-9: The polarization prediction for prompt (direct) $\psi(2S)$ by Braaten et al.[44]. A transverse polarization at large $\psi(2S)$ P_T is predicted. The band reflects the uncertainties due to the color-octet matrix elements, the parton distribution functions, the renormalization and factorization scale, and the charm quark mass.
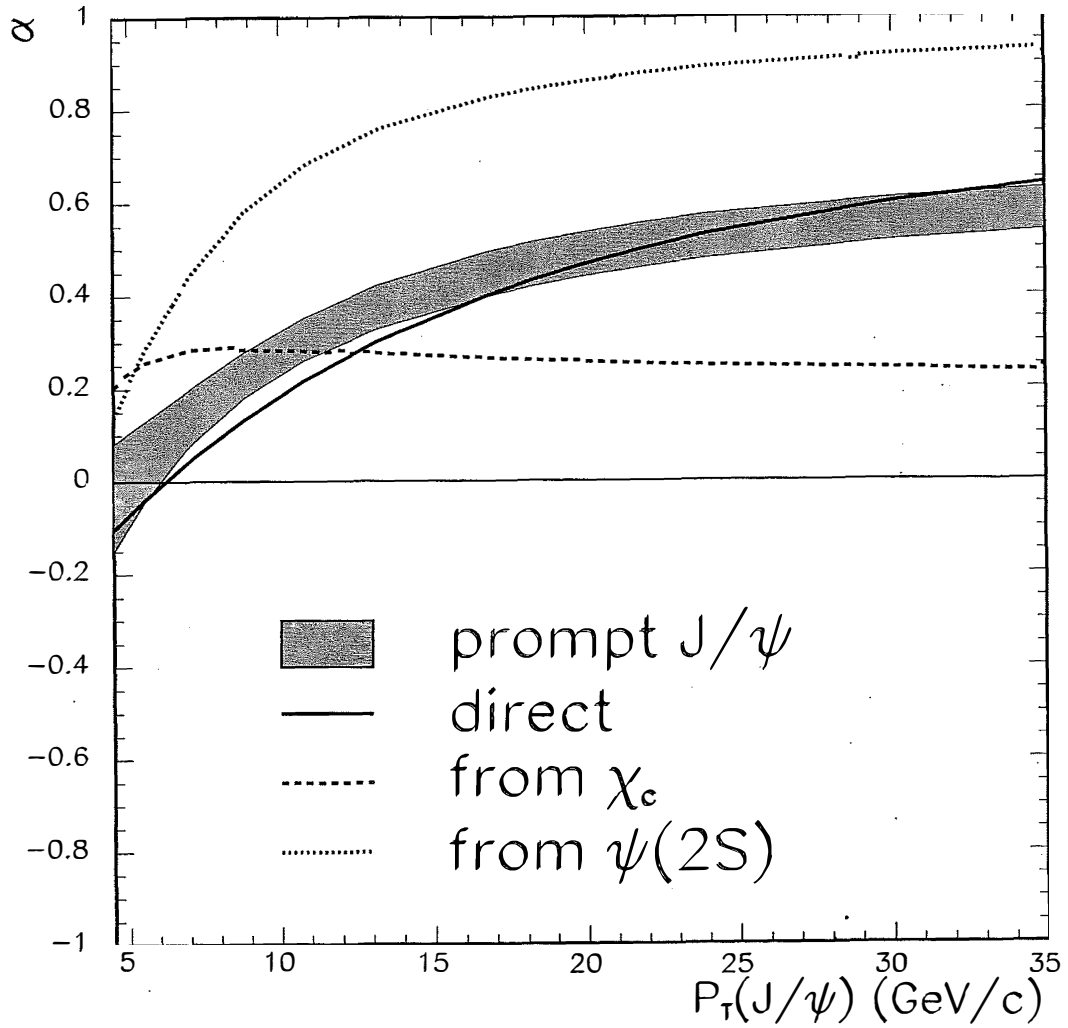
Figure 1-10: The polarization prediction for prompt J/ψ by Braaten et al.[44] is shown as the shaded band. The predicted polarizations for the three components of prompt J/ψ are also displayed. The solid line represents the central curve of α for direct J/ψ, the dashed line for J/ψ from χ_c, and the dotted line for J/ψ from $\psi(2S)$.

Using the matching procedure presented in Ref.[46], they derived the production rate of J/ψ from B decays in terms of the NRQCD matrix elements with their coefficients governed by the b quark mass (m_b), the c quark mass (m_c), and the Wilson coefficients[13] (C_+ and C_-). Subsequently, they computed the relative production rates of J/ψ with specified helicities, from which they determined the polarization.

Using the procedure described above, the authors of Ref.[45] derived the polarization parameter α in terms of the NRQCD matrix elements:

$$\alpha = \frac{-0.39\langle\mathcal{O}_1^{J/\psi}(^3S_1)\rangle - 17\langle\mathcal{O}_8^{J/\psi}(^3S_1)\rangle + 52\langle\mathcal{O}_8^{J/\psi}(^3P_0)\rangle/m_c^2}{\langle\mathcal{O}_1^{J/\psi}(^3S_1)\rangle + 44\langle\mathcal{O}_8^{J/\psi}(^3S_1)\rangle + 61\langle\mathcal{O}_8^{J/\psi}(^1S_0)\rangle + 211\langle\mathcal{O}_8^{J/\psi}(^3P_0)\rangle/m_c^2}.$$

Only the leading color-singlet and color-octet matrix elements in the relativistic v^2 expansion were considered. The numerical coefficients were obtained with $m_b = 4.7$ GeV/c^2, $m_c = 1.55$ GeV/c^2, $C_+(m_b) = 0.868$, and $C_-(m_b) \doteq 1.329$. Notice that α depends only weakly on $\langle\mathcal{O}_8^{J/\psi}(^3S_1)\rangle$ and most strongly on $\langle\mathcal{O}_8^{J/\psi}(^3P_0)\rangle/m_c^2$. Using the current experimental information and theoretical considerations on the color-octet matrix elements[5, 22, 47, 48]:

$$\langle\mathcal{O}_1^{J/\psi}(^3S_1)\rangle \in [1.0, 1.2] \text{ GeV}^3$$

$$\langle\mathcal{O}_8^{J/\psi}(^3S_1)\rangle \in [0.0016, 0.0092] \text{ GeV}^3$$

$$\langle\mathcal{O}_8^{J/\psi}(^1S_0)\rangle + 7\frac{\langle\mathcal{O}_8^{J/\psi}(^3P_0)\rangle}{m_c^2} \in [0.0, 0.095] \text{ GeV}^3$$

$$0.096\langle\mathcal{O}_1^{J/\psi}(^3S_1)\rangle + 4.21\langle\mathcal{O}_8^{J/\psi}(^3S_1)\rangle + 6.76\langle\mathcal{O}_8^{J/\psi}(^1S_0)\rangle$$

$$+ 25.3\frac{\langle\mathcal{O}_8^{J/\psi}(^3P_0)\rangle}{m_c^2} \in [0.24, 0.45] \text{ GeV}^3$$

the authors calculated the expected range of α to be $-0.33 < \alpha < 0.05$. The maximum value for $\alpha(0.05)$ is obtained when $\langle\mathcal{O}_8^{J/\psi}(^3S_1)\rangle$ is at the minimum of its allowed range and when the combination $\langle\mathcal{O}_8^{J/\psi}(^1S_0)\rangle + 7\langle\mathcal{O}_8^{J/\psi}(^3P_0)\rangle/m_c^2$ is near the maximum of its allowed range. The minimum value of $\alpha(-0.33)$ occurs in the opposite situation. On the other hand, if only the color-singlet $^3S_1$ state is taken into account, the prediction on α is -0.40 ± 0.04.

Notice that the polarization prediction discussed above is only for $B \to J/\psi X$. To date, no prediction for α of $\psi(2S)$ from B decays is available.

---

[13]Wilson coefficients govern the scale evolution of the four-quark Fermi interaction.

1.4 Outline of Measuring the $\psi(2S)$ Polarization

A polarization measurement involves the analysis of the $\cos\theta^*$ angular distribution. We start by introducing, in the next chapter, the relevant features of the experimental apparatus that produce and detect the $\psi(2S)$ mesons. Chapter 3 describes the reconstruction of the $\psi(2S)$ candidates from a dimuon data sample. To study the transverse momentum (P_T) dependence of polarization, we divide the data sample into three $\psi(2S)$ P_T ranges. Each sample is further divided into two sub-samples based on the $\psi(2S)$ lifetime (ct) distribution: a prompt enriched low ct sample and a B-decay dominated high ct sample. The $\cos\theta^*$ angular distributions are extracted by fitting the invariant mass distributions of the dimuons in $\cos\theta^*$ bins. Chapter 4 discusses how the $\cos\theta^*$ acceptance and efficiencies are determined using Monte Carlo methods. Chapter 5 details an analysis of the $\psi(2S)$ lifetime distribution to determine the relative fractions of the prompt and B-decay components in the data samples. As will be discussed in Chapter 6, an iterative χ^2 fit of the $\cos\theta^*$ distributions is performed to extract the polarization of the promptly produced $\psi(2S)$ mesons and those from B decays. The results are presented in Chapter 7.

Chapter 2

Experimental Apparatus

This chapter describes the experimental apparatus used in this analysis. Charmonium mesons are produced in proton-antiproton collisions with the Tevatron, at the Fermi National Accelerator Laboratory (FNAL or Fermilab). The Tevatron is currently the highest energy collider, colliding proton and antiproton beams at a center of mass energy of $\sqrt{s} = 1.8$ TeV. The decay products of the charmonia were detected in the Collider Detector at Fermilab (CDF). CDF is a general purpose detector, built to study the $p\bar{p}$ interactions with large transverse momentum (P_T).

2.1   The Accelerator

A total of seven acceleration devices are used to produce the colliding proton and antiproton beams, and their layout is shown in Figure 2-1. The first step in creating the proton beam involves the Cockcroft-Walton hydrogen gas chamber, across which there is a large electrostatic potential difference. Inside this device, electrons are added to hydrogen atoms, producing negatively charged H^- ions, which are accelerated by the electric field to an energy of 750 keV. The ions are then fed to a linear accelerator called the Linac. The Linac consists of five resonant radio frequency (RF) cavities followed by a side-coupled section based on seven klystrons. This system accelerates the ions to an energy of 400 MeV. On exiting the Linac, the ions are subjected to a charge-exchange process in which they are passed through a carbon foil which strips

away the electrons. This converts the H⁻ beam into a beam of positively charged protons which are then injected into the Booster. The Booster is a 75 m radius synchrotron in which the protons circle about 20,000 times while being accelerated to 8 GeV and formed into pulses or bunches, before being loaded into the Main Ring. The Main Ring is another synchrotron with a radius of 1000 m and contains 1000 copper-coiled magnets which continually bend and focus the protons. While this accelerator is capable of reaching energies of 400 GeV, it needs only to accelerate the protons to 150 GeV for insertion into the Tevatron. The Tevatron itself is also a synchrotron, located just below the Main Ring in the same tunnel. It is capable of accelerating protons to an energy of 1 TeV by a system of RF cavities. Alternating super-conducting dipole and quadrupole magnets are ramped synchronously to maintain the orbits of the protons at the Tevatron radius. Cooled by liquid helium, the superconducting magnets operates at a temperature of 5K ($-450°$ F).

The initial stages for creating the antiproton beam are the same as for the proton beam. A 120 GeV proton beam is extracted from the Main Ring to strike a nickel target. This produces a large variety of particles, including antiprotons. The target is optimized for producing antiprotons with an energy spectrum peaked at 8 GeV (the Main Ring injection energy), with an efficiency of about 20 antiprotons produced for every million protons fired into the target. The produced antiprotons have a momentum spread and angular divergence due to the dynamics of the p-Ni collisions. Thus, they must be "cooled" (i.e. reduced in phase space) in order to capture them with acceptably high efficiency in the Main Ring and the Tevatron, and to produce a compressed beam for high luminosity collisions. A lithium (a conductor with the smallest atomic number) lens is used to focus the antiprotons into a beam. The antiproton beam is transported to the Debuncher, a ring 520 m in circumference, where a phase space rotation reduces the longitudinal momentum spread. The transverse profile of the beam is diminished by Stochastic Cooling[49]. This cooling method uses a set of beam "pickups" and "kickers". The pickup coil in one section of the Debuncher detects the average deviation of the antiprotons from the central orbit of the ring, and a correction signal is sent across a chord to a kicker, in time to deflect the particle tra-
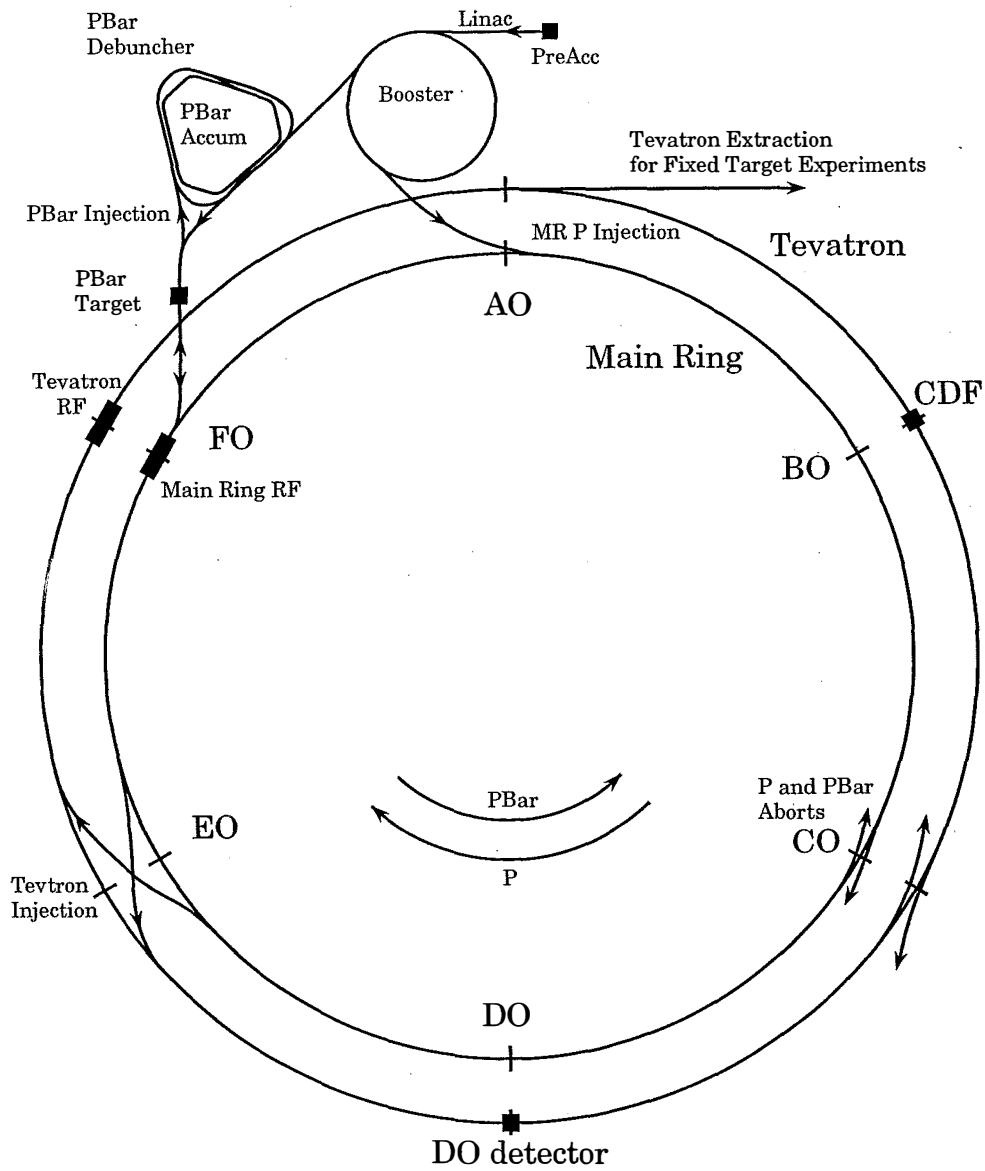
Figure 2-1: Schematic diagram of the particle accelerators at Fermilab. For simplicity, the Main Ring and Tevatron are diagrammed as coplanar.

jectories back onto the central orbit. Consequently, the transverse momentum spread of the antiproton beam is reduced. The cooled antiprotons are then transferred to the Accumulator, where they are slowly merged with the stack of previously generated antiprotons and further cooled. The Accumulator, which occupies the same tunnel as the Debuncher, normally stores the antiprotons for up to 24 hours until $> 2 \times 10^{11}$ antiprotons are accumulated. Once the anticipated number of antiprotons have been accumulated, they are transferred to the Main Ring for acceleration and injection into the Tevatron.

When operated in collider mode, the Tevatron accelerates the counter-rotating proton and antiproton beams to 900 GeV, producing 1.8 TeV center of mass energy. The beams are divided into six bunches of $\approx 2 \times 10^{11}$ protons and six bunches of $\approx 6 \times 10^{10}$ antiprotons. At regions where the beam bunches cross, electrostatic separators are used to keep them apart; but at the two interaction regions, labeled by their geographical locations as "B0" and "D0", special magnets focus the beams to collide with each other. At the interaction regions, the transverse beam sizes are diminished to about 40 μm, providing high-luminosity collisions. The number of bunches and the size of the accelerator imply that collisions occur once every 3.5 μsec. This defines the time frame needed for the data acquisition system described below. Also, whereas the transverse size of the bunches is small at the luminous regions, the longitudinal size is not; the distribution of collisions along the beam direction is approximately Gaussian with a standard deviation of ≈ 30 cm. Some of the important Tevatron parameters are given in Table 2.1.

The data used for this thesis were collected with the CDF detector surrounding the B0 interaction region. The data taking took place in the 1992-1995 collider run, known as Run 1. A total of ≈ 110 pb^{-1} of data were collected in two separate running periods, "Run 1A" and "Run 1B". Run 1A (26 August 1992 - 30 May 1993) collected ≈ 19 pb^{-1} and Run 1B (18 January 1994 - 24 July 1995) collected ≈ 90 pb^{-1}. The main differences between the two runs were the replacement of the Silicon Vertex Detector, the .upgrade of the data acquisition system, and the higher instantaneous luminosities of the Tevatron.

Beam Energy	900 GeV
Bunches/Beam	6
Bunch Spacing	3.5 μs
Protons/Bunch	2×10^{11}
Anti-protons/Bunch	6×10^{10}
Collision Region (RMS)	30 cm
Beam Size	40 μm
Typical Peak Luminosity	16×10^{30} cm^{-2}/s
Interactions/crossing	2.5

Table 2.1: Tevatron Collider parameters.

2.2 The CDF Detector

2.2.1 Coordinates and Kinematic Variables

The kinematics of the particles detected can be described in terms of Cartesian co-ordinates (x, y, and z). Further simplification can be achieved by exploiting the symmetry of the interactions. This motivates the use of polar coordinates (θ, and ϕ), as well as coordinates defined by the natural symmetries (pseudo-rapidity η and again, ϕ).

The origin of the Cartesian coordinates is chosen to be the nominal center of the detector and coincides with the center of the interaction region. The x axis is in the plane of the accelerator ring, pointing radially outward, and the y axis points up, perpendicular to the plane of the ring. The z axis completes a right handed coordinate system, and coincides with the direction of travel of the protons exiting the interaction point.

The Tevatron collides *unpolarized* beams of protons and antiprotons, therefore all physical observations are invariant under rotations around the beam line. Many calculations are then simplified by using a polar coordinate system. It is defined in the standard way with respect to the Cartesian coordinates, with the origins of the

azimuthal and polar angles, ϕ and θ, along the x and z axes, respectively.

Since protons and antiprotons are composite particles, the interactions actually occur between individual partons[1] which carry only some fraction of the proton and antiproton momenta. As a result, the center of mass of an interaction at the parton level can have a large momentum along the z axis in the laboratory frame of reference; whereas the total momentum in the plane transverse to the beam, $P_T = \sqrt{P_x^2 + P_y^2}$, remains zero. This means the collision products are in general boosted in the z direction. Noting that only the energy and the momentum along the z axis change under a boost in the z direction, we use a variable called rapidity

$$y \equiv \frac{1}{2} \ln \left(\frac{E + P_z}{E - P_z} \right).$$

This is useful as the rapidity distribution of the produced particles, dN/dy is invariant under Lorentz transformation along the z axis. Rapidity y is usually approximated by pseudo-rapidity

$$\eta \equiv \frac{1}{2} \ln \left(\frac{P + P_z}{P - P_z} \right) = -\ln(\tan \frac{\theta}{2})$$

which has the advantage of being independent of the mass of the particle and having a simple relationship with the polar angle. Pseudo-rapidity of a massless particle is equivalent to its rapidity; for massive particles the two are nearly the same when $P \gg m$.

2.2.2 Overview

Most final state particles produced at the Tevatron are energetic enough that it is experimentally advantageous to use variables such as P_T, ϕ, and η, which are invariant under Lorentz transformation along the beam direction. The Collider Detector at Fermilab (CDF) was thus designed to have an approximately cylindrically symmetric layout of detector components with uniform segmentation in η and ϕ whenever feasible. In general, the detector can be categorized into three layers: high resolution tracking on the inside, electromagnetic and hadronic calorimetry in the middle, and

---

[1]Partons are point-like constituents inside a proton. They can be referred to a valence or sea quark, or a gluon.

muon identification on the outside. A comprehensive description of the detector can be found in [50, 51]. Figure 2-2 shows an isometric view of the CDF detector whereas a side view cross-section of one quarter of the detector is shown in Figure 2-3.
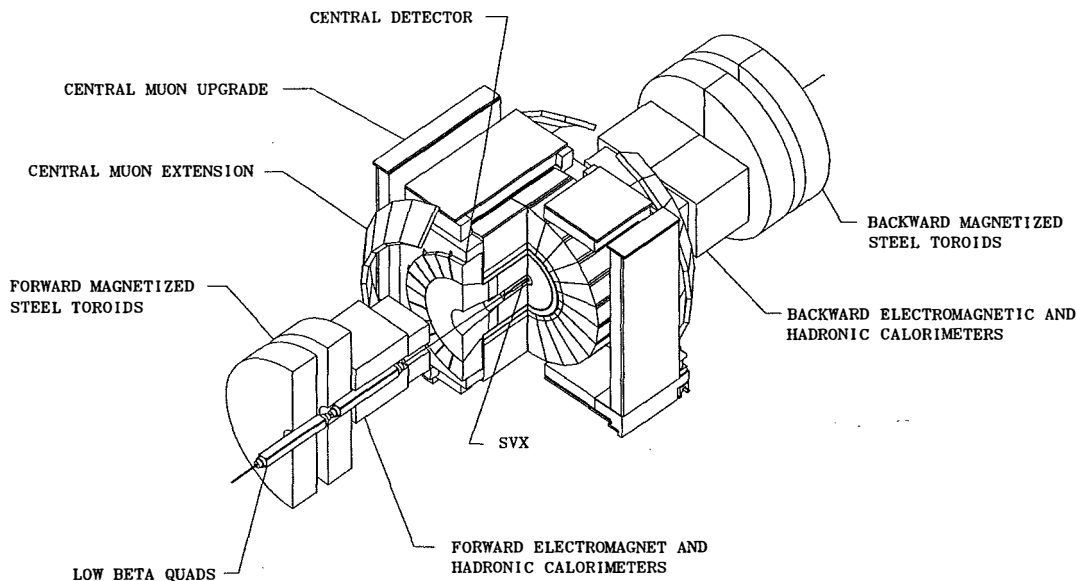
Figure 2-2: Isometric view of the CDF detector.

The tracking system is comprised of three principal components: the Central Tracking Chamber (CTC), the Silicon Vertex Detector (SVX), and Vertex Time Projection Chamber (VTX). They are placed inside a superconducting solenoid. Combined, they provide precise information on tracking parameters.

Outside the magnet are the calorimeters: the Central Electromagnetic Calorimeter (CEM) and the Central Hadronic Calorimeter (CHA). They measure the electromagnetic and hadronic energy flow of particles. They also serve as an absorber for interacting particles other than muons.

The muon chambers are placed behind the calorimetry. There are altogether four subsystems: the Central Muon Detector (CMU), the Central Muon Upgrade (CMP), the Central Muon Extension (CMX), and the Forward Muon System (FMU). They detect tracks for muon identification.

The CDF detector has essentially full azimuthal coverage, while the pseudo-
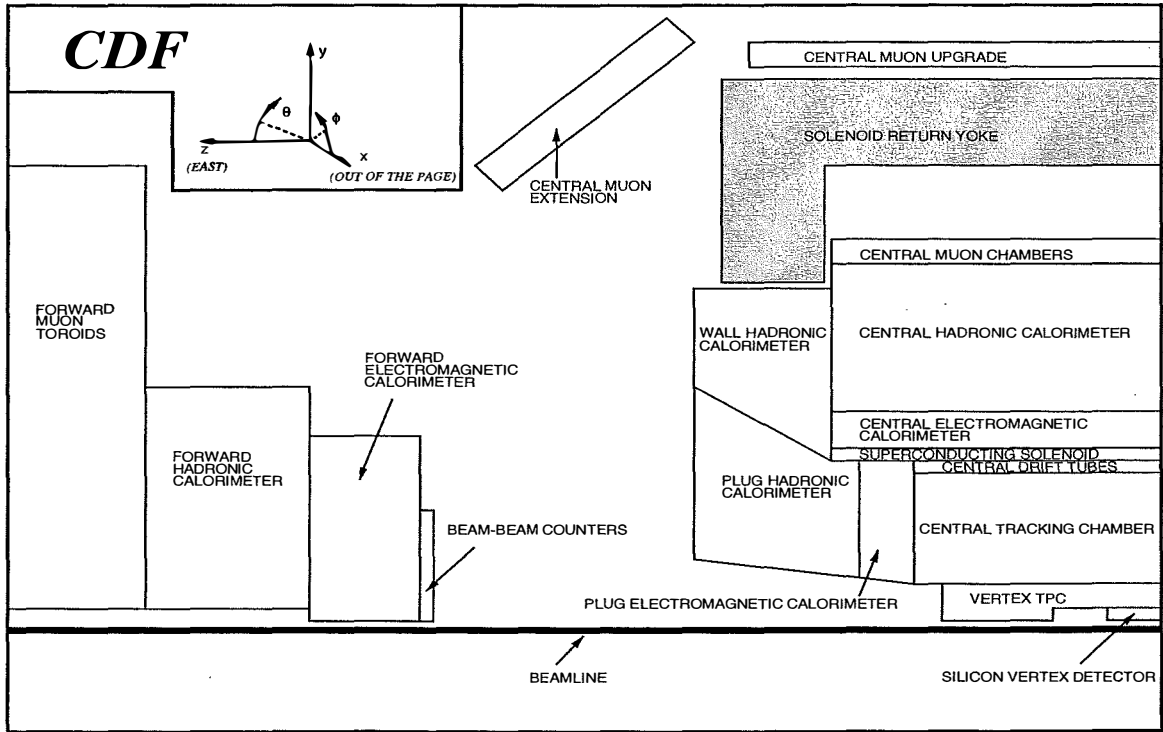
Figure 2-3: A cross-section view of one quadrant of the CDF detector. The detector is forward-backward symmetric about the interaction region, which is located along the beamline in the lower right corner. With the exception of the central muon upgrade and extension subsystems, the detector is also cylindrically symmetric about the beamline. The CDF coordinate system is shown inset in the upper left corner.

rapidity coverage reaches to $|\eta| \approx 4$.

Since this analysis is based on reconstruction of charged particle tracks with identification of muon candidates from $\psi(2S) \rightarrow \mu^+\mu^-$ decays, the detector components of main interest are the tracking chambers and the central muon detection systems.

2.2.3 Tracking

When charged particles pass through matter, they cause ionization as they interact with the matter electromagnetically. This ionization can be detected by electronic means to yield a set of spatial "hits" which can be used to form *tracks* that indicate the paths the particles followed. The CDF *tracking chambers* are designed for the detection of this ionization and the subsequent reconstruction of the trajectories of the charged particles.

At CDF, the tracking chambers are surrounded by a superconducting solenoidal magnet. Current running through 1164 turns of NbTi/Cu wire provides a 1.41 T magnetic field[2][52] which permeates a cylindrical region 4.8 m in length and 3 m in diameter. As a result, charged particles passing through the region follow helical paths with axes parallel to the beamline. Since the point of origin along the track helices is not observed directly, each of these helices can be described by five parameters namely c, d_0, ϕ_0, z_0, and $\cot\theta$.

Three of the tracking parameters, c, d_0, and ϕ_0, describe the projected circle in the $x - y$ plane due to the helix of a charged particle. $|c|$, called the track "curvature", is the inverse of the diameter of the circle; d_0, known as the "impact parameter", is the shortest distance from the origin to the circle; and ϕ_0 is the angle of the line tangent to the circle at its point of closest approach to the origin. These three parameters uniquely determine a circle. c and d_0 are signed quantities because positive and negative tracks curve in opposite directions under the magnetic field. Positive tracks have c positive, and negative tracks have c negative. The sign convention for d_0 is

---

[2]The nominal magnetic field value used for Run 1A was 1.4127 T; whereas for Run 1B, it was 1.4116 T with small run-dependent corrections from a database of magnetic field measurements taken over the course of the Run.

such that qd_0 is positive if the origin lies outside the circle, and negative otherwise, where q is the charge of the track. The remaining two parameters, $\cot\theta$ and z_0, determine the trajectory of the track in the $r - z$ view, where θ is the polar angle, and z_0 is the z-coordinate at the point of closest approach to the z axis.

In Section 2.2.1, we mentioned three tracking variables (P_T, η, and ϕ) which are convenient to use in detectors for high P_T physics like CDF. They can be determined from three of the helix parameters: $c, \cot\theta$, and ϕ_0. The P_T (in GeV) of a track is related to its curvature (in cm^{-1}):

$$P_T = \frac{2.998 \times 10^{-4} B_z}{2|c|} = \frac{.002116}{|c|},$$

where B_z is the z-component of the solenoidal field measured in kGauss and is equal to 14.116 kGauss. The pseudo-rapidity can be calculated by $\eta = -\ln\tan(\theta/2)$, where θ is the polar angle.

All five helix parameters are measured by the Central Tracking Chamber (CTC). The Vertex Time Projection Chamber (VTX) determines z position of primary interaction precisely, hence improving the accuracy of the z_0 and $\cot\theta$ measurements. The Silicon Vertex Detector (SVX) provides precise information on d_0 and ϕ_0, allowing accurate determination of displaced secondary vertices.

2.2.3.1   Silicon Vertex Detector

The Silicon Vertex Detector (SVX)[51] is a solid state detector placed around the beam pipe. This device provides very high resolution measurements of points on the trajectories of charged particles. As a result, the impact parameter d_0 and ϕ_0 of charged tracks can be determined precisely. This allows displaced secondary track vertices from the decay of long lived particles to be resolved from the beam position. For this analysis, we rely on this resolution to separate promptly produced $\psi(2S)$ mesons from those originating from B decays. At the Tevatron, B mesons, having a lifetime of ≈ 1.5 ps, typically travel a distance of about 1 mm before decaying; whereas the resolution of SVX can be as good as $25\mu m$.

The original SVX was installed at the beginning of Run 1A. Its response degraded

due to a cumulative exposure to radiation. Thus it was replaced by the radiation-hard SVX′ at the beginning of Run 1B. The features of SVX′ are described below, although the two detectors are very similar in construction. A comparison is shown in Table 2.2. In this thesis, both will be referred to as SVX.

Feature	SVX	SVX′
Channels	46080	46080
z coverage	51.1 cm	51.1 cm
Gap at z=0	2.15 cm	2.15 cm
Radius of layer 0	3.0049 cm	2.8612 cm
Radius of layer 1	4.2560 cm	4.2560 cm
Radius of layer 2	5.6872 cm	5.6872 cm
Radius of layer 3	7.8658 cm	7.8658 cm
Overlap of layer 0	-1.26deg	0.17deg
Overlap of layer 1	0.32deg	0.32deg
Overlap of layer 2	0.30deg	0.30deg
Overlap of layer 3	0.04deg	0.04deg

Table 2.2: A comparison of the SVX and SVX′ detectors.

The SVX is comprised of two barrels aligned along the beam direction (z axis). Each barrel has an active length of 25.5 cm, giving the SVX an active length of 51 cm around the interaction point. At $z = 0$, there is a small inactive gap of 2.15 cm where the two barrels are joined. An isometric view of an SVX barrel is shown in Figure 2-4. Because the beam profile is roughly Gaussian centered at $z = 0$ with $\sigma \approx 30$cm, the geometric acceptance of the SVX is only about 60%. The pseudo-rapidity coverage of the SVX is $|\eta| < 1.9$.

Each SVX barrel consists of four concentric layers of silicon strip detectors, with the innermost layer 2.9 cm from the beam line and the outermost at 7.9 cm. Every layer in turn contains twelve ladders. Figure 2-5 shows an SVX ladder. Each ladder has the same length as the barrel and covers approximately $30°$ of azimuthal angle. It
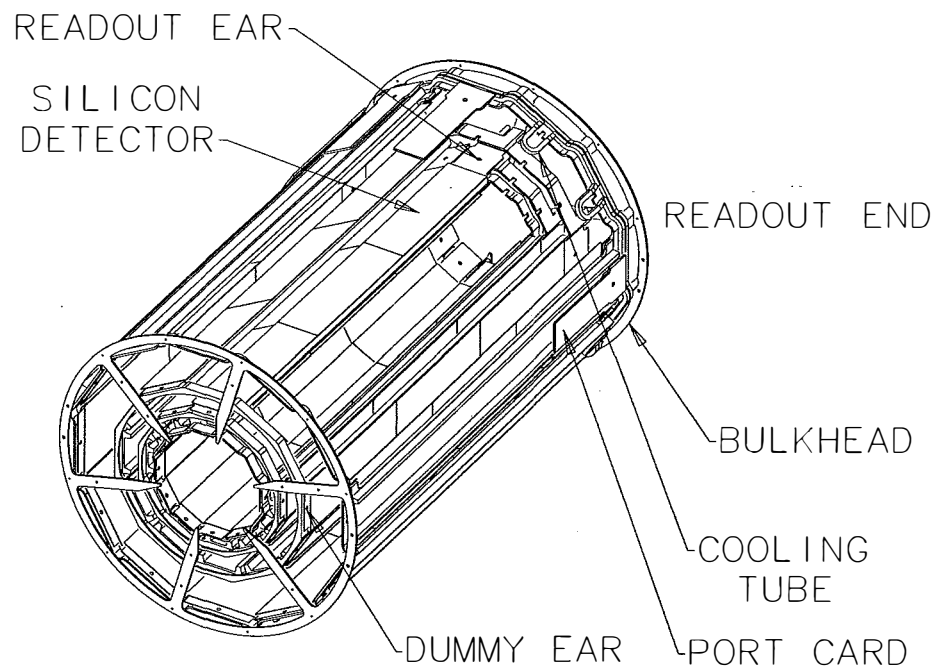
Figure 2-4: Isometric view of one of the two silicon vertex detector (SVX) barrels. It is comprised of four concentric layers of silicon strip detector elements. The dummy-ear sides of both barrels are conjoined at the $z = 0$ position inside the CDF detector.

is made up of three single sided silicon wafers, each 8.5 cm long, electrically connected with aluminum wire bonds. The readout strips of the silicon are aligned parallel to the beam line, making the SVX detector a 2-D tracking device in the $r - \phi$ plane. The pitch of the readout strips is 60 μm for the inner three layers and 55 μm for the outermost. Although the strips are separated by $\approx$ 60 μm, by considering the amount of charge collected in each strip from a charged particle, and by clustering several strips together, a resolution of about 10 μm can be achieved.

The SVX strips are read out in a "sparse mode", i.e. only those strips above threshold are read out for further processing. There are 2, 3, 4 and 6 chips (each with 128 channels) per ladder on layers 1 to 4 respectively, for a total of 46080 channels for the entire SVX detector. The typical readout time is about 2 ms, among the longest of all CDF detector subsystems.

2.3.2 Vertex Time Projection Chamber

The Vertex Time Projection Chamber (VTX) is a gas-filled drift chamber lying between the SVX and the CTC. While the other two detectors have excellent tracking resolution in the $r - \phi$ plane, the VTX provides $r - z$ tracking with high precision. This enables detection of primary vertices (i.e. proton-antiproton interactions) with a resolution of 1 mm. Such precision improves the z_0 and $\cot\theta$ information for tracks found in the CTC. Multiple vertices are often found, and these correspond to multiple interactions occurring during a given bunch crossing. The number of vertices scales with instantaneous luminosity.

The VTX is segmented into 8 modules along the z axis, covering the region between $z = \pm 1.4$ m. Its active volume extends radially from just outside the SVX to a radius of 21 cm. The pseudo-rapidity range is $|\eta| < 3.25$.

Each module is octagonal, composed of 8 wedges. At the center of each module is a high voltage grid that divides the module into two oppositely directed drift regions. In the presence of the 320 V/cm longitudinal electric field provided by the high voltage grid and the 50/50% argon-ethane gas mixture at atmosphere pressure, a drift velocity of 46 μm/ns is produced. The modules are designed to have a maximum
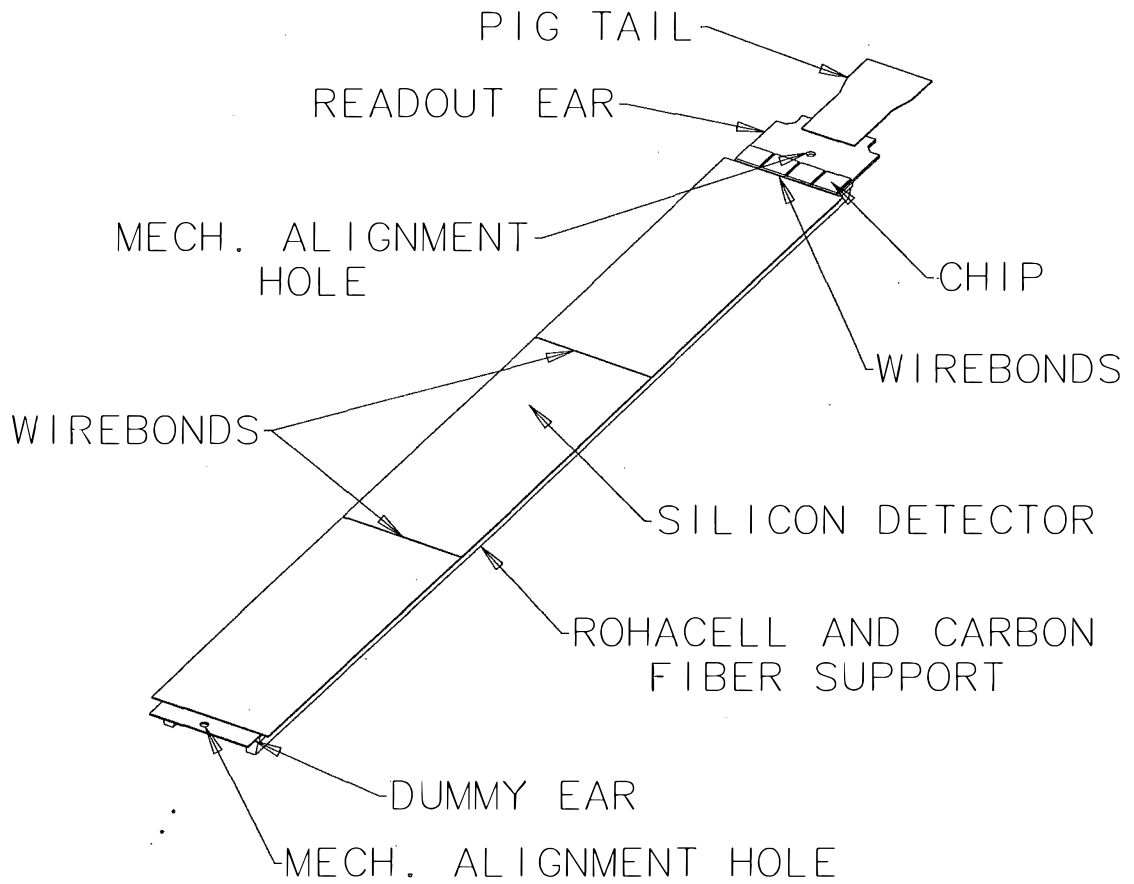
Figure 2-5: Layout of a SVX ladder. It has three single-sided silicon wafers wired bonded together.

drift distance of 15.25 cm so that the maximum drift time is always less than the 3.5 μs timing between $p\bar{p}$ bunch crossings. Adjacent modules are rotated by 11.3^o about the beamline. For tracks passing through at least two modules, this eliminates inefficiencies near octant boundaries and provide ϕ information from small angle stereo.

The ionization electrons drift away from the central grid until they pass through a cathode grid and enter one of the two endcaps. Each endcap is divided into octants, with 24 sense wires and 24 cathode pads in each octant. The arrival times of the electrons at the sense wires give information on the location of the hits in the $r - z$ view. The hits are then combined to give track segments which are extrapolated to the beamline, and fits are performed to find the primary vertices.

2.2.3.3   Central Tracking Chamber

The Central Tracking Chamber (CTC)[53] is a cylindrical drift chamber located between the VTX and the superconducting solenoid. It is the mainmast of CDF tracking, providing efficient 3-D tracking information with good precision (single track reconstruction efficiency is in excess of 90%, and at a resolution better than 200 μm).

The CTC is 3.2 m long along the z axis, covering the pseudo-rapidity range $|\eta| < 1.1$. Its physical dimension extends from an inner radius of 27.4 cm to an outer radius of 138 cm.

The CTC consists of 84 layers of sense wires, grouped into 9 "superlayers". A cross-sectional view is shown in Figure 2-6. The superlayers are logically sub-divided into regions called "open cells" ("open" because of no physical division between the cells). The cells in each superlayer are evenly spaced in azimuth so that the maximum drift time is about 800 ns, much shorter than the 3.5 μs between bunch crossings.

In addition to sense wires, each cell also contains field wires and field-shaping wires which produce a drift field (E) of $\approx$ 1350 V/cm. The superconducting solenoid provides a uniform 1.4 T magnetic field (B). In the presence of crossed electric and magnetic fields, electrons no longer drift along the electric field direction, but at an
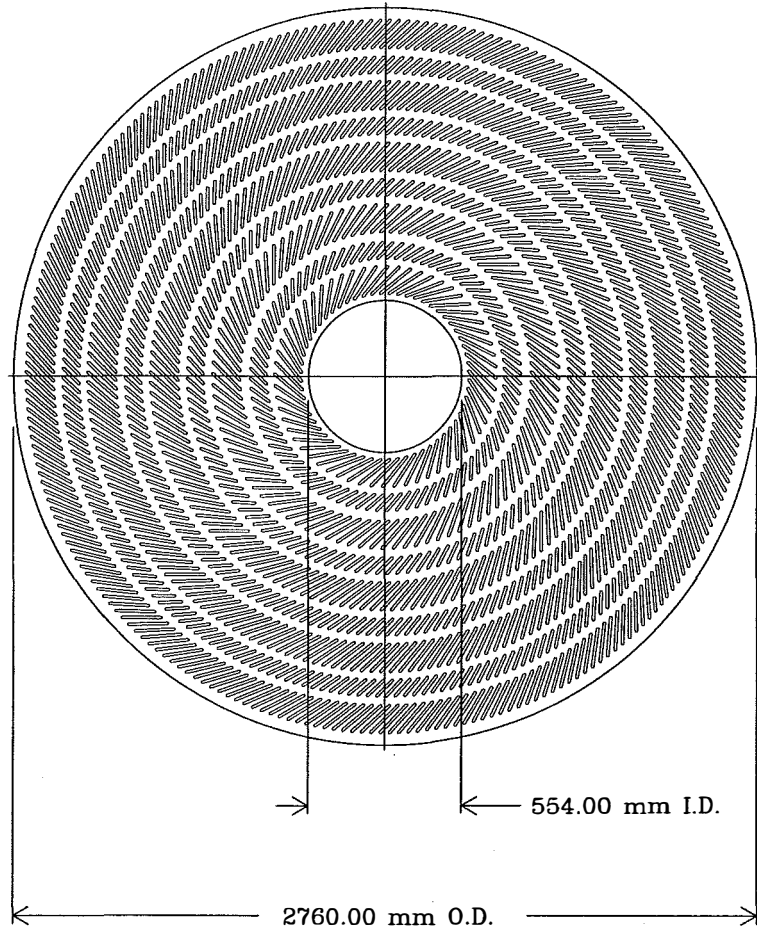
Figure 2-6: Transverse view of the central tracking chamber (CTC). The wire slot locations for the five axial and four stereo superlayers are shown. The wires lie at an angle of 45° with respect to the radial direction. The inner diameter (I.D.) and outer diameter (O.D.) are shown in the plot.

angle β relative to it given approximately by:

$$\tan \beta = \frac{v(E, B = 0)B}{kE},$$

where $v(E, B = 0)$ is the drift velocity without the magnetic field, B and E are the magnetic and electric field strengths. The parameter k depends on the type of drift gas and the magnitude of the E-field. $k \approx 0.7$ in a gas mixture of argon/ethane/ethanol (49.6/49.6/0.8%) at the given E. This gives $\beta \approx 45^o$ for the normal operating conditions in the CTC.

To compensate for the value of β, all wires in each cell are tilted at 45° with respect to the radial direction. Subsequently, the electron drift direction becomes azimuthal, i.e. perpendicular to the radius vector. This results in best resolution for high P_T tracks which traverse radially. Tilting the cells also helps to reduce dead space and linearize the time-to-distance relationship at the end of the cells caused by a large β. A large tilt angle ensures overlapping between neighboring cells in the azimuthal directions so that every high P_T track must pass close to at least one wire in every superlayer. Such "zero crossing" condition on the drift time is exploited to resolve closely spaced tracks. Moreover, having large β and tilt angle helps resolve the left-right ambiguity which arises from the inherent inability of a single sense wire to determine which side of the wire the electrons drifted from. The large β and tilting cause the wrong solution to be rotated by $\Delta = \tan^{-1}(2 \tan \beta) \approx 70^o$ relative to the true track direction. This large rotation simplifies the rejection of "ghost tracks".

The 9 superlayers are numbered 0 through 8, going from the innermost out. The 5 even numbered superlayers are "axial" superlayers. Each cell in these superlayers consists of 12 sense wires for a total of 60 axial wires. These wires are aligned with the z axis, providing $r - \phi$ tracking information. The 4 odd numbered superlayers are "stereo" superlayers, with each cell contains 6 sense wires for a total of 24 stereo wires. The wires form an angle of $\pm 3^o$ with respect to the z axis ($+3^o$ for superlayers 1 and 5, -3° for superlayers 3 and 7), and enable track reconstruction in the $r - z$ plane. Table 2.3 summarizes the resolutions of the five helix parameters measured by the CTC.

δP_T	$0.002 P_T^2$ $(\mathrm{GeV/c})^{-1}$
δd_0	200 μm
$\delta \phi_0$	0.02
δz_0	1 cm
$\delta \cot \theta$	0.01

Table 2.3: Resolution of the five track parameters measured by the CTC.

The CTC has 6,156 sense wires, and each is read out by a multi-hit TDC. Two different pattern recognition algorithms then search the TDC data for tracks.

2.2.4 Calorimetry

Calorimeters are designed to measure the energy of particles. When particles pass through matter, they can induce particle "showers". For example, an electron can radiate a photon through bremsstrahlung[3], which can then convert into an electron-positron pair; these in turn can radiate more photons. Such cascading processes produce an electromagnetic shower. Similarly, hadrons produce showers by interacting strongly with the protons and neutrons from the atomic nuclei in the material.

Muons do not produce showers in calorimeters. Being 200 times heavier than electrons, muons have negligible energy loss due to bremsstrahlung[4]. In addition, muons are not affected by the inelastic scattering that produces hadronic showers, because they do not undergo strong interactions. Normally muons only lose energy by ionizing the medium through which they pass. In this analysis, the muons are required to deposit some small amount of energy in the calorimeters; otherwise, the calorimeter information is not used at all.

The CDF detector has two calorimeter systems: the Central Electromagnetic Calorimeter (CEM) and the Central Hadronic Calorimeter (CHA). They are sampling

---

[3]Bremsstrahlung refers to the process of energy loss in which an electron is decelerated by the electric field of an atomic nucleus and radiates a photon.

[4]The rate of energy loss due to bremsstrahlung is proportional to $1/m^2$, where m is the mass of the charged particle.

calorimeters consisting of alternate layers of active medium and absorber. These detectors are segmented into towers, each covering 0.1 in η and 15° in ϕ, which point back to the interaction point.

The CEM is placed outside the solenoid and has a pseudo-rapidity coverage $|\eta| <$ 1.1. It consists of 62 alternating layers of lead and scintillator, and a proportional chamber for measurement of the shower profile. The position resolution of the CEM is about 2 mm, and the energy resolution is $\delta E_T / E_T = \sqrt{(13.5\%/\sqrt{E_T})^2 + (2\%)^2}$ where E_T is the transverse energy measured in GeV/c.

The CHA is located behind the CEM, covering the region $|\eta| < 0.9$. It is divided into 528 towers which consist of 64 alternating layers of steel and scintillator. The energy resolution of the CHA is $\delta E_T / E_T = \sqrt{(50\%/\sqrt{E_T})^2 + (3\%)^2}$.

In addition to *central* calorimeters, the *plug, wall* and *forward* calorimeters cover regions of larger pseudo-rapidity, $1.1 < |\eta| < 4.2$.

2.2.5 Muon Detection

The ability to identify muon candidates is essential to the reconstruction of $\psi(2S)$ mesons through its dimuon decay mode. Muons, being minimum ionizing particles, do not interact strongly with atomic nuclei. In addition, they have a relatively long lifetime and large mass. They can, therefore, penetrate much more material than any other type of charged particle. This property is exploited to detect muons by placing the muon chambers in the outer regions of the CDF detector. The material of the inner detector components serves to stop the majority of hadrons and electrons before they reach the muon chambers.

The CDF has four muon detectors: the Central Muon Detector (CMU), the Central Muon Upgrade (CMP), the Central Muon Extension (CMX), and the Forward Muon System (FMU). Except for the FMU, they are all situated to detect muons which pass through the central tracking chambers and the calorimeters. The dimuon data sample for this analysis only uses CMU information.

2.2.5.1 The Central Muon Detector

The Central Muon Detector (CMU)[54] covers z with cylindrical symmetry from $9.1 < |z| < 512.5$ cm and surrounds the inner detectors at a radial distance of 3,470 mm from the beam axis. This corresponds to a pseudo-rapidity coverage of $|\eta| < 0.6$ with a small gap at 0. It covers ϕ uniformly in 12.6^o segments called "wedges", with gaps of 2.38^o between adjacent wedges. There are altogether 48 wedges, half surrounding the east half of the detector and half surrounding the west half. Each wedge is equally divided into three "trigger towers", each subtending 4.2^o in ϕ. A trigger tower, shown in Figure 2-7, consists of four layers, each containing four rectangular drift cells.

A drift cell is of dimensions 63.5 mm $\times$ 26.8 mm $\times$ 2,261 mm and has a 50-μm stainless steel sense wire strung through its center. The cells are operated in limited streamer mode with a 50/50% argon-ethane gas mixture. This provides a resolution of 1.2 mm on the position of a muon candidate track along the z direction whereas the azimuthal resolution is 250 μm.

In the four layers of drift cells, the outermost and the second innermost layers are oriented such that their sense wires lie on a radial that originates from the interaction point. The other two layers are offset by 2mm. The offset resolves the left-right ambiguity inherent in drift chambers. The position of a candidate muon track is determined from the pairwise difference in drift times to wires in layers 1 and 3, and 2 and 4. This can be related to the transverse momentum of the track and such information is promptly available to the trigger system, as described in Section 2.2.6.

Charged particle tracks in the muon chambers are referred to as "stubs". Muon reconstruction begins by searching for stubs with 3 or 4 hits. The stubs are then matched to extrapolated tracks from CTC. Close matches are identified as muon candidates. Using the CMU hit positions and the locations of the extrapolated CTC tracks in the $r - \phi$ and $r - z$ planes, two χ^2 are formed for later use in rejecting background.

The inner detector components surrounded by the CMU constitute about 5 ab-
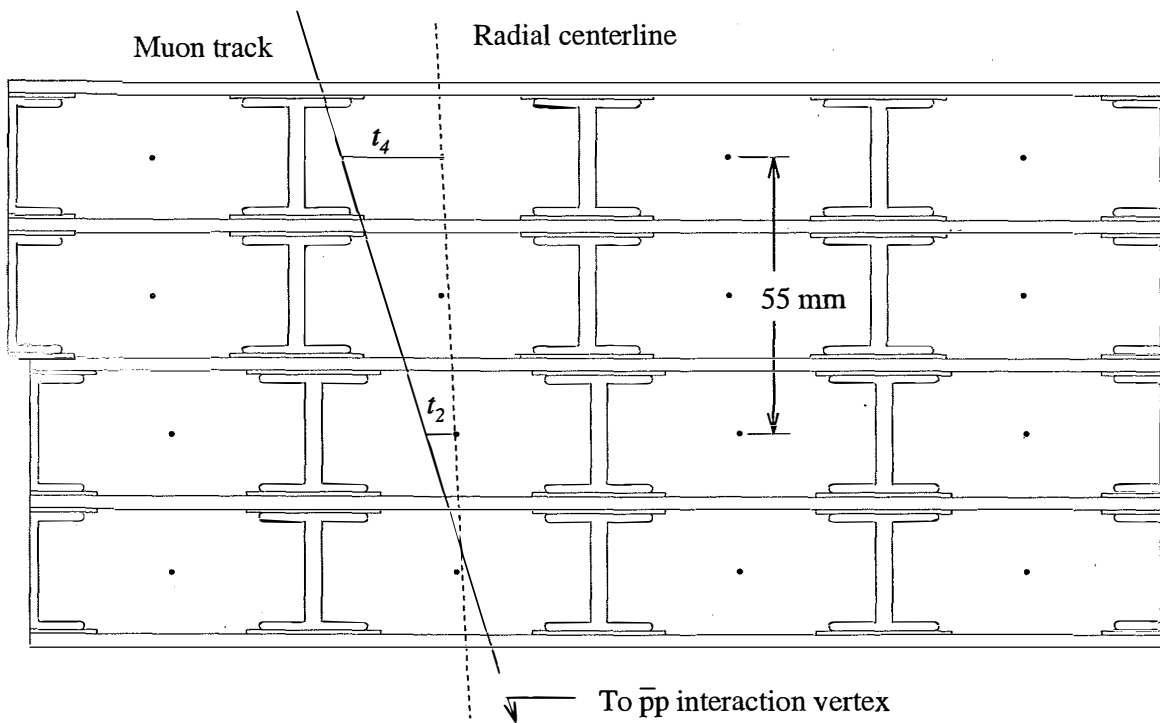
Figure 2-7: Layout of a central muon detector (CMU) tower which is comprised of four layers of rectangular drift cells.

sorption lengths of material at normal incidence. In addition to filter out the hadrons and electrons, the material also stops muons below a P_T of 1.4 GeV/c, known as the muon rangeout threshold[55]. When a muon traverses through the material, its path is deflected by multiple coulomb scattering. This makes the extrapolation of a muon's trajectory uncertain, which decreases inversely with the transverse momentum of the muon.

2.2.5.2   Other Muon Detectors

The Central Muon Upgrade (CMP) has the same z and η coverage as the CMU, with a rectangular box geometry. The CMP is located outside the solenoid return yoke which helps to stop high-energy hadrons that escape through the calorimeters ("punch through"). The presence of steel yoke is equivalent to an additional two absorption lengths of material at 90° incidence. A total of 864 drift cells, each 2.54 cm $\times$ 15.24 cm in cross section, constitute the CMP.

The Central Muon Extension (CMX) consists of four free-standing conical arches, two on each side of the CDF detector. The CMX covers a pseudo-rapidity region $0.6 < |\eta| < 1.0$, extending muon coverage over the useful acceptance of the CTC. It has 1,536 drift cells which are grouped into modules. An array of scintillation counters is mounted on the inner and outer sides of each module, providing background rejection and a high speed trigger.

The Forward Muon System (FMU) detects muons in the high-η region, $|\eta| > 1.0$. Since it lies outside the acceptance of the central tracking system, the FMU has its own toroidal magnets, providing rough momentum measurement.

2.2.6   Triggering

The total $p\bar{p}$ cross section at $\sqrt{s} = 1.8$ TeV is about 80 mb[56], while the cross sections for interesting processes are orders of magnitude smaller. For example, the cross section times branching ratio for $\psi(2S) \to \mu^+\mu^-$ is nearly nine orders of magnitude smaller. The $p\bar{p}$ bunch crossings in the Tevatron collider occurs every 3.5 μs, corre-

sponding to a crossing frequency of ≈ 300 kHz. On the other hand, a typical CDF event has a data size of ≈ 165 kB, which can only be reliably written out to tapes at a rate of ≈ 10 Hz. For these reasons, a *triggering* system is needed to filter out interesting events from the overwhelming bulk of uninteresting interactions with a $\approx 30,000 : 1$ rejection factor. The CDF trigger consists of three levels, with each successive level making a more detailed examination of the data events (and hence taking a longer time) to impose the filtering criteria.

2.2.6.1 Level 1

The Level 1 trigger is capable of making an accept/reject decision in less than 3.5 μs between beam crossings, thus incurring no dead time. Such a speed of operation is achieved by the analog readout and processing of data from selected detector components with FASTBUS-based electronics. The Level 1 trigger primarily uses signals from the calorimeters and the muon systems. The combined rate of level-1 accepts is about 1-2 kHz, two orders of magnitude less than the input rate of 300 kHz. Events passing the Level 1 trigger are digitized and passed to the Level 2 trigger.

At Level 1, muon triggers require that a muon candidate must have a stub in the muon detectors, subject to a minimum transverse momentum threshold. Specifically, for the dimuon triggers used in this study, the two stubs are required to be noncontiguous. That is, at least one trigger tower that does not contain a muon stub must reside between the two stubs[5]. Otherwise, the two adjacent towers with muon stubs are merged and treated as a single muon for the purpose of the Level 1 trigger. The minimum P_T threshold for the Level 1 muon trigger is nominally 3.3 GeV/c.

2.2.6.2 Level 2

When the Level 1 trigger is fired, it is inhibited from considering subsequent $p\bar{p}$ collisions for a period of up to 40 μs. During this dead time, the Level 2 trigger

---

[5]One exception is when the two adjacent muon stubs (having same ϕ) are in the opposite halves of the detector. They will pass as a dimuon trigger because the east and west halves of the detector are independent.

performs more sophisticated procedures and makes its decision. It looks for clusters of calorimeter towers and for correlations between different detector systems such as the tracking systems and the muon chambers. The information is organized to identify "physics objects" which include electrons, photons, taus, jets, neutrinos, and muons.

The Level 2 trigger uses a hardware processor, called the Central Fast Tracker (CFT)[57], to find tracks in the CTC with high speed. The CFT finds 2-D tracks in the $r - \phi$ projection by examining hits in the five axial CTC superlayers. In each superlayer, the CFT considers hits with two types of timing information: prompt and delayed hits. Prompt hits, gated ≤ 80 ns after the beam crossing, are due to charged particles traversing the small drift distance radially. Delayed hits, gated 500-650 ns after the beam crossing, are caused by charged particles drifting across the cell to the adjacent sense wires in the ϕ direction. The absolute prompt and delayed drift times provide information on a track's trajectory, whereas the relative drift times give measurements of curvature, and hence P_T. Once the prompt and delayed hits are located, the CFT begins with the prompt hits in superlayer 8 (outermost and thus lowest hit density) and looks to the inner layers for hit patterns that match those in a look-up table. As a result, a list of tracks is reconstructed and sorted into 16 bins in P_T and 144 bins in ϕ.

At Level 2, the dimuon triggers impose a matching criterion between at least one of the two Level 1 muon stubs and a CFT track. The CFT track is extrapolated to the muon chambers, with effects due to multiple scattering taken into account. The extrapolated track and the stub are required to have an azimuthal separation $\Delta\phi \leq 5^o$. Muon stubs with matched CFT tracks are associated with calorimeter towers to form Level 2 muon clusters. Muon clusters are demanded to be noncontiguous[6]. A typical muon cluster includes 3 calorimeter towers, while adjacent muon clusters merge to form a 6-tower cluster.

---

[6]If one muon is in the east and the other in the west half of the CDF detector, the two muon clusters are required to be at different ϕ. This Level 2 requirement is more stringent than that in Level 1.

When the Level 2 trigger accepts an event, the detector is read out, which makes the detector blind for 2 ms. With a level-2 accept rate of about 20 Hz, this dead time is only about 6%.

2.2.6.3 Level 3

The Level 3 trigger collects the event fragments through a demultiplexer called the "event builder" (Section 2.2.7). The trigger runs a reduced version[7] of the offline reconstruction code on a farm of commercial computers. The software also contains filtering modules which provide a rejection factor of 3. The average processing time for an event is about 1 s. Accepted events are passed to a data logger which caches them on disk and then writes them out to tape at a rate of less than 10 events per second.

Level 3 also sorts the accepted events into *streams*. There are three streams: A, B, and C, in the order of descending priority. This allows important events to be studied quickly while those of less interest are made available more slowly.

At Level 3, both the full CTC track reconstruction and the standard muon reconstruction are performed. Each CTC track is extrapolated to the appropriate muon subsystem, with the energy loss and multiple scattering corrected. The position of the projected track is compared with that of the muon stub in both the $r - \phi$ and the $r - z$ views. The dimuon triggers used in this analysis require the matching to be within 6 (3) standard deviations of the combined multiple scattering and measurement uncertainties for Run 1A (1B). In addition, the dimuon invariant mass is required to be in the window 2.8-4.0 (2.7-4.1) GeV/c^2 for Run 1A (1B).

2.2.7 Data Acquisition

The data acquisition (DAQ) pipeline begins with the front end electronics in which the analog signals from channels in the various subsystems of the CDF detector are read out, amplified and digitized. The signals are passed to the Level 1 and Level 2

---

[7]The reduced version does not used the SVX information and eliminates reconstruction of objects that are not used in the trigger, such as very low momentum tracks.

triggers where an accept/reject decision is made on the event. Once a level-2 accept is fired, the trigger supervisor, a FASTBUS module, initiates the readout of data from the front end electronics using custom processors (so called FASTBUS readout controllers or FRCs). The FRCs send their data to six VME-based processors known as scanner CPUs or SCPUs. The event fragments are then transported to the Level 3 processor nodes via a commercial network. To ensure event fragments belonging together are passed to the same L3 processor, the scanner manager, also a VME-based CPU, coordinates the data flow between the SCPUs and the Level 3 trigger system by using a reflective memory network. The scanner manager communicates with the trigger supervisor via the trigger supervisor interface.

Events accepted by the Level 3 trigger are passed to the consumer server which distributes the events to consumers. Some consumers are diagnostic applications that monitor data quality and detector performance. Another consumer provides an on-line interactive event display system. Yet another consumer runs three data logger programmes (one for each output data stream) which write accepted events to staging disks and subsequently to 8-mm tapes.

Chapter 3

Data Sample and Signal Extraction

3.1   The Data Sample

The experimental data for this analysis were collected by the CDF detector from 1992 to 1995. During this period, the Fermilab Tevatron collided protons with antiprotons at a center of mass energy of $\sqrt{s} = 1.8$ TeV. This running period is generally known as Run 1 and was split into two separate parts: Run 1A and Run 1B. The data recorded during Run 1A amounted to a time-integrated luminosity ($\int \mathcal{L}dt$) of 19.5 ± 1.0 pb^{-1}. In Run 1B, 89 ± 7 pb^{-1} of data were written to tape, yielding a Run 1 total of $\int \mathcal{L}dt = 109 \pm 7$ pb^{-1}. The data logging efficiencies were 70% and 77% for Run 1A and 1B respectively.

Data stored on tape were processed in "production farms" of commercial computers. The processing used offline reconstruction code that examined events more thoroughly than was possible in the Level 3 trigger system. This included locating primary vertices from the VTX, finding tracks in the CTC without any explicit P_T requirement, and using SVX information to match up with CTC tracks to form combined SVX-CTC tracks. Also muon stubs were matched with CTC tracks to form muon candidates. Other physics objects such as electron candidates and calorimeter jets were reconstructed as well. During the processing, run-dependent information such as calibration and alignment constants were also used. The processed events were then split into several data sets based on physics analysis criteria.

In this analysis, we start with the data set of low P_T dimuon triggers. The following sections provide more details on the track and muon reconstruction procedures. The reconstruction of $\psi(2S)$ candidates from dimuons is described in Section 3.4, whereas the extraction of the signal as a function of $\cos\theta^*$ is described in Section 3.5.

3.2   Track Reconstruction

Track reconstruction starts with the set of primary vertices identified by the VTX. The CTC track finding algorithms then associate the hits in the outermost superlayer with those in the inner superlayers so that they are compatible with an arc of a helix originating from one of these primary vertices. The helical trajectory is then extrapolated back into the SVX, where hits are searched for along a "road" of a given width calculated from the CTC track parameters and covariance matrix. If a sufficient number of SVX hits are found, they are included in refitting the CTC track to form a combined SVX-CTC track. Otherwise, the SVX information is not used. This results in a sample of tracks classified as "SVX" and "CTC" respectively. For this analysis, an SVX track is required to have hits on at least three of its four layers. This reduces random associations of a CTC track with hits in the SVX, but also restricts the analysis to candidates with well-measured decay lengths, as will be described in Chapter 5. We only use dimuons where both muons have SVX reconstructed tracks. The sample of CTC muons was studied but it is not included in the final analysis. This is because the proper time resolution of the CTC is much poorer than that of the SVX, making it impossible to separate the prompt and the B-decay components by relying on the CTC information alone. The poorer mass resolution of the CTC also results in fitting the dimuon invariant mass distribution more difficult. The statistical improvement on the polarization measurement of the $\psi(2S)$ meson from adding the CTC sample is expected to be only $\approx 10\%$.

The combined SVX-CTC tracking provides a transverse momentum resolution of $\delta P_T/P_T = \sqrt{0.0066^2 + (0.0009 P_T)^2}$ $(\text{GeV/c})^{-1}$ and an impact parameter resolution of $\delta d = (13 + 40/P_T)$ μm. This indicates good resolution in P_T and d for the sample

used in this analysis as most muons in the sample are in the P_T range $2 - 3$ GeV/c.

3.3   Muon Selection

Muons are selected by matching good quality stubs in the muon chambers to good quality tracks. A good muon stub is required to have 3 or 4 hits (out of a maximum of 4) in a muon chamber and the χ^2 of fitting these hits to a straight line must be less than 10. A good track is as defined in the previous section. The matching is done by extrapolating the track from the inner tracking chambers to the muon detectors, and comparing the position of the projected track with that of the muon stub. A position matching χ^2[58] is calculated by squaring the difference of the distance between the two, and dividing it by the combined error on the CMU position measurement and the CTC track extrapolation. The associated energy loss and multiple scattering in the extrapolation are taken into account. For this analysis, the components of the matching χ^2 in the x and z directions are both required to be less than 9.

The matching requirement is useful in reducing two major sources of muon backgrounds. One is "interactive punch-through" which occurs when a charged hadron, typically a kaon or a pion, enters the calorimeter and initiates a shower, but some of the daughter charged hadrons in the shower may pass through the calorimeters and enter the muon systems. If one of these particles leaves a stub in the muon chamber which is consistent with a track reconstructed in the CTC, then a fake muon candidate is formed. In this case, however, the match between the muon stub and the extrapolated CTC track is usually much worse than for a real muon, since the daughter particles generated in the shower usually travel at an angle relative to the parent hadron that initiated the shower.

The other major source of muon background is from "decay-in-flight" muons. These are muons produced by the decays $\pi^{\pm}, K^{\pm} \rightarrow \mu^{\pm}\nu_{\mu}$. The charged hadron track is reconstructed in the CTC and the daughter muon registers a stub in the muon chamber. These muons also result in a poorer match between the CMU stub and the CTC track extrapolation because the direction of the decay-in-flight muon is displaced

73

from the direction of the charged hadron.

When a muon candidate travels through the calorimeters, it can deposit a small amount of ionization energy there before reaching the muon detector. Therefore, the energy deposition in the hadronic calorimeter cell in front of the muon stub is required to be above the pedestal level. To select muons detected in the central portion of the detector, the muons are also required to have $|z| < 60$ cm.

In Run 1A, the above muon quality cuts are found to be useful in reducing background, and they are more than 95% efficient[8]. A comparable effectiveness of these cuts is found for the triggers in Run 1B.

Furthermore, only events that have fired triggers whose efficiency can be well determined are used. For this analysis, four dimuon triggers are used, they are known as: CMU_CMU_ONE_CFT from Run 1A and CMU_CMU_TWO_CFT, CMU_CMU_ONE_CFT, and CMU_CMU_SIX_TOW from Run 1B. See Appendix B for a description of these triggers. More than 70% of the events are from CMU_CMU_TWO_CFT_1B.

A minimum P_T requirement is applied to the muon candidates. The muon P_T cuts are chosen to minimize systematic effects from the trigger while retaining a large acceptance. The magnitude of the P_T threshold depends on which trigger the dimuon passes, and the thresholds are listed in Table 3.1. For the one-CFT triggers, a higher P_T threshold is imposed on the muon matched with a CFT track, allowing a lower threshold on the other muon stub. This asymmetric P_T requirement is especially beneficial for accepting events with large values of $|\cos\theta^*|$, and it is those events which are most sensitive to the value of the polarization.

dimuon trigger	muon P_T cuts (GeV/c)
CMU_CMU_ONE_CFT_1A	one $\geq$ 1.7, other $\geq$ 2.7
CMU_CMU_ONE_CFT_1B	one $\geq$ 1.7, other $\geq$ 2.9
CMU_CMU_TWO_CFT_1B	both $\geq$ 2.0
CMU_CMU_SIX_TOW_1B	both $\geq$ 2.0

Table 3.1: The muon P_T requirement for each of the four triggers used.

3.4 $\psi(2S)$ Reconstruction

Muons passing the selection criteria outlined in the previous section are considered as potential candidates originating from a $\psi(2S)$ meson through its decay $\psi(2S) \rightarrow \mu^+\mu^-$. Oppositely charged muon pairs are subject to a "vertex constraint" fit[59], which forces the two tracks to originate from a common point in space (as expected from the decay of a single particle). In this fit, the track parameters, corrected for multiple scattering and energy loss, are adjusted iteratively to minimize the χ^2. The resulting χ^2 per degree of freedom is required to be less than 10. This eliminates close tracks which are not really consistent with the hypothesis of originating from a common vertex. This requirement is effective in reducing background due to heavy flavor decays, such as $b\bar{b}$ or $c\bar{c}$, which produce opposite sign muon pairs through semileptonic ($b\bar{b} \rightarrow c\bar{c}\mu^+\mu^-X$ or $c\bar{c} \rightarrow s\bar{s}\mu^+\mu^-X$) or sequential ($b \rightarrow c\mu^+\nu_\mu$ followed by $c \rightarrow s\mu^-\bar{\nu}_\mu$) decays, where the muons have originated from different vertices.

In order to remain in the region where the kinematic acceptance does not vary very rapidly, the reconstructed $\psi(2S)$ candidates are also required to have $P_T > 5.5\,\mathrm{GeV/c}$.

Table 3.2 summarizes the list of the selection cuts imposed throughout the reconstruction chain.

Tracks	≥ 3 hits in SVX
Muons	trigger-dependent P_T cuts
	track matching $\chi_x^2 < 9$
	track matching $\chi_z^2 < 9$
	nonzero energy in hadronic calorimeter
	$|z| < 60$ cm
$\psi(2S)$	$P_T > 5.5\,\mathrm{GeV/c}$
	vertex constraint $\chi_{\mathrm{fit}}^2 < 10$

Table 3.2: List of the selection requirements applied in the reconstruction of the $\psi(2S)$ meson candidates.

The invariant mass distribution of the reconstructed $\psi(2S)$ candidates after the

above selection is shown in Figure 3-1. The mass peak due to signal $\psi(2S)$ events is clearly seen. We define a signal region to be between 3.63 GeV/c^2 and 3.73 GeV/c^2. This corresponds to a 100 MeV/c^2 window around approximately 3.686 GeV/c^2, the world-average[5] value of $\psi(2S)$ mass. The signal region contains most of the signal events. We also define two "sidebands", one on each side of the mass peak. The lower sideband extends from 3.48 GeV/c^2 to 3.58 GeV/c^2, while the upper sideband extends from 3.78 GeV/c^2 to 3.88 GeV/c^2. The sidebands are well separated from the signal region and contain predominately background events, providing a good estimate of the number of background events. Therefore, with proper scaling to account for the difference of mass window size between the signal region and the sidebands, an estimate of the number of signal events can be obtained by subtracting the number of events in the sidebands from that in the signal region. This "sideband-subtraction" method gives a total of 1826 ± 64 signal $\psi(2S)$ candidate events in our data sample, with a signal to background ratio of 1.18 ± 0.04 in the signal region.

To study the P_T dependence of the polarization, we divide the data sample into three $\psi(2S)$ P_T bins (5.5-7, 7-9, and 9-20 GeV/c). Each sample is further divided into two sub-samples based on the measured $\psi(2S)$ proper decay length (ct) distribution. A short-lived sample selected in the low ct region ($-0.1 < ct \leq 0.01$ cm) is enriched of $\psi(2S)$ mesons from prompt production, while a long-lived sample selected in the high ct region ($ct > 0.01$ cm) is dominated by $\psi(2S)$ mesons from B decays. Chapter 5 will discuss the fitting of the $\psi(2S)$ ct distribution to determine the composition of prompt, B, and background in the samples.

3.5   Mass Fit

The extraction of the polarization α requires fitting the $|\cos\theta^*|$ angular distribution[1]. In principle, the $\psi(2S)$ event yield in each $|\cos\theta^*|$ bin can be determined by doing a sideband subtraction of the mass distribution in the bin. However, we find this method inadequate because it is more susceptible to statistical fluctuations. There-

---

[1]Since the angular distribution is symmetric, the absolute value of $\cos\theta^*$ is used.
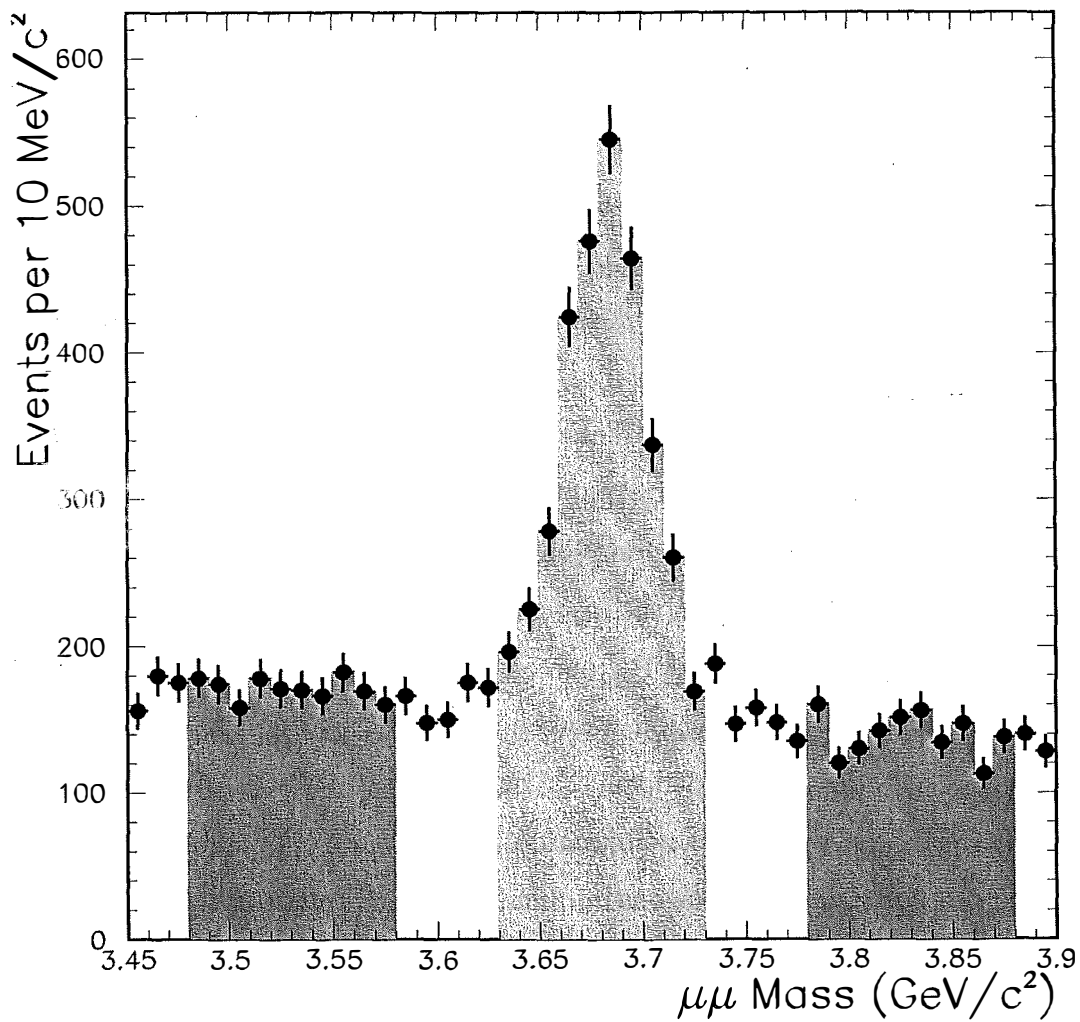
Figure 3-1: The invariant mass distribution of the reconstructed $\psi(2S)$ mesons after the various selection requirements are imposed. The signal region is defined to be $3.63 \leq m_{\mu^+\mu^-} \leq 3.73$ GeV/c^2 and the sidebands as $3.48 \leq m_{\mu^+\mu^-} \leq 3.58$ GeV/c^2 or $3.78 \leq m_{\mu^+\mu^-} \leq 3.88$ GeV/c^2. These regions are shaded in the histogram.

fore, we fit the mass distributions in different bins of $|\cos\theta^*|$ instead to achieve more robust measurements of the $\psi(2S)$ event yields.

The invariant mass distribution of the $\psi(2S)$ meson candidates is parameterized by a Gaussian signal plus a linear background:

$$\frac{N}{\Delta m\sqrt{2\pi}\sigma}\exp\left[-\frac{1}{2}(\frac{m-\mu}{\sigma})^2\right] + a_0 + a_1(m-\mu) \qquad (3.1)$$

where N is the number of signal events under the gaussian. The parameters μ and σ are the mean and width of the gaussian, whereas a_0 and a_1 are the offset and the slope of the linear background. The mass histograms have a bin width Δm of 15 MeV/c^2. The fits are carried out using the log likelihood method which readily handles bins with zero events correctly.

In the bins with large $|\cos\theta^*|$, the event yield is low, causing difficulties in fitting the mass distributions to a parameterization with five free parameters. Therefore, the mean and width of the gaussian signal function are constrained in order to ensure that the mass fits converge. This reduces the free parameters in the fits to three. Noting that the mass resolution depends on P_T, one expects the mass width to depend on $|\cos\theta^*|$ as well, due to the correlation between P_T and $|\cos\theta^*|$. We use a Monte Carlo simulation to study this dependence. Decays of $\psi(2S) \to \mu\mu$ are generated and propagated through the detector simulation (see Chapter 4 for the details). The reconstructed dimuon mass distributions in different $|\cos\theta^*|$ bins are then fitted with a Gaussian to determine the widths. Figure 3-2 shows the mass width versus $|\cos\theta^*|$ in the three different $\psi(2S)$ P_T bins: $5.5-7, 7-9$, and $9-20$ GeV/c. One sees rather flat distributions in the $5.5 < P_T \le 7$ GeV/c and $7 < P_T \le 9$ GeV/c ranges. However, a significant rise towards higher $|\cos\theta^*|$ bins is seen in the $9 < P_T \le 20$ GeV/c bin. Yet, when the distribution of this P_T bin is divided into smaller P_T bins, the resulting distributions in $|\cos\theta^*|$ are also seen to be flat.

To confirm that the rise is due to the integrated effect of $\psi(2S)$ P_T, we rescale the $\psi(2S)$ mass to compensate for the P_T dependence of the mass width. The top plot in Figure 3-3 shows the mass width as a function of P_T in the $9 < P_T \le 20$ GeV/c

range. The masses of the candidates in each P_T bin are then rescaled by:

$$\frac{\sigma_1}{\sigma_i}(m - \mu_i) + \mu_1$$

where m is the mass of each event and μ_i and σ_i are the mean and width of the mass distribution in the ith P_T bin. This essentially rescales the mass distributions in higher P_T bins to match the mass distribution of the first P_T bin. The rescaled mass distributions are fitted to a Gaussian to determine their new widths. As expected, the mass width is now flat in P_T after rescaling, as shown in the middle plot of Figure 3-3. The bottom plot of Figure 3-3 shows the mass width as a function of $|\cos\theta^*|$ in the $9 < P_T \leq 20$ GeV/c bin after rescaling. The rise is much reduced. This indicates that the $\cos\theta^*$ dependence of the mass width is largely due to P_T.

To correct for the rising widths, one can use the Monte Carlo distribution in the bottom plot of Figure 3-2 as scaling factors to be applied when fitting data mass distributions. To check the validity of these Monte Carlo scaling factors, we compare the mass widths between data and Monte Carlo in J/ψ, a data sample which has ≈ 50 times more statistics, and thus provides a more accurate comparison than that of the $\psi(2S)$ sample. Figure 3-4 shows the J/ψ mass width as a function of the J/ψ P_T.[2] We see that data have larger widths than Monte Carlo. Nevertheless, good agreement between data and Monte Carlo is seen if the Monte Carlo widths are raised by 25%. This indicates that the Monte Carlo can reproduce the shape of the mass resolution dependence on P_T observed in the data. Therefore, the Monte Carlo scaling factors, governed by the shape of the mass resolution P_T dependence, can be applied when fitting the data mass distributions.

Finally, the following procedure is used to fit the mass distributions of $\psi(2S)$ candidates in the data: In the $5.5 < P_T \leq 7$ GeV/c and $7 < P_T \leq 9$ GeV/c bins, the mass distribution, integrated over all $|\cos\theta^*|$ bins to gather more statistics, is fitted to get the global mass mean and width. These values are then used to fix the mean and width in fitting the mass distribution in each $|\cos\theta^*|$ bin. The offset and the

---

[2]It is sufficient to compare the mass width as a function of P_T because the mass width dependence is largely due to P_T.
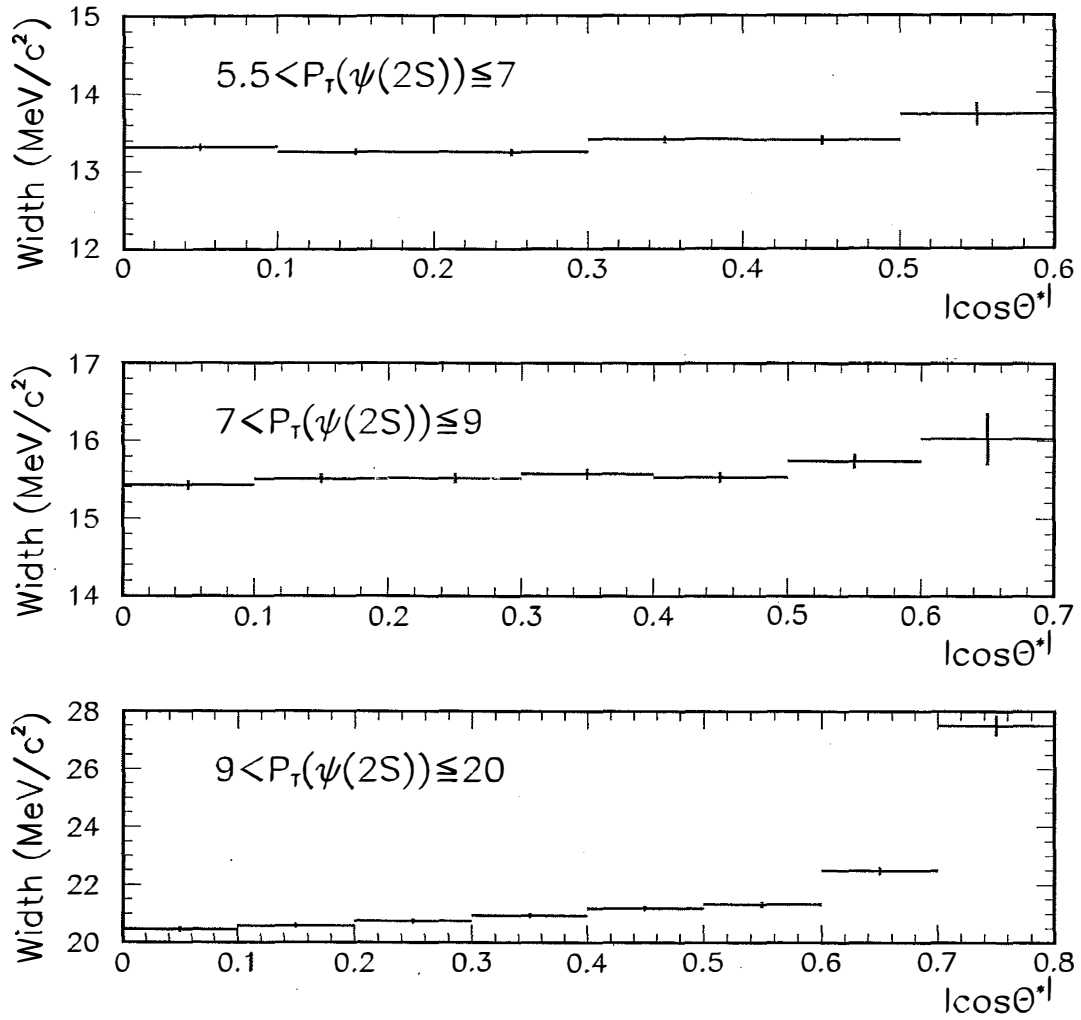
Figure 3-2: Mass width of $\psi(2S)$ Monte Carlo as a function of $|\cos\theta^*|$ for three P_T ranges.
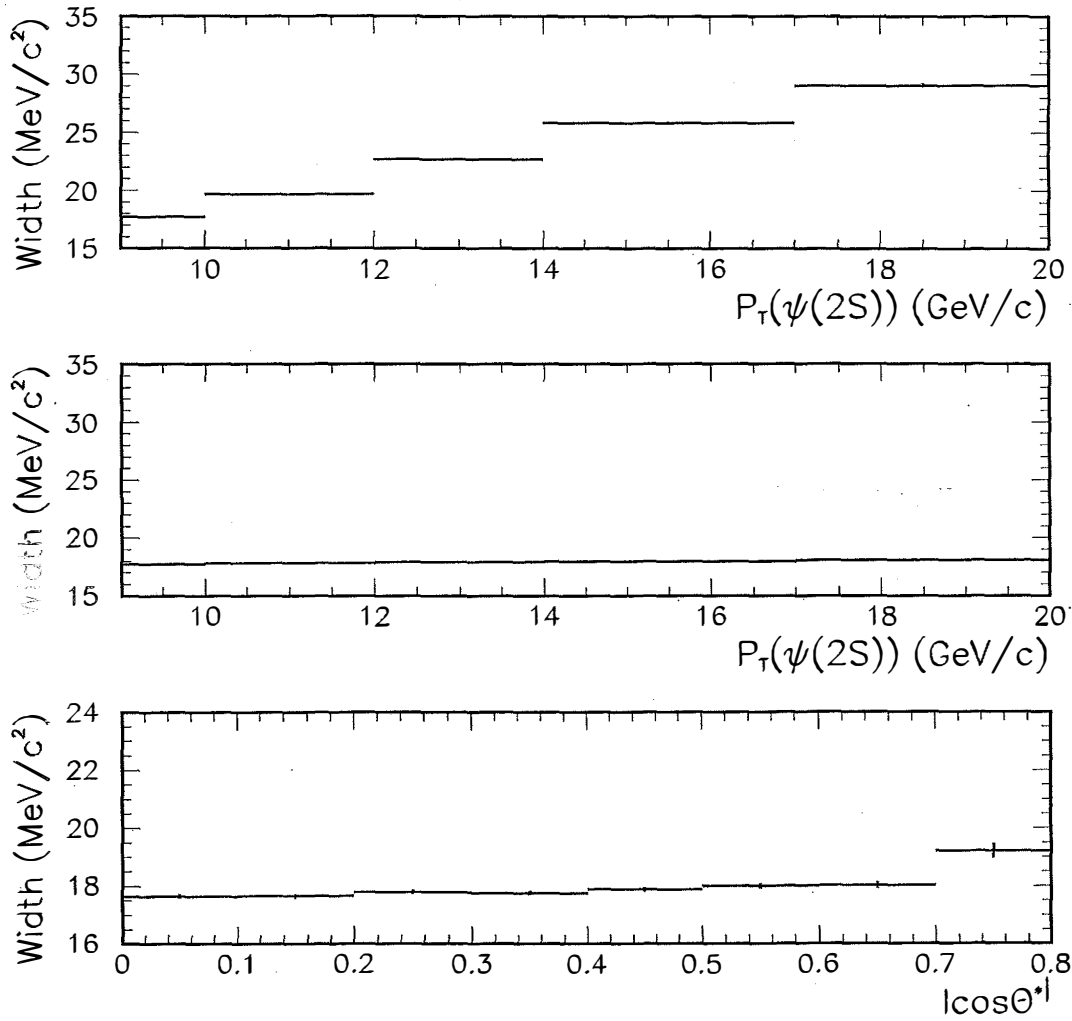
Figure 3-3: Consistency check that the $\cos \theta^*$ dependence of mass width is largely due to P_T. The top plot displays the mass width of $\psi(2S)$ Monte Carlo as a function of P_T for the $9 < P_T \le 20$ GeV/c range. The center plot shows the mass width as a function of P_T after mass rescaling for the $9 < P_T \le 20$ GeV/c range. The bottom plot depicts the mass width as a function of $\cos \theta^*$ after mass rescaling for the $9 < P_T \le 20$ GeV/c range.
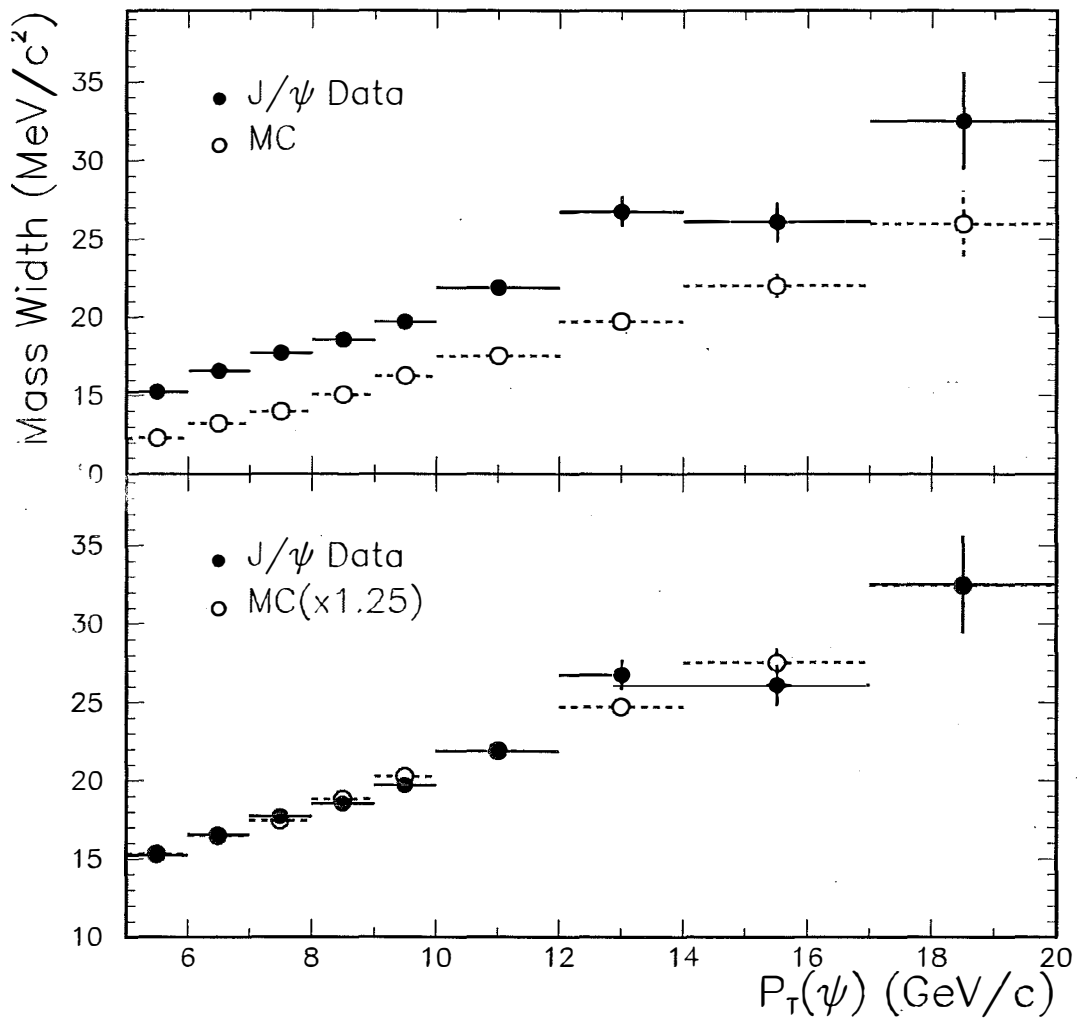
Figure 3-4: Comparison of mass widths of J/ψ data and Monte Carlo as a function of P_T. This shows that the Monte Carlo can reproduce the shape of the mass resolution dependence on P_T observed in data.

slope of the linear background are left floating in each fit. In the $9 < P_T \leq 20$ GeV/c range, the mass distribution, integrated over the first 6 $|\cos\theta^*|$ bins where the mass width is seen to rise slowly (see Figure 3-2), is again fitted to get a global mass mean and width. These values are again fixed in fitting the mass distributions in individual $|\cos\theta^*|$ bins, with the width further multiplied by a bin-by-bin scaling factor obtained from the bottom plot of Figure 3-2 to account for the rising width.

The resultant fits to the $\psi(2S)$ mass distributions in the three $\psi(2S)$ P_T bins are shown in Figures 3-5, 3-6 and 3-7. These are for events selected in the region of low $\psi(2S)$ proper decay length ($-0.1 < ct \leq 0.01$ cm). The $\psi(2S)$ mass fits in the high ct region ($ct > 0.01$ cm) for the three P_T bins are shown in Figures 3-8, 3-9 and 3-10 respectively. The event yield and the χ^2 per degree of freedom of the mass fits are listed in Tables 3.3 and 3.4 for the low and high ct regions. Figures 3-11 and 3-12 show the resulting $|\cos\theta^*|$ distributions. Each data point represents the number of signal events obtained by fitting the mass distribution in the corresponding $|\cos\theta^*|$ bin. One sees the event yield decrease to zero at large $|\cos\theta^*|$. This is due to the acceptance of the CDF detector, as will be described in the next chapter.
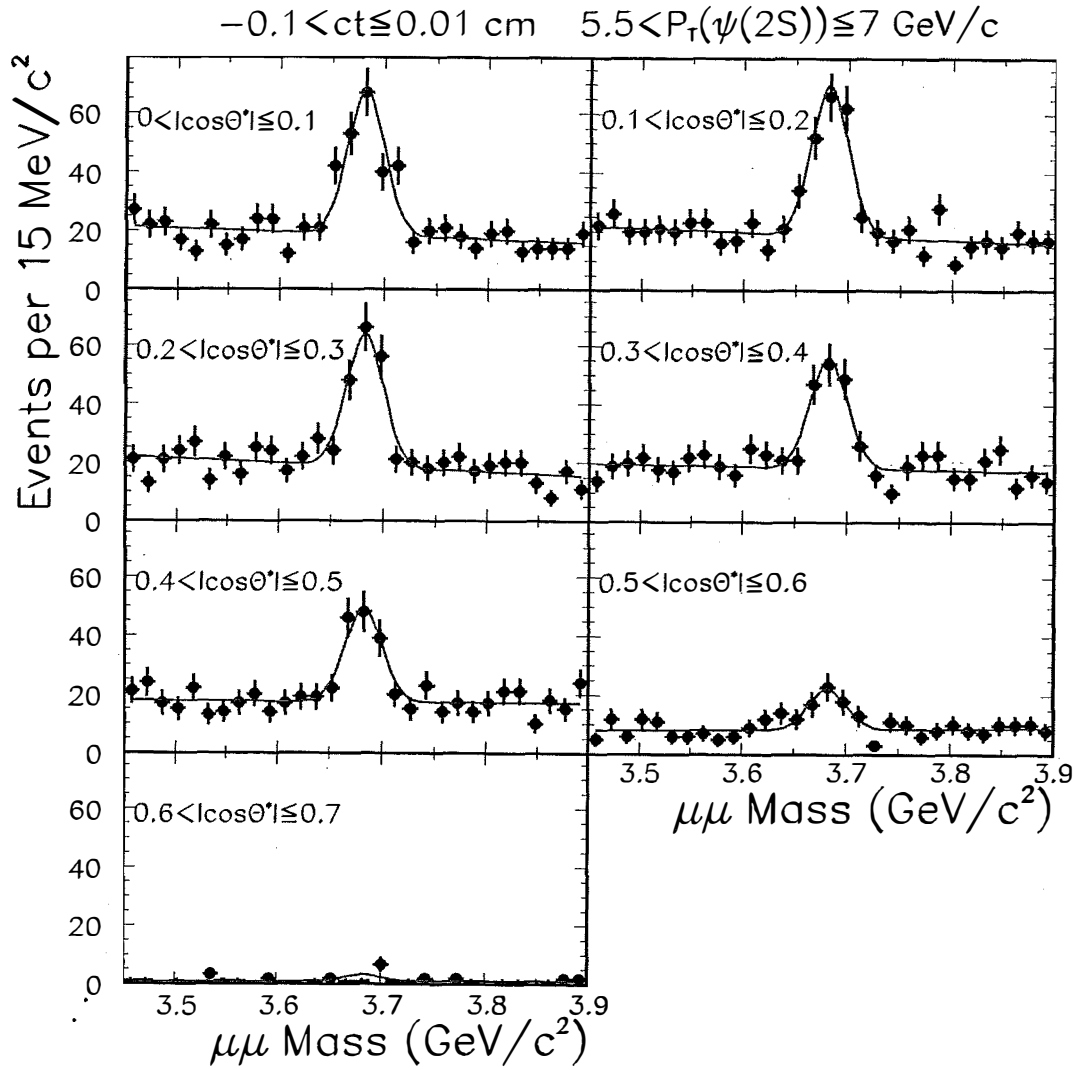
Figure 3-5: The invariant mass distributions of dimuons selected for the $\psi(2S)$ analysis. The $\psi(2S)$ candidates are required to have $5.5 < P_T \leq 7$ GeV/c and $-0.1 < ct \leq 0.01$ cm. In each plot, the data are shown as points, whereas the line shows the result of a maximum-likelihood fit. The mass distributions are displayed in increasing $|\cos\theta^*|$ bins.
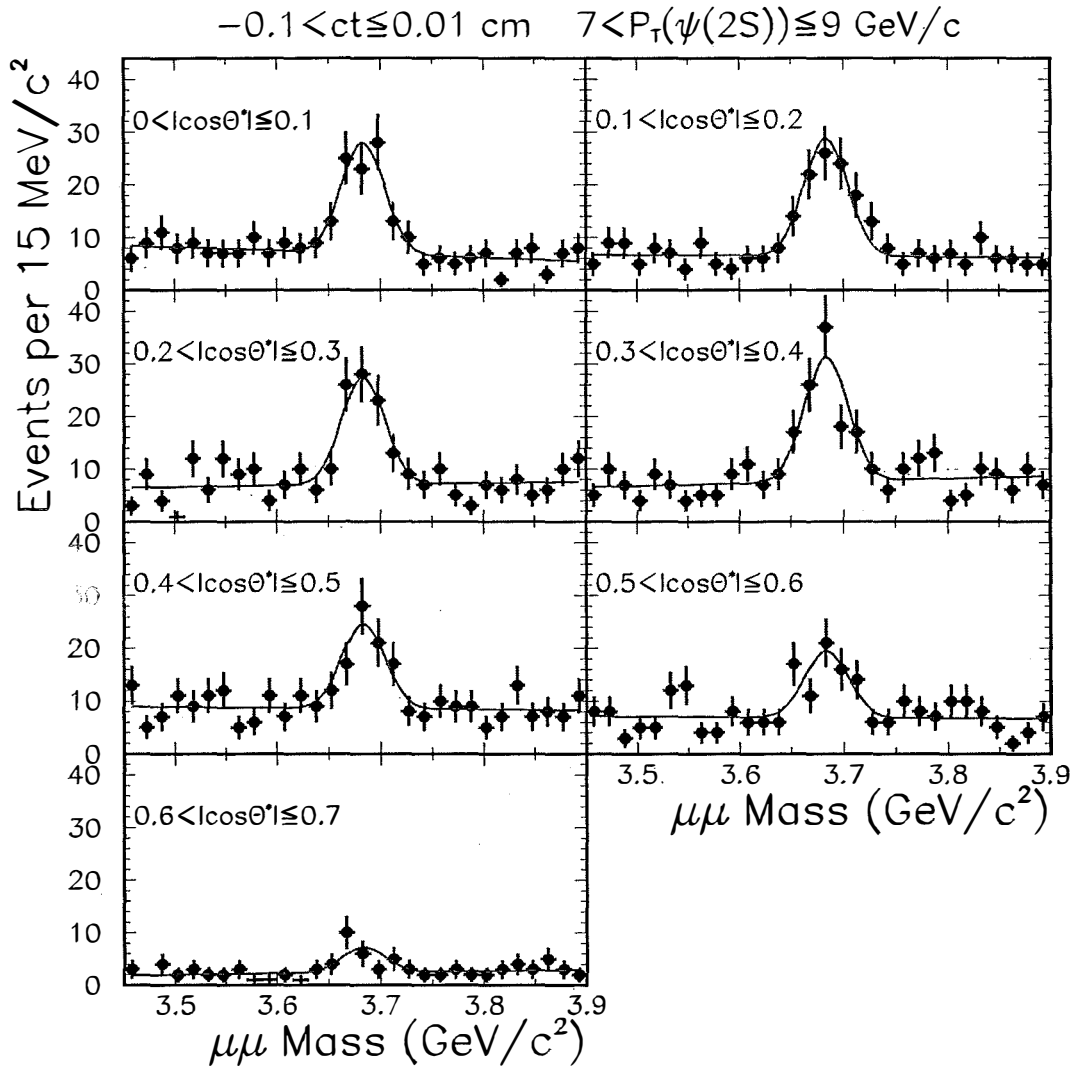
Figure 3-6: The invariant mass distributions of dimuons selected for the $\psi(2S)$ analysis. The $\psi(2S)$ candidates are required to have $7 < P_T \leq 9$ GeV/c and $-0.1 < ct \leq 0.01$ cm. In each plot, the data are shown as points, whereas the line shows the result of a maximum-likelihood fit. The mass distributions are displayed in increasing $|\cos\theta^*|$ bins.
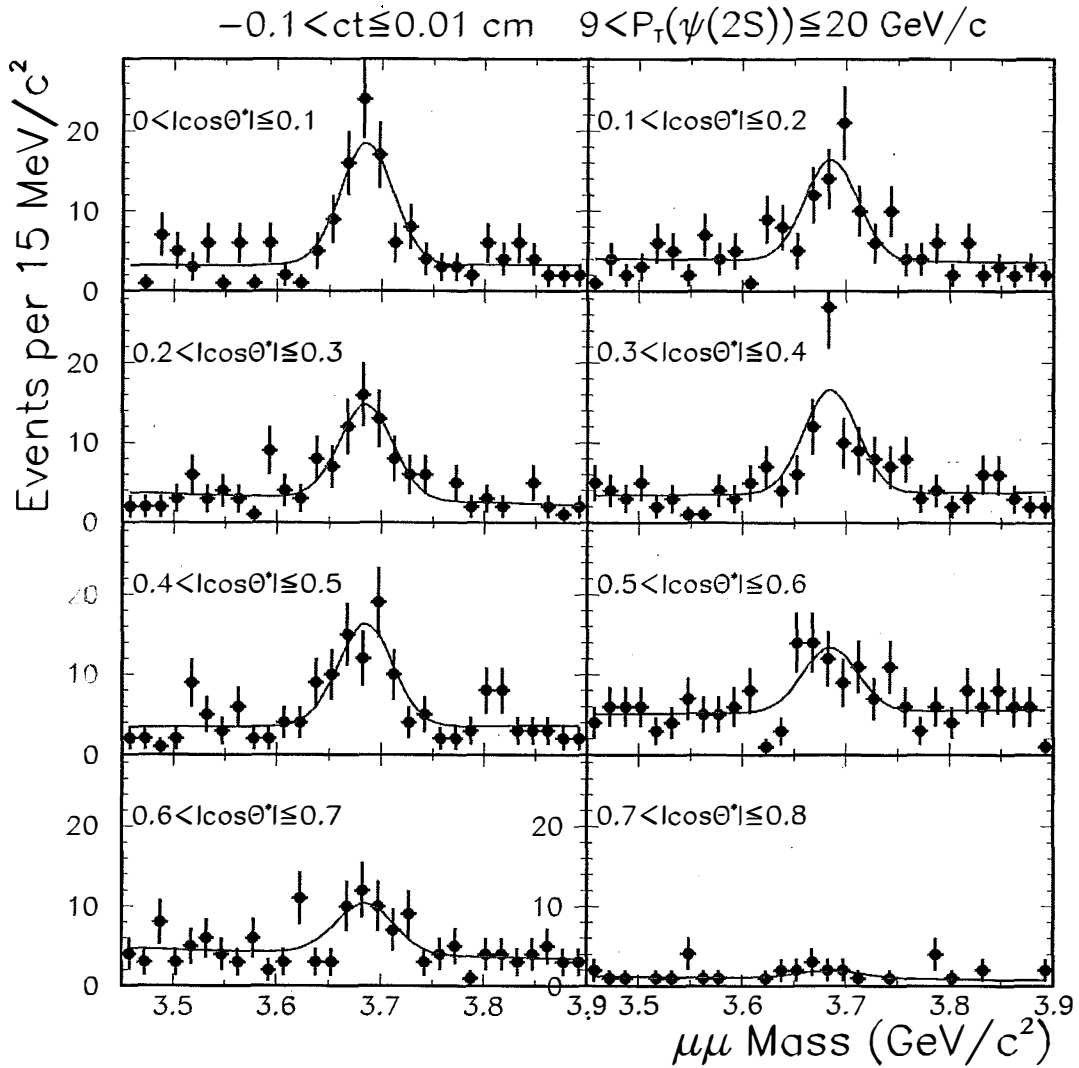
Figure 3-7: The invariant mass distributions of dimuons selected for the $\psi(2S)$ analysis. The $\psi(2S)$ candidates are required to have $9 < P_T \leq 20$ GeV/c and $-0.1 < ct \leq 0.01$ cm. In each plot, the data are shown as points, whereas the line shows the result of a maximum-likelihood fit. The mass distributions are displayed in increasing $|\cos\theta^*|$ bins.

86
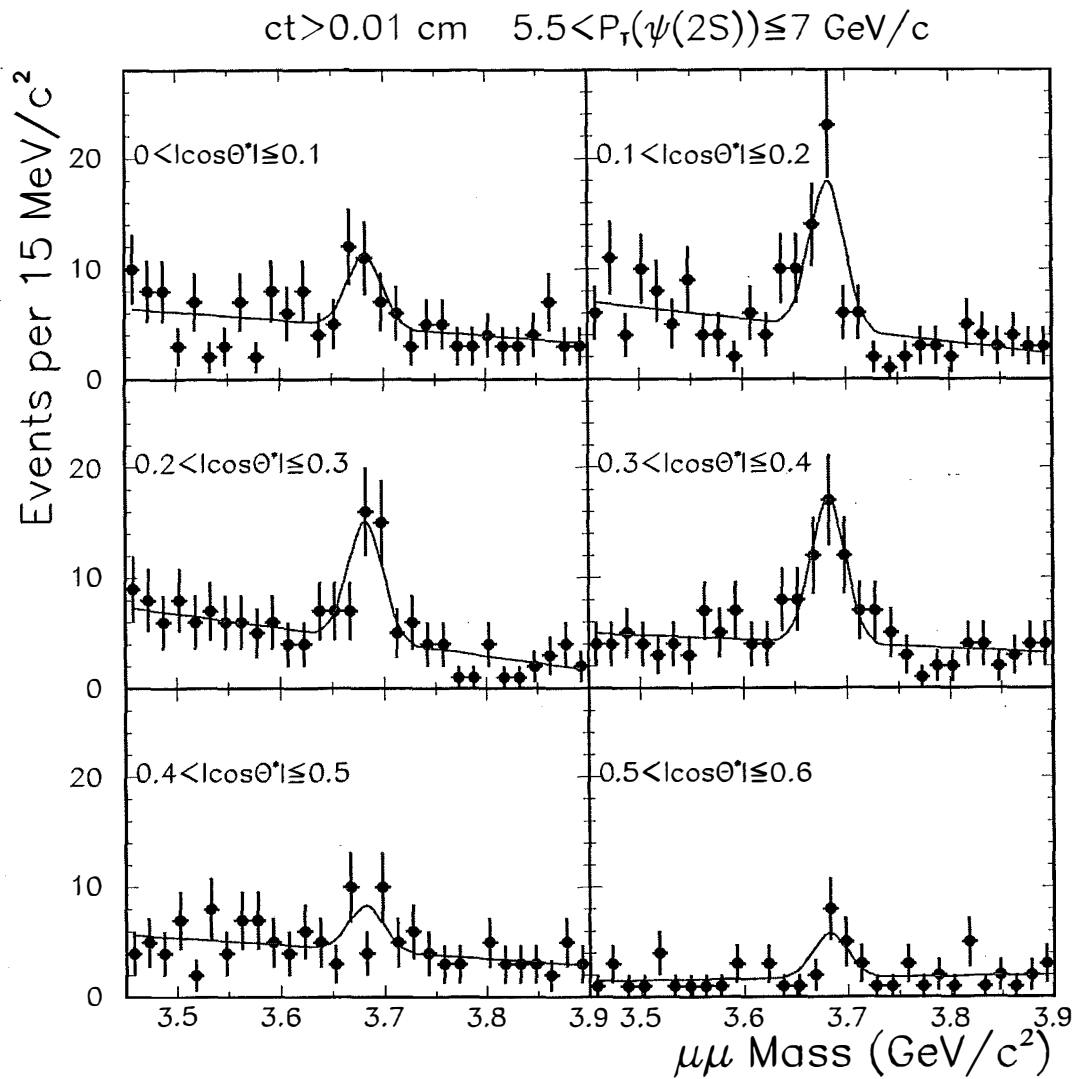
Figure 3-8: The invariant mass distributions of dimuons selected for the $\psi(2S)$ analysis. The $\psi(2S)$ candidates are required to have $5.5 < P_T \leq 7\,\mathrm{GeV/c}$ and $ct > 0.01$ cm. In each plot, the data are shown as points, whereas the line shows the result of a maximum-likelihood fit. The mass distributions are displayed in increasing $|\cos\theta^*|$ bins.
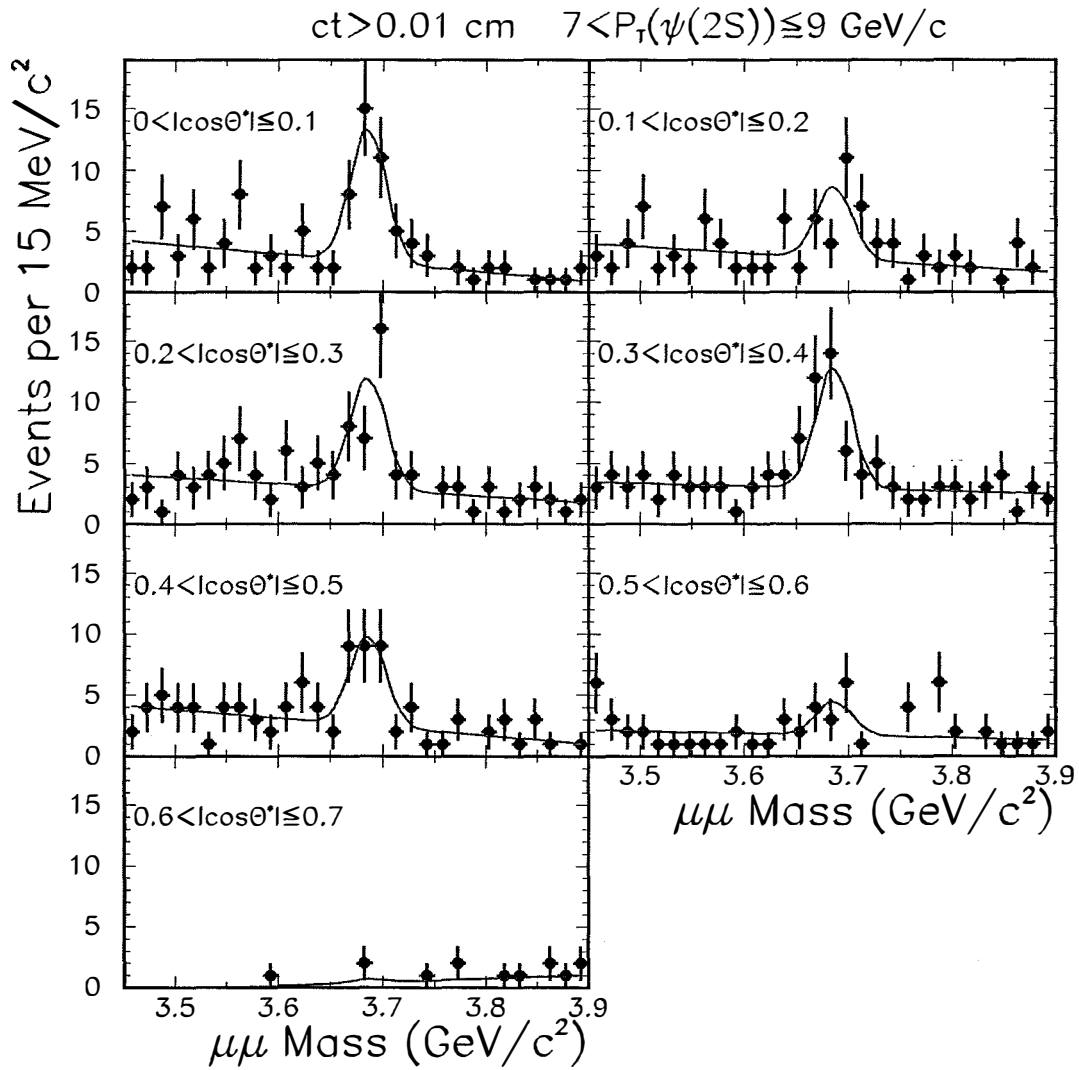
Figure 3-9: The invariant mass distributions of dimuons selected for the $\psi(2S)$ analysis. The $\psi(2S)$ candidates are required to have $7 < P_T \leq 9$ GeV/c and $ct > 0.01$ cm. In each plot, the data are shown as points, whereas the line shows the result of a maximum-likelihood fit. The mass distributions are displayed in increasing $|\cos\theta^*|$ bins.
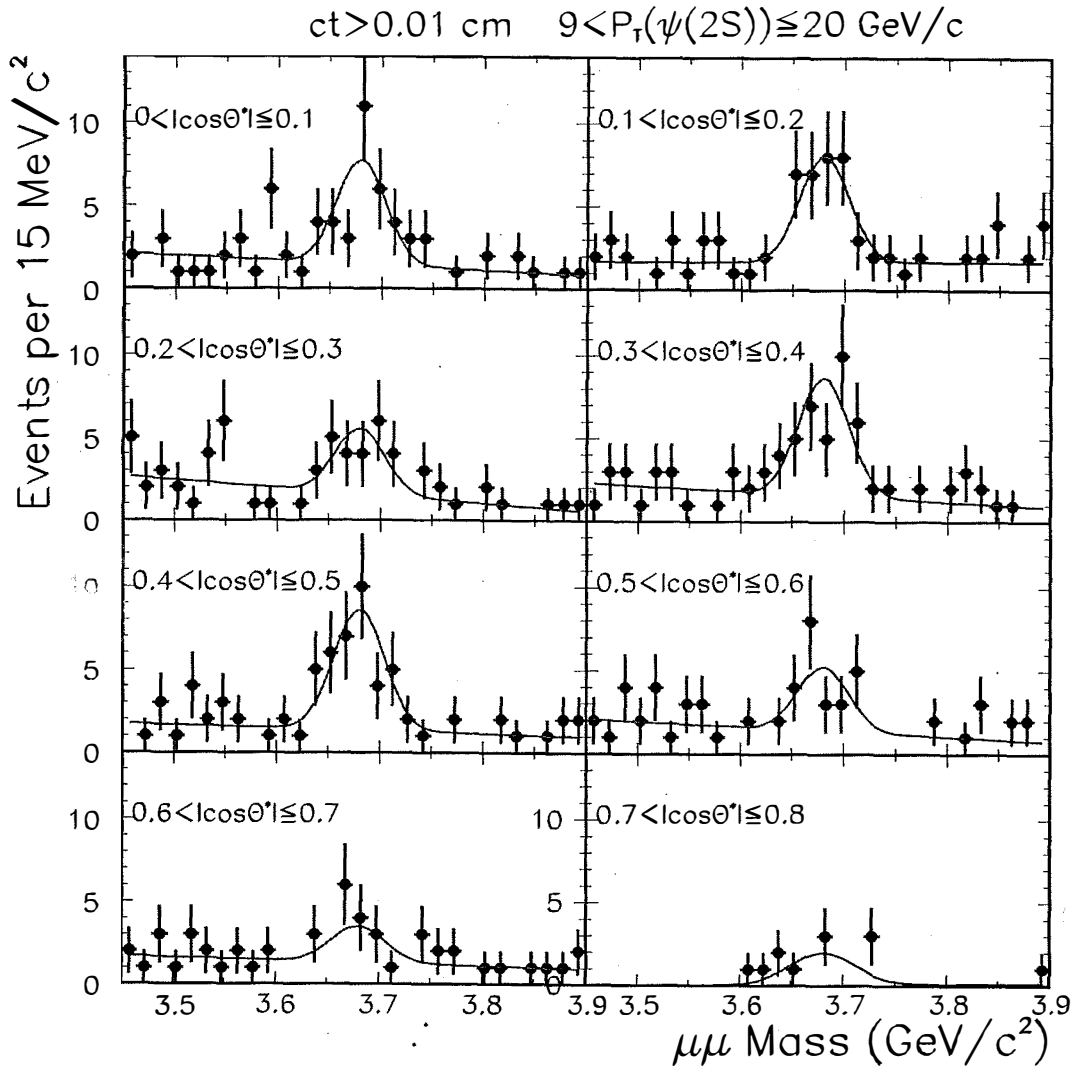
Figure 3-10: The invariant mass distributions of dimuons selected for the $\psi(2S)$ analysis. The $\psi(2S)$ candidates are required to have $9 < P_T \leq 20$ GeV/c and $ct > 0.01$ cm. In each plot, the data are shown as points, whereas the line shows the result of a maximum-likelihood fit. The mass distributions are displayed in increasing $|\cos\theta^*|$ bins.

$\|\cos\theta^*\|$	$5.5 < P_T \le 7$		$7 < P_T \le 9$		$9 < P_T \le 20$	
	Events	χ^2/dof	Events	χ^2/dof	Events	χ^2/dof
0.0-0.1	144.8±16.1	1.2	72.3±11.0	0.7	64.7±9.6	1.7
0.1-0.2	150.1±16.0	0.9	76.8±11.2	0.5	53.9±9.6	1.7
0.2-0.3	132.5±15.3	1.3	69.9±10.8	2.3	50.9±8.9	0.9
0.3-0.4	110.5±14.5	1.0	81.4±11.6	1.0	56.5±9.5	1.4
0.4-0.5	93.7±13.6	0.8	55.0±10.5	0.8	56.1±9.5	1.2
0.5-0.6	41.1± 9.3	1.1	43.6± 9.5	1.5	35.4±9.1	2.4
0.6-0.7	6.8± 3.6	0.8	16.4± 5.7	0.6	29.6±8.2	1.2
0.7-0.8					5.4±3.9	0.4

Table 3.3: The event yield and χ^2 per degree of freedom of the mass fits in individual $\|\cos\theta^*\|$ bins. The results are for the three different $P_T(\text{GeV/c})$ ranges in the low ct region.

$\|\cos\theta^*\|$	$5.5 < P_T \le 7$		$7 < P_T \le 9$		$9 < P_T \le 20$	
	Events	χ^2/dof	Events	χ^2/dof	Events	χ^2/dof
0.0-0.1	17.7±6.4	1.1	31.0±6.6	0.8	24.6±6.1	0.8
0.1-0.2	36.6±7.8	1.6	16.9±5.7	1.0	25.3±6.1	0.4
0.2-0.3	29.4±7.2	0.9	26.1±6.5	1.0	15.7±5.3	0.6
0.3-0.4	36.2±7.7	0.7	28.3±6.8	0.6	28.6±6.6	0.6
0.4-0.5	11.2±5.7	0.8	20.8±5.8	0.9	29.4±6.5	0.5
0.5-0.6	11.1±4.4	0.8	7.9±4.0	0.8	15.8±5.1	0.7
0.6-0.7			0.9±1.4	0.6	9.4±4.3	0.4
0.7-0.8					10.2±3.5	1.2

Table 3.4: The event yield and χ^2 per degree of freedom of the mass fits in individual $\|\cos\theta^*\|$ bins. The results are for the three different $P_T(\text{GeV/c})$ ranges in the high ct region.
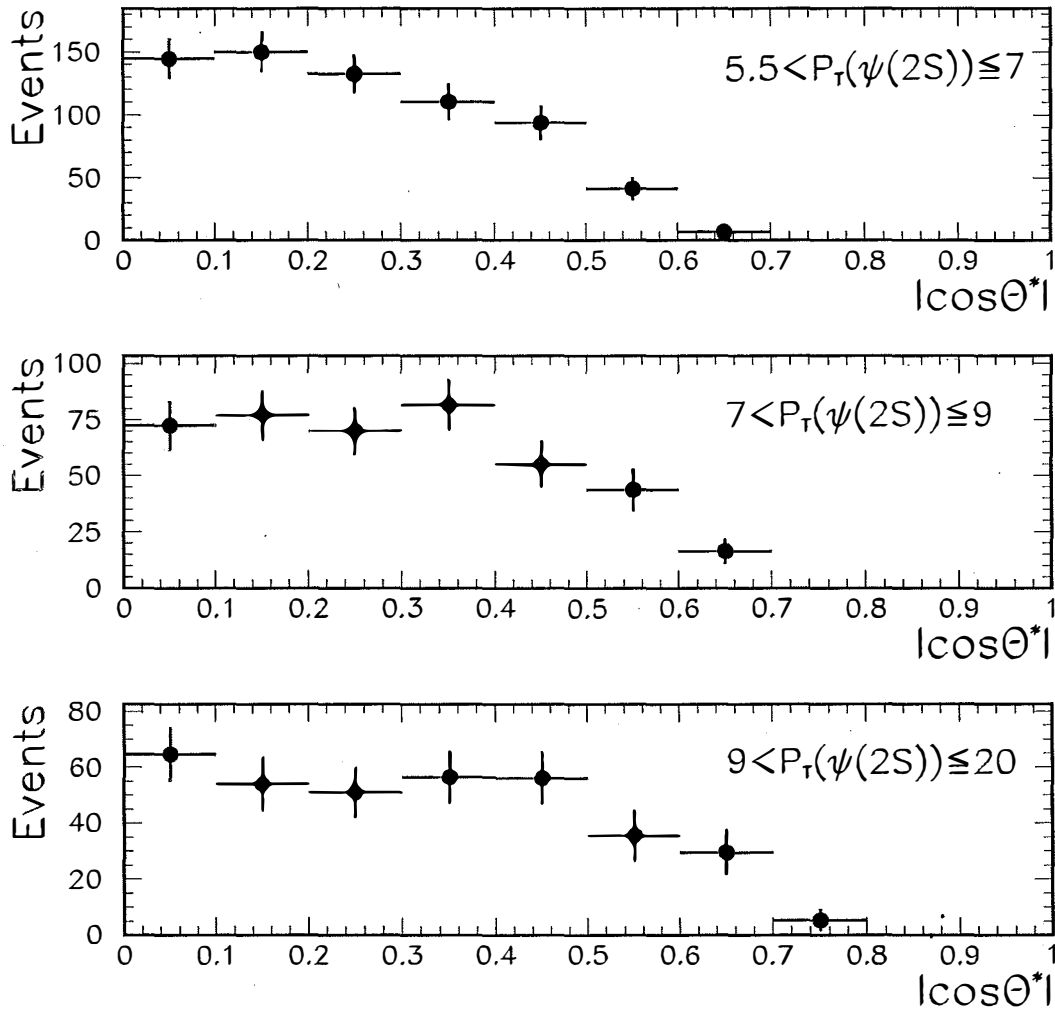
Figure 3-11: The $|\cos\theta^*|$ distributions for the three $\psi(2S)$ P_T bins in the low ct region. The signal event yield in each $|\cos\theta^*|$ bin is obtained from the fit to the mass distribution in the corresponding bin.
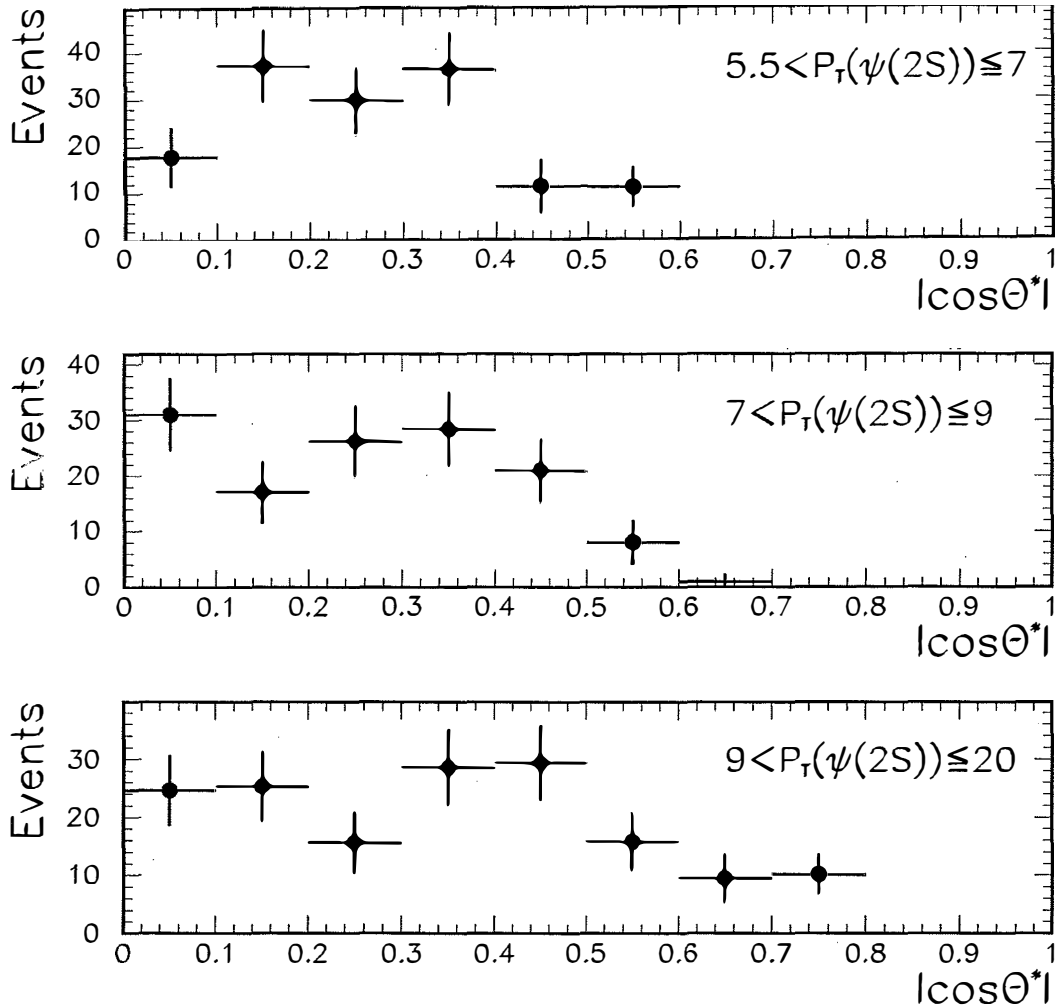
Figure 3-12: The $|\cos\theta^*|$ distributions for the three $\psi(2S)$ P_T bins in the high ct region. The signal event yield in each $|\cos\theta^*|$ bin is obtained from the fit to the mass distribution in the corresponding bin.

Chapter 4

Monte Carlo Sample

In order to fit the $\cos\theta^*$ distribution to extract the polarization, it is necessary to account for the event loss due to both the fiducial detector geometry and the kinematic and reconstruction selection requirements. This *effective* acceptance to $\psi(2S) \rightarrow \mu^+\mu^-$ decays is determined by Monte Carlo calculations. In this chapter, we describe the different steps in simulating the $\psi(2S)$ events, including the generation and the decay of $\psi(2S)$ mesons, the modeling of the CDF detector response to the final-state particles, and the simulation of the triggers relevant to the analysis. A method of fine tuning the simulated Monte Carlo events to match the data events is described at the end of this chapter.

4.1   Generation and Decay of $\psi(2S)$ Mesons

To determine the effective kinematic acceptance of $\psi(2S) \rightarrow \mu^+\mu^-$ decays, only the signal $\psi(2S)$ events need to be considered; in other words, a modeling of the underlying event and fragmentation particles is not relevant. Since the selection of the $\psi(2S)$ in the data uses requirements on the muons alone. The only possible effect of the rest of the particles in the event can arise in the reconstruction efficiency of these muons, once they satisfy the kinematic requirements. This is discussed in Section 4.2. Therefore, a fast generator is used to generate directly samples of $\psi(2S)$ events, each containing only a $\psi(2S)$ meson.

The $\psi(2S)$ mesons are generated with a uniform rapidity distribution over $|y| < 1$, and a uniform azimuthal angle distribution between 0 and 2π. The transverse momentum spectrum of the generated $\psi(2S)$ mesons is given by $C/(P_T^2 + M^2)^N$, where C, M and N are obtained by fitting this parameterization to the $\psi(2S) \to \mu^+\mu^-$ differential cross sections measured by CDF[8] using Run 1A data. The parameters M and N characterize the shape of the P_T parameterization. Their fitted values for the $\psi(2S)$ differential cross sections from prompt production and from B meson decays are listed in Table 4.1. The fits to the differential cross sections are shown in Figure 4-1. These cross sections were obtained by multiplying the inclusive $\psi(2S)$ cross section with $(1 - f_B)$ for the prompt and f_B for B decays, where f_B is the B fraction. To avoid edge effects due to smearing, a P_T range of $3.5 < P_T < 28.5$ GeV/c is used.

	Prompt	B-decay
M	2.67	6.31
N	2.48	2.50

Table 4.1: Parameters characterizing the shape of the measured $\psi(2S)$ P_T spectra from prompt production and from B meson decays.

Since the fractions of the prompt and the B-decay components in data will be determined[1] by a fit of the measured $\psi(2S)$ ct distribution, and will then be accounted for in the polarization fit, a simulation of the ct distribution is not necessary.

The generated $\psi(2S)$ mesons are fed into the QQ Monte Carlo program[60] from the CLEO experiment to decay the $\psi(2S)$ to dimuons. The default QQ matrix element for unpolarized $\psi(2S)$ with leading order radiative correction is used.

---

[1]The details can be found in Chapter 5
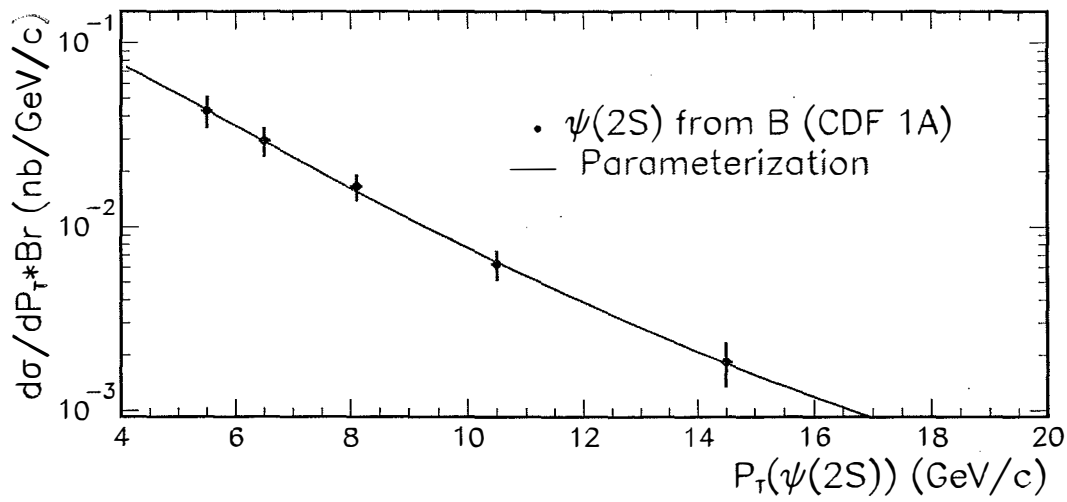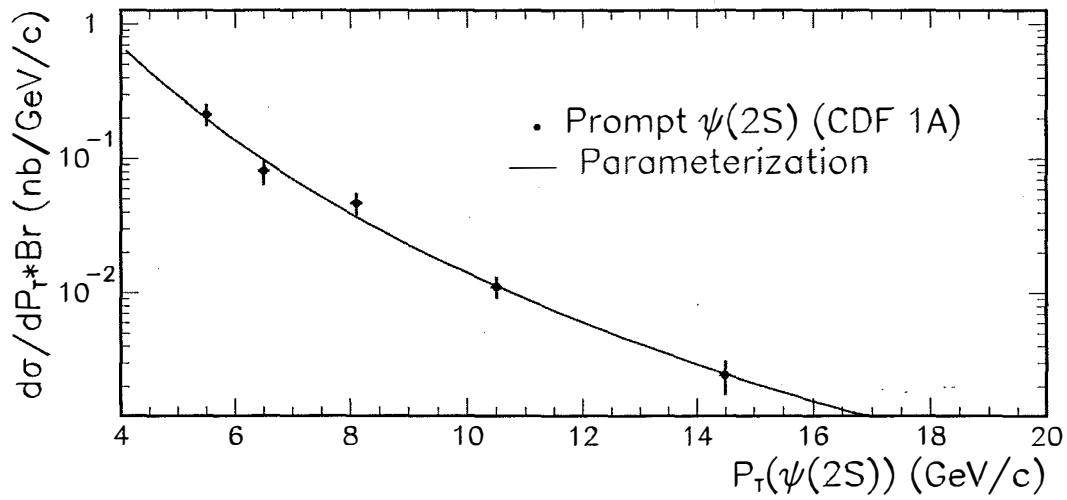
Figure 4-1: The differential cross sections for the $\psi(2S)$ mesons from prompt production (top) and from B decays (bottom). The data points are from the CDF published results obtained from Run 1A, overlaid with fits given by the parameterization $C/(P_T^2 + M^2)^N$.

4.2 Detector Simulation

Once the dimuons from the $\psi(2S)$ meson decays are produced, a Monte Carlo simulation of the CDF detector response is invoked. The simulation is performed by the QFL' program[61]. This program is a high-level simulator which directly produces the data structures identical to those in the real data. The model of the detector response is tuned to agree with the data. The differences in the running conditions between Run 1A and 1B, such as the detector geometry and the precise value of the magnitude of the magnetic field, are also taken into account.

QFL' models the detector by propagating the generated particles through the detector. The z location of the simulated event vertex is distributed according to a Gaussian probability density function. The mean and standard deviation of the Gaussian function are obtained by fitting the z distributions of the data event vertex for Run 1A and 1B separately. For Run 1A, the mean and standard deviation are determined to be -1.1 cm and 25.0 cm; whereas for Run 1B, they are 2.0 cm and 27.0 cm respectively. A correct modeling of the position in z of the event vertex is important due to its implications for the fiducial SVX acceptance.

Particles experience energy loss due to ionization and their trajectories are deflected by multiple Coulomb scattering through their interactions with the detector material. In the CTC, tracks for the charged particles are generated according to a parameterized efficiency and resolution, rather than simulating wire hits followed by the pattern recognition and reconstruction algorithms. For particles passing through the SVX and/or the CMU detectors, hits are generated, with their positions smeared by the detector resolution and multiple scattering effects. The combined procedures provide a fast and yet adequate simulation as our analysis requires both muon tracks to be reconstructed in the SVX.

The simulated information is then processed with the same reconstruction routines used to reconstruct data. The SVX tracking information is combined with the CTC information, where appropriate. Muon candidates are formed by matching hits in the CMU with the tracking information. The reconstruction of muons is found to be

highly efficient and essentially not affected by the presence of the tracks left by the other particles in the events. $\psi(2S)$ meson candidates are subsequently reconstructed from the two muon tracks, using the procedure described in Chapter 3.

4.3 Simulation of the Level 1 and 2 Triggers

The Level 1 and 2 muon triggers are described in Sections 2.2.6.1 and 2.2.6.2 respectively. The simulation of these two levels of triggers is performed with the standard software packages used throughout CDF: MU2TRG for Run 1A and DIMUTG[62] for Run 1B[2]. These packages check if each muon in the event is in the fiducial region of the trigger. Parameterizations of the measured muon trigger efficiencies are used to determine the probability that a given candidate dimuon event satisfies the trigger requirement. The Monte Carlo events are then selected using this probability.

The shape of the efficiency versus P_T curve for the Level 1 trigger is dominated by the effect of multiple Coulomb scattering. The trigger has a nominal P_T threshold of 3.3 GeV/c. However, due to the smearing effect of multiple Coulomb scattering, the threshold becomes an indirect P_T cut that rejects more low P_T muons than high. Figure 4-2 shows the resulting Level 1 CMU single muon trigger efficiency parameterization as a function of muon P_T[63].

The Level 2 dimuon trigger efficiencies are found to depend not only on P_T, but also on charge, pseudo-rapidity (η), azimuth, (ϕ), and time-integrated luminosity ($\int \mathcal{L} dt$)[64]. The geometry of the CTC wire planes gives rise to a slightly higher trigger efficiency for positive muon tracks than negative tracks. Also, muons with large track $|\eta|$ tend to deposit more charge on the CTC wires, subsequently enhancing the hit efficiency. This η dependence of the efficiency is found to be parabolic. The ϕ dependence of the efficiency is observed to be sinusoidal, and it is simply due to the offset of the beam from the geometrical center of the CTC. Finally, the decline in the CTC

---

[2]From Run 1A to Run 1B, the change in Level 1 trigger was small. On the other hand, the Level 2 trigger underwent extensive changes. For example, the CFT bin thresholds were shifted, and the principal triggers in Run 1B required two muon clusters at Level 2.
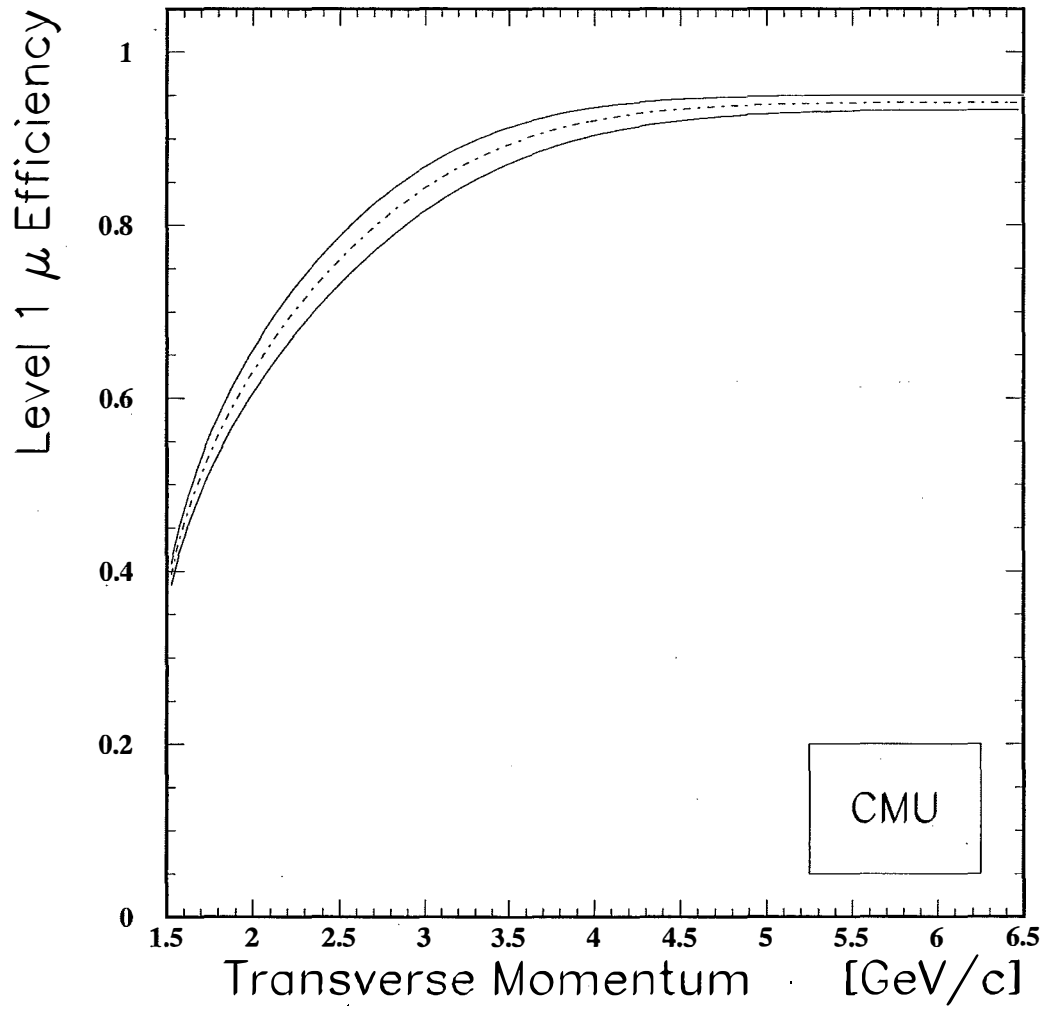
Figure 4-2: Efficiency of the Level 1 CMU trigger, as a function of muon transverse momentum. The dashed-dotted curve is the central values, and the solid curves indicate the uncertainties.

hit efficiencies (due to chamber aging) as a function of integrated luminosity causes a corresponding degradation in the Level 2 CFT pattern recognition efficiency[65]. This effect also enhances the curvature of the parabolic η-dependent efficiency. All these dependencies are accounted for in the trigger model. The Level 2 CMU trigger efficiency parameterization as a function of muon P_T is shown in Figure 4-3[63].

The Level 3 dimuon trigger is not included in the simulation because the trigger is highly efficient[3] and independent of the muon transverse momentum.

4.4 Acceptance

The simulated Monte Carlo events, where applicable, are subject to the same selection requirements imposed on the data (See Table 3.2). The $\cos\theta^*$ values of the selected Monte Carlo events are calculated and binned, forming effective acceptance distributions. Figure 4-4 depicts the $|\cos\theta^*|$ effective acceptance for prompt $\psi(2S)$ mesons in the three $\psi(2S)$ transverse momentum ranges: $5.5 - 7.0$, $7.0 - 9.0$, and $9.0 - 20.0$ GeV/c. In general, the acceptance is fairly flat and maximum at the low $|\cos\theta^*|$ region, but decreases to zero as $|\cos\theta^*|$ increases to 1. The depleted acceptance at large $|\cos\theta^*|$ is due to the fact that in this kinematic region, the direction of one of the decayed muons in the $\psi(2S)$ rest frame is close to the direction of the $\psi(2S)$ in the Lab frame. Subsequently one of the muons is boosted backwards with respect to its direction of motion, when transformed into the Lab frame, and can become too soft to pass the muon triggers. As the $\psi(2S)$ P_T increases, the soft muon becomes stiffer, and larger values of $|\cos\theta^*|$ become accessible. This trend is reflected in the figure. The $|\cos\theta^*|$ effective acceptance of $\psi(2S)$ from B decays is shown in Figure 4-5. The corresponding distributions for the three $\psi(2S)$ P_T bins have similar shapes to their prompt counterparts. Nevertheless, they are slightly more populated in the large $|\cos\theta^*|$ region since the $\psi(2S)$ P_T spectrum from B decay is stiffer than that from prompt production.

---

[3]The Level 3 dimuon trigger efficiency is measured to be 0.97 ± 0.02[66].
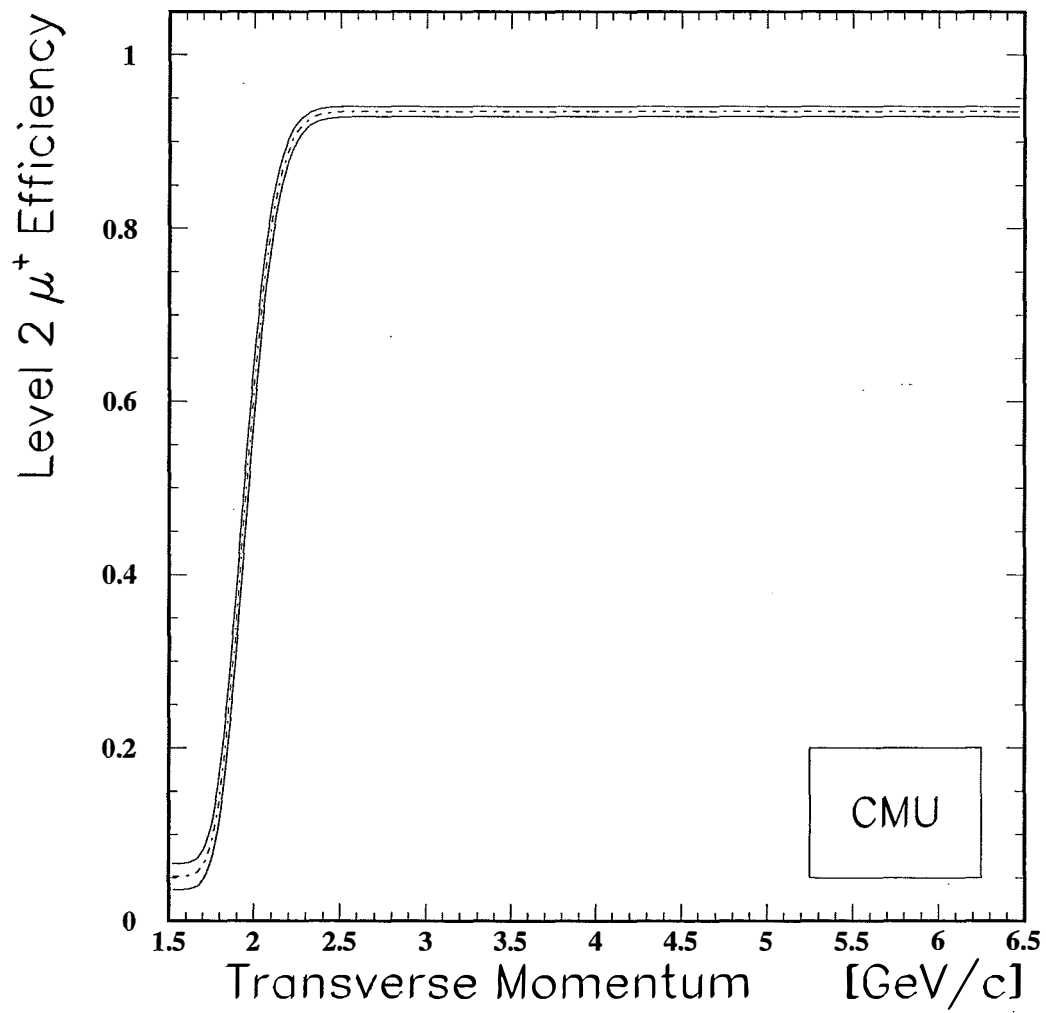
Figure 4-3: The Level 2 CMU trigger efficiency parameterization for positively
charged muons. The dashed-dotted curve is the central values, and the solid curves
indicate the uncertainties.
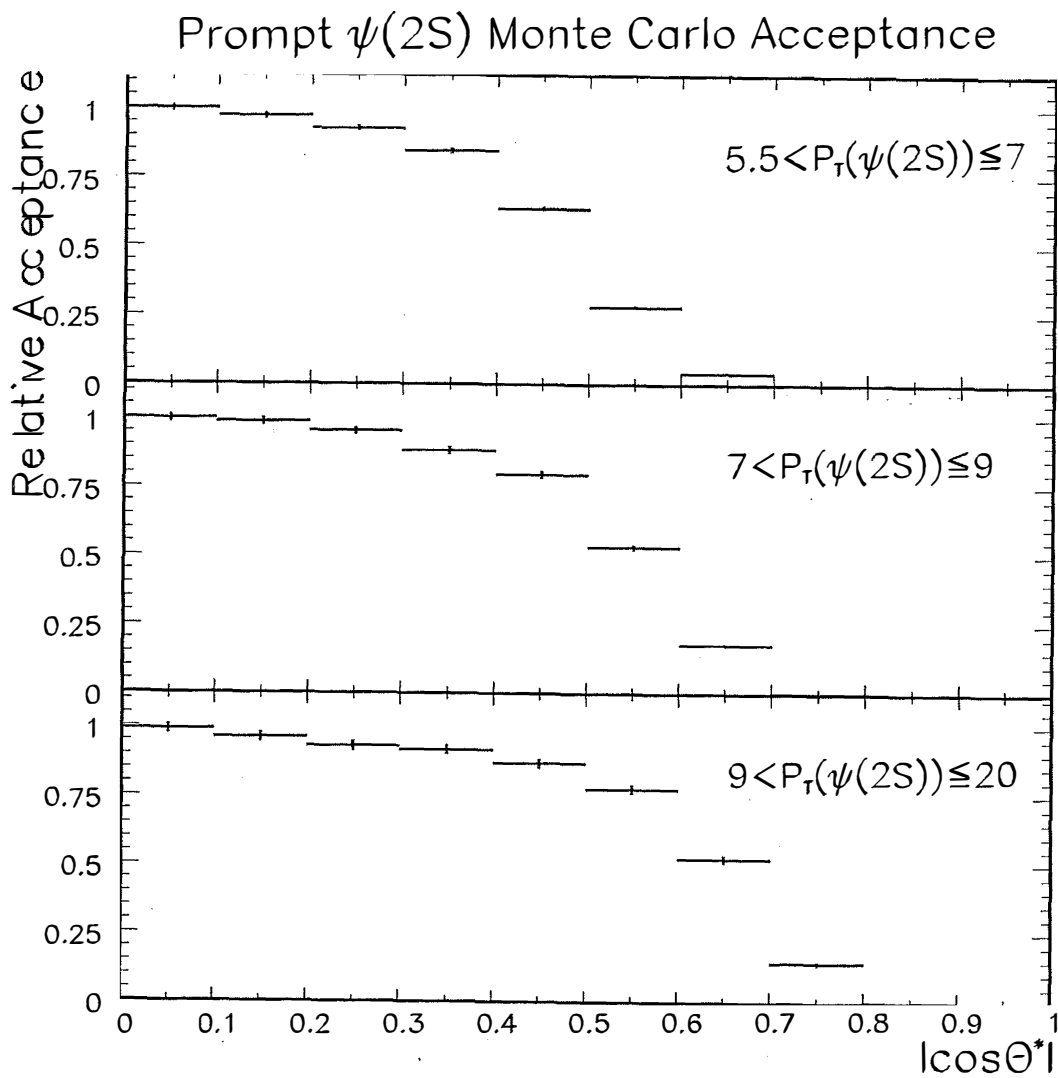
Figure 4-4: The $|\cos\theta^*|$ acceptance of prompt $\psi(2S)$ mesons in the three different P_T ranges.
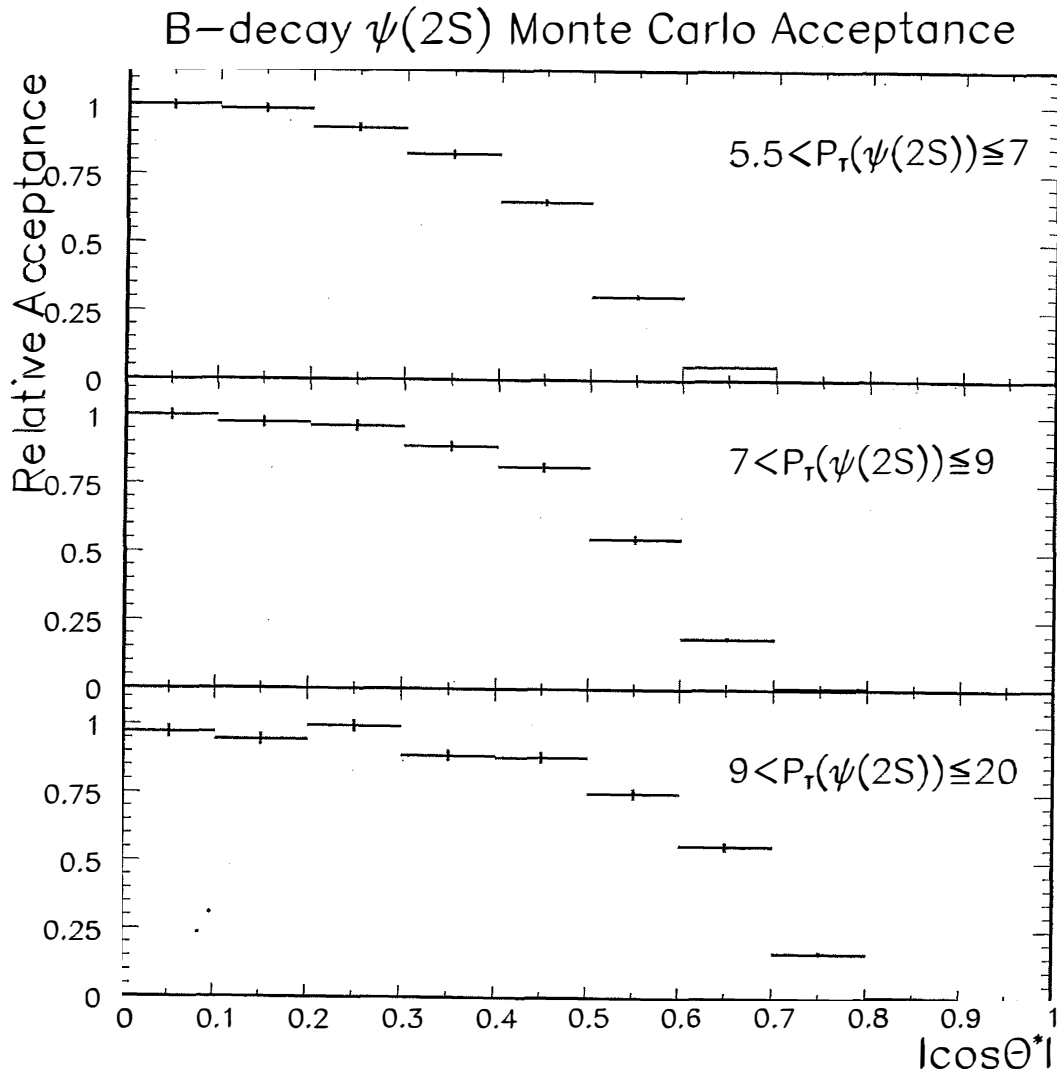
Figure 4-5: The $|\cos\theta^*|$ acceptance of $\psi(2S)$ mesons from B decay in the three different P_T ranges.

4.5   Tuning the Monte Carlo P_T Distribution

It is important to have a good model of the P_T distribution of $\psi(2S)$ production because it affects the acceptance in $|\cos\theta^*|$ through the correlation of $|\cos\theta^*|$ and P_T. A comparison of the P_T distributions between the prompt Monte Carlo and the background subtracted[4] data in the low ct region ($-0.1 < ct < 0.01$ cm) is shown in Figure 4-6. The $\psi(2S)$ P_T distribution for the data has been multiplied by the prompt fractions[5] to correct for the $\sim 10\%$ B-decay component. The Monte Carlo appears to have a slightly stiffer P_T distribution than the data. The discrepancy is attributed to the insufficient information in the P_T parameterization at the high P_T region. As discussed in Section 4.1, the $d\sigma/dP_T$ measurement used for the parameterization has a $\psi(2S)$ P_T range which extends only up to 17 GeV/c, therefore the information for $P_T > 17$ GeV/c relies on the extrapolation of the parameterization.

We tune the Monte Carlo to match the $\psi(2S)$ data by randomly discarding high P_T events in the Monte Carlo. To do this, the Monte Carlo P_T distribution is first parameterized as $e^{-\frac{P_T}{b}}$, where the parameter b controls the slope of the fall-off. The $\psi(2S)$ P_T distribution of the prompt Monte Carlo gives $b = 2.71$ GeV/c, whereas that of the B-decay Monte Carlo has $b = 4.0$ GeV/c. High P_T events are then thrown away to tune the distribution to follow $e^{-\frac{P_T}{b'}}$, where $b' = b + \delta b$ for some δb. The χ^2 between the data and the resulting Monte Carlo P_T distributions is calculated. Figure 4-7 shows the χ^2 as a function of various δb trials. These are fit to a parabola, $p_1(\delta b - p_2)^2 + p_3$, with equal bin weights. The value $\delta b = -0.57$ GeV/c is used as it gives minimum χ^2 between data and Monte Carlo P_T distributions, thus providing the best match between them. The one sigma error on δb is given by $\frac{1}{\sqrt{p_1}}$, which is 0.08 GeV/c. This one sigma error is later used to determine the systematic uncertainty due to this method of parameterizing the $\psi(2S)$ P_T distribution (see Section 7.2.2).

---

[4]The method of sideband subtraction is used to remove the background in the signal region, as discussed in Section 3.4.

[5]Chapter 5 will discuss the fitting of the measured $\psi(2S)$ ct distribution to determine the sample composition. The prompt fractions are listed in Table 5.2.

A similar procedure is used to tune the $\psi(2S)$ P_T distribution from the B Monte Carlo to match data. Figure 4-8 shows the P_T distributions of the background sub-tracted data in the high ct region ($ct > 0.01$ cm) and the B Monte Carlo before tuning. Here, the data P_T distribution of the $\psi(2S)$ has been multiplied by the B fractions ($(1 - p_+)$ in Table 5.2) such that it represents the P_T distribution arising purely from B decays. The χ^2 between the data and the Monte Carlo P_T distributions as a function of δb is shown in Figure 4-9. The value $\delta b = -1.19 \pm 0.27$ GeV/c is obtained.

Figures 4-10 and 4-11 show the $\psi(2S)$ P_T distributions of the data and the tuned Monte Carlo for prompt and B decays respectively. An overall improvement in agreement is seen. A comparison of the kinematic distributions between the data in the low ct region and the tuned prompt Monte Carlo for P_T, z, η, and ϕ are shown in Figures 4-12, 4-13, 4-14, and 4-15 respectively. The data distributions are background subtracted. A similar comparison of the corresponding distributions between the data in the high ct region and the tuned B-decay Monte Carlo are shown in Figures 4-16, 4-17, 4-18, and 4-19. The overall agreement between the simulated Monte Carlo and the data for these kinematic variables is quite good. This agreement is a cross-check that the full set of acceptance and efficiency corrections discussed above can be used to model the overall effective acceptance to $\psi(2S) \rightarrow \mu^+\mu^-$ decays, and therefore to model the experimental distributions for $|\cos\theta^*|$ in order to extract the $\psi(2S)$ polar-ization. This is the subject of Chapter 6. Before this discussion, though, we turn to the determination of the fractions of $\psi(2S)$ mesons from prompt production and B decays. This is the subject of the next chapter.
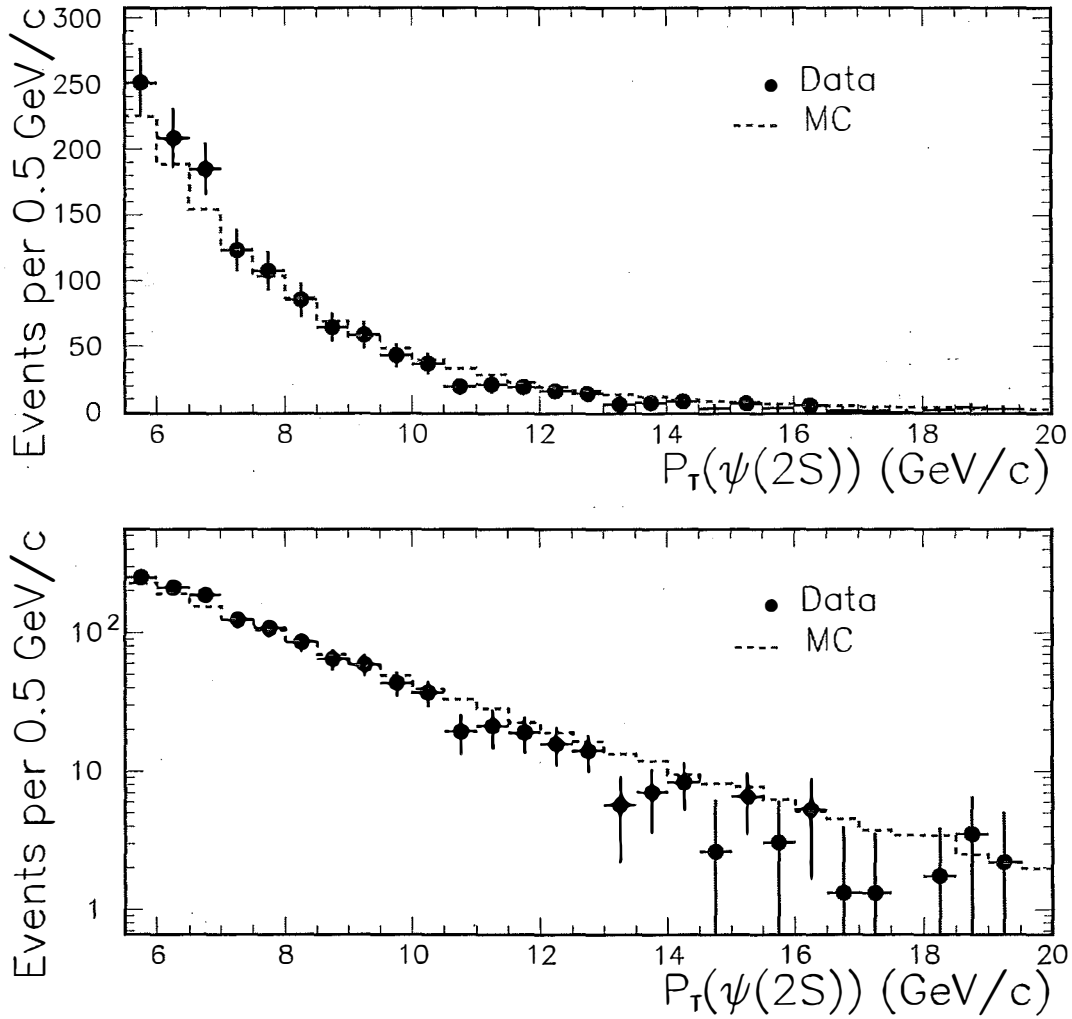
Figure 4-6: Comparison of the P_T distributions between data (background subtracted and multiplied by prompt fractions) in the low ct region and prompt Monte Carlo. The top plot is on a linear scale whereas the bottom plot is on a logarithmic scale.
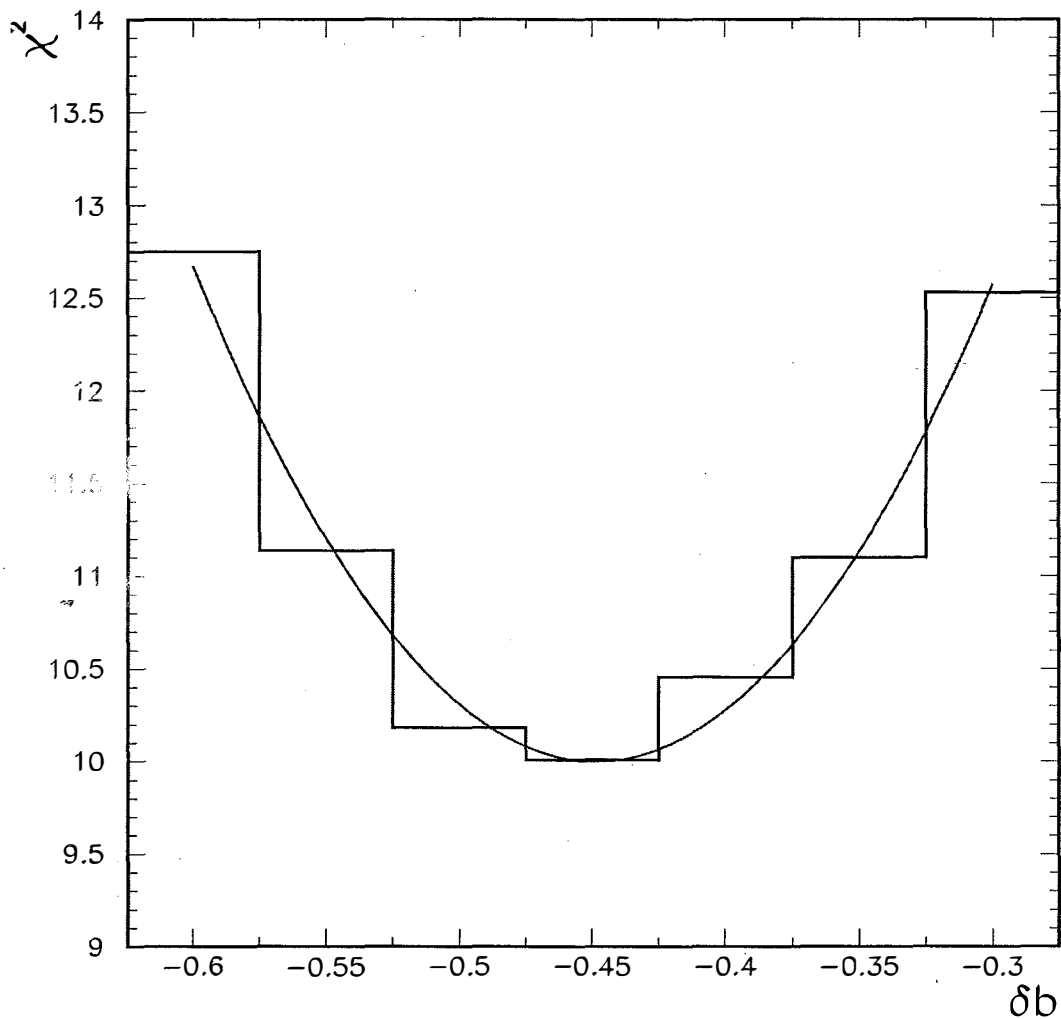
Figure 4-7: The χ^2 between data and prompt Monte Carlo P_T distributions as a function of δb, the P_T tuning parameter. The distribution is fitted to a parabola to extract the δb value that best describes the $\psi(2S)$ P_T distribution.
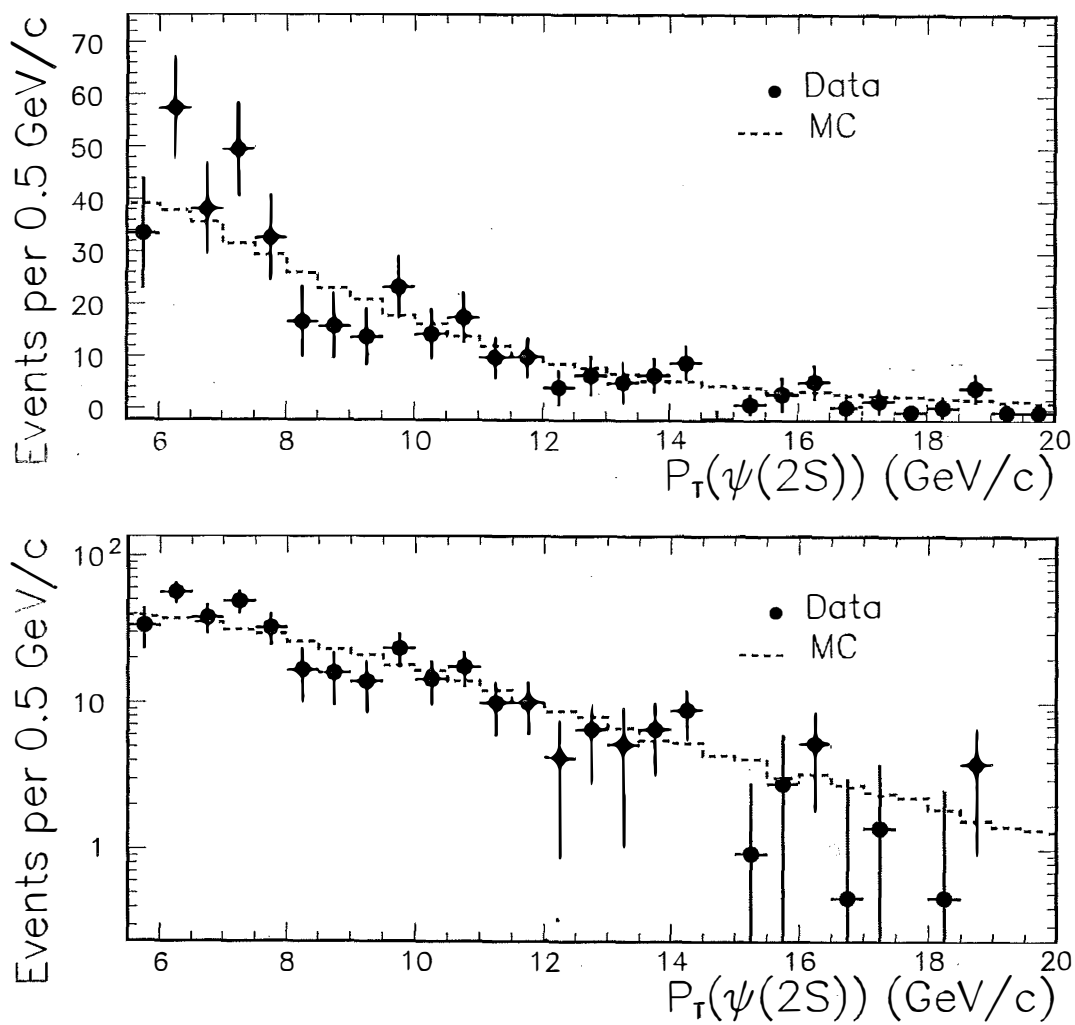
Figure 4-8: Comparison of the P_T distributions between data (background subtracted and multiplied by B fractions) in the high ct region and B Monte Carlo. The top plot is on a linear scale whereas the bottom plot is on a logarithmic scale.
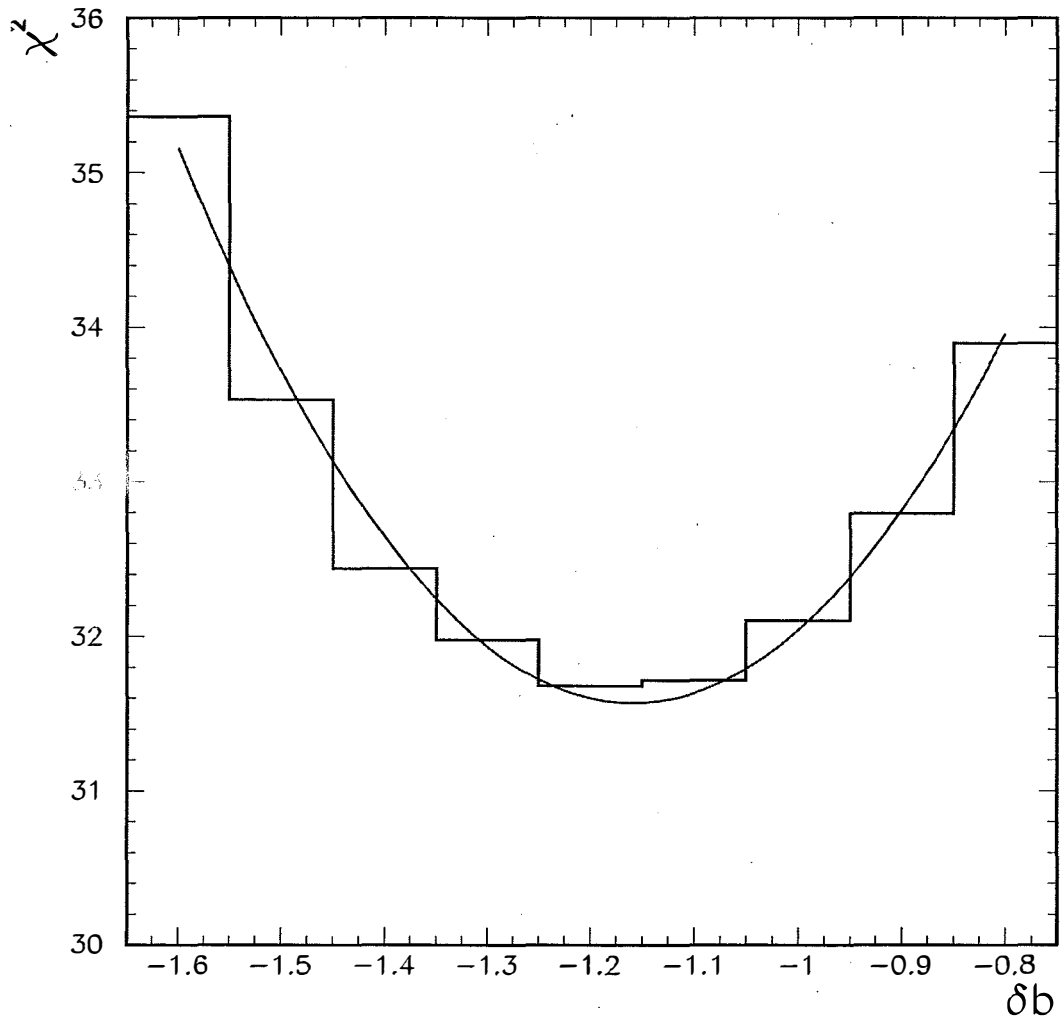
Figure 4-9: The χ^2 between data and prompt Monte Carlo P_T distributions as a function of δb, the P_T tuning parameter. The distribution is fitted to a parabola to extract the δb value that best describes the $\psi(2S)$ P_T distribution.
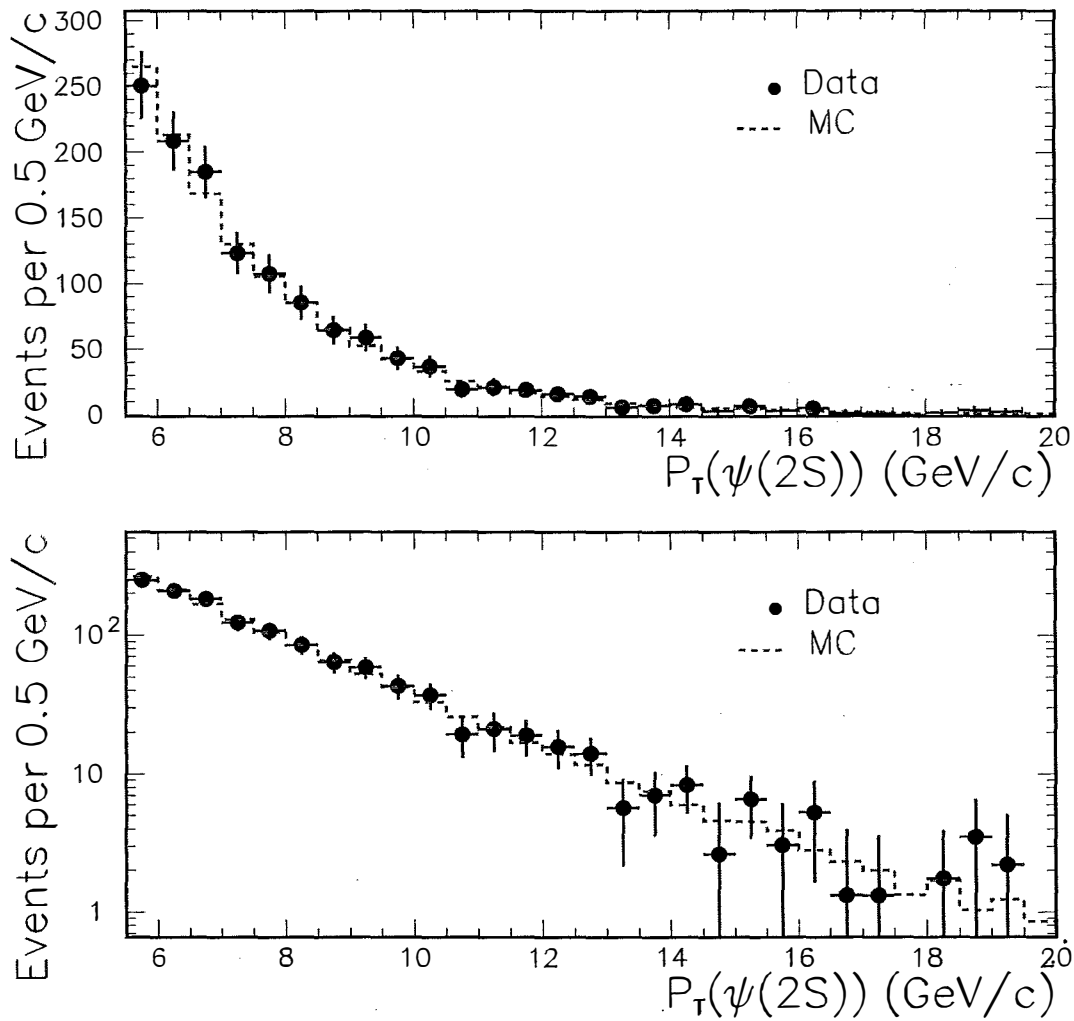
Figure 4-10: Comparison of the P_T distributions between data (background subtracted and multiplied by prompt fractions) in the low ct region and the tuned prompt Monte Carlo. The top plot is on a linear scale whereas the bottom plot is on a logarithmic scale.
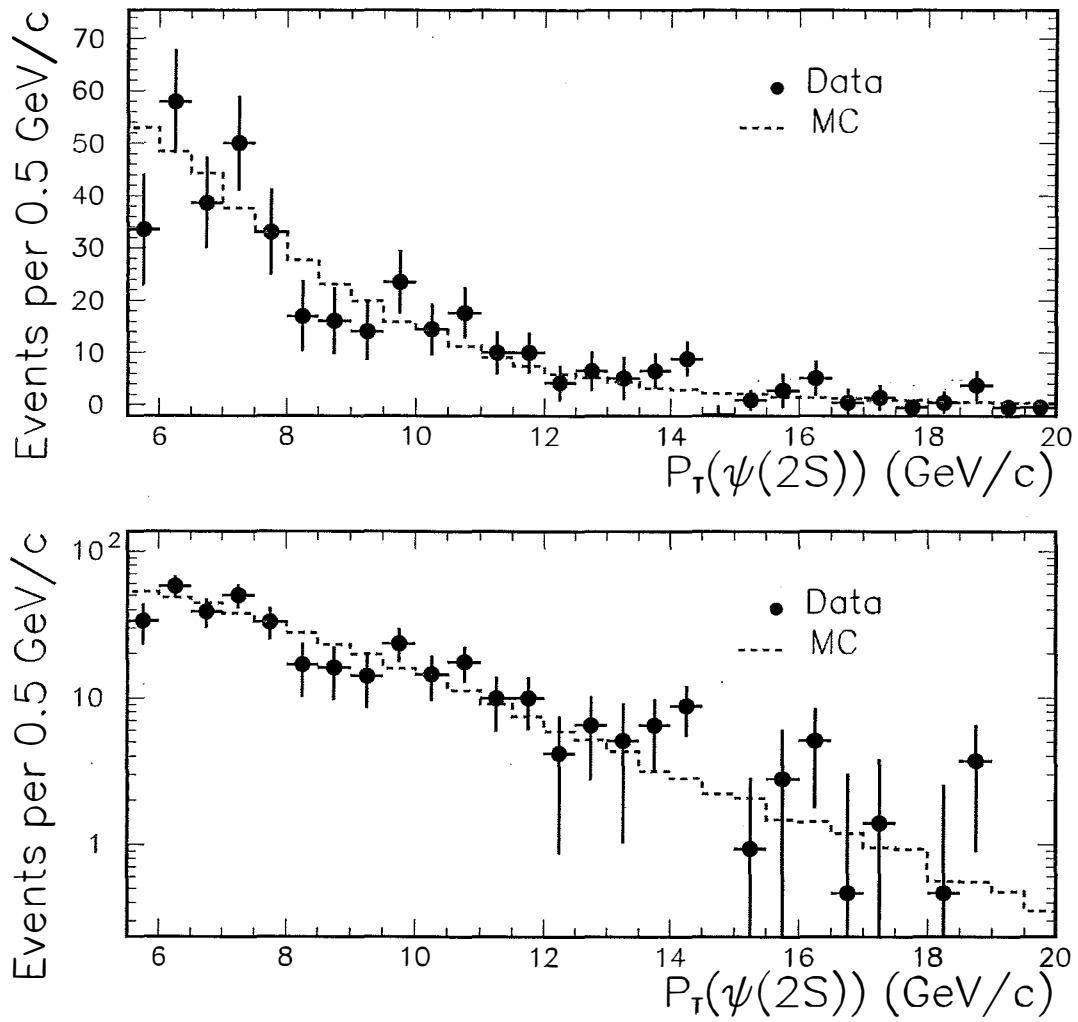
Figure 4-11: Comparison of the P_T distributions between data (background subtracted and multiplied by B fractions) in the high ct region and the tuned B Monte Carlo. The top plot is on a linear scale whereas the bottom plot is on a logarithmic scale.
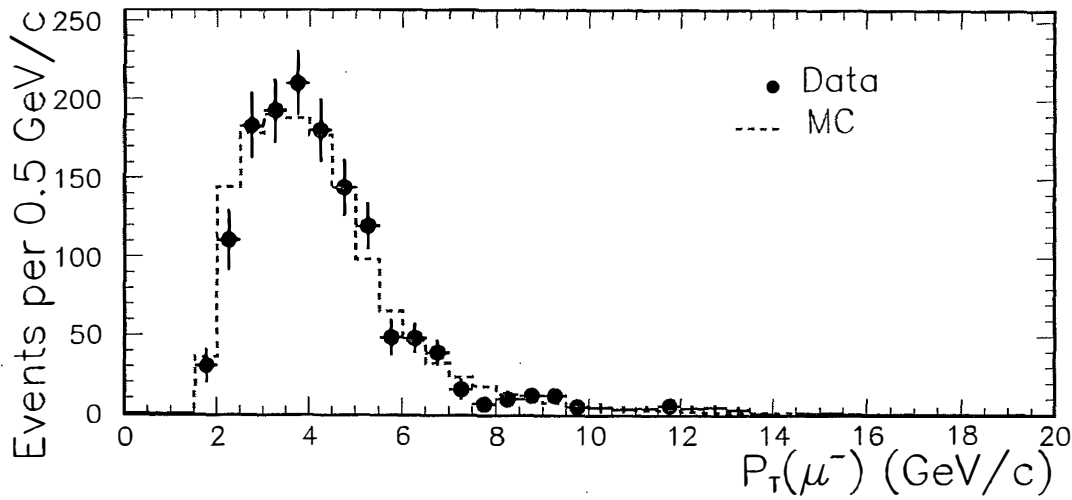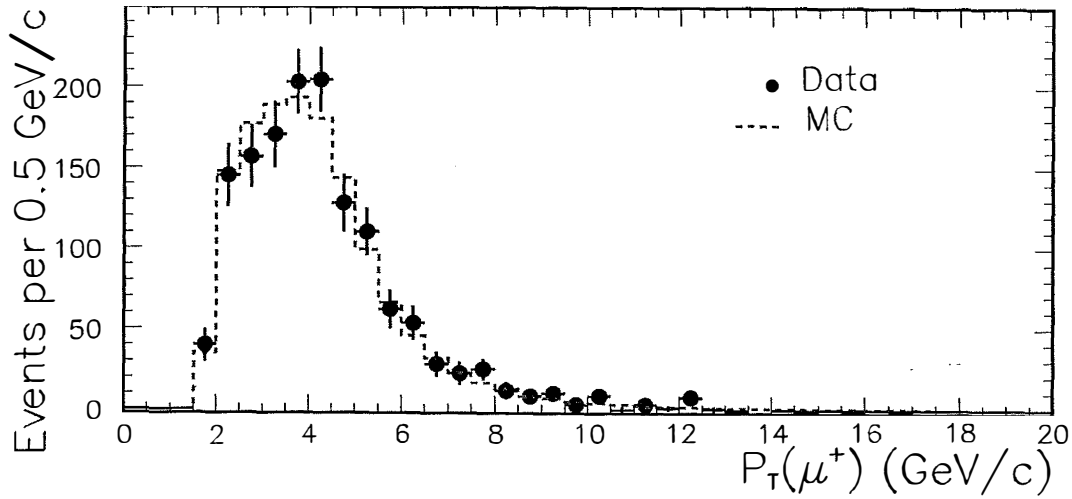
Figure 4-12: Comparison of the muons P_T distributions between data (background subtracted) in the low ct region (dark circles) and the tuned prompt Monte Carlo (dashed line).
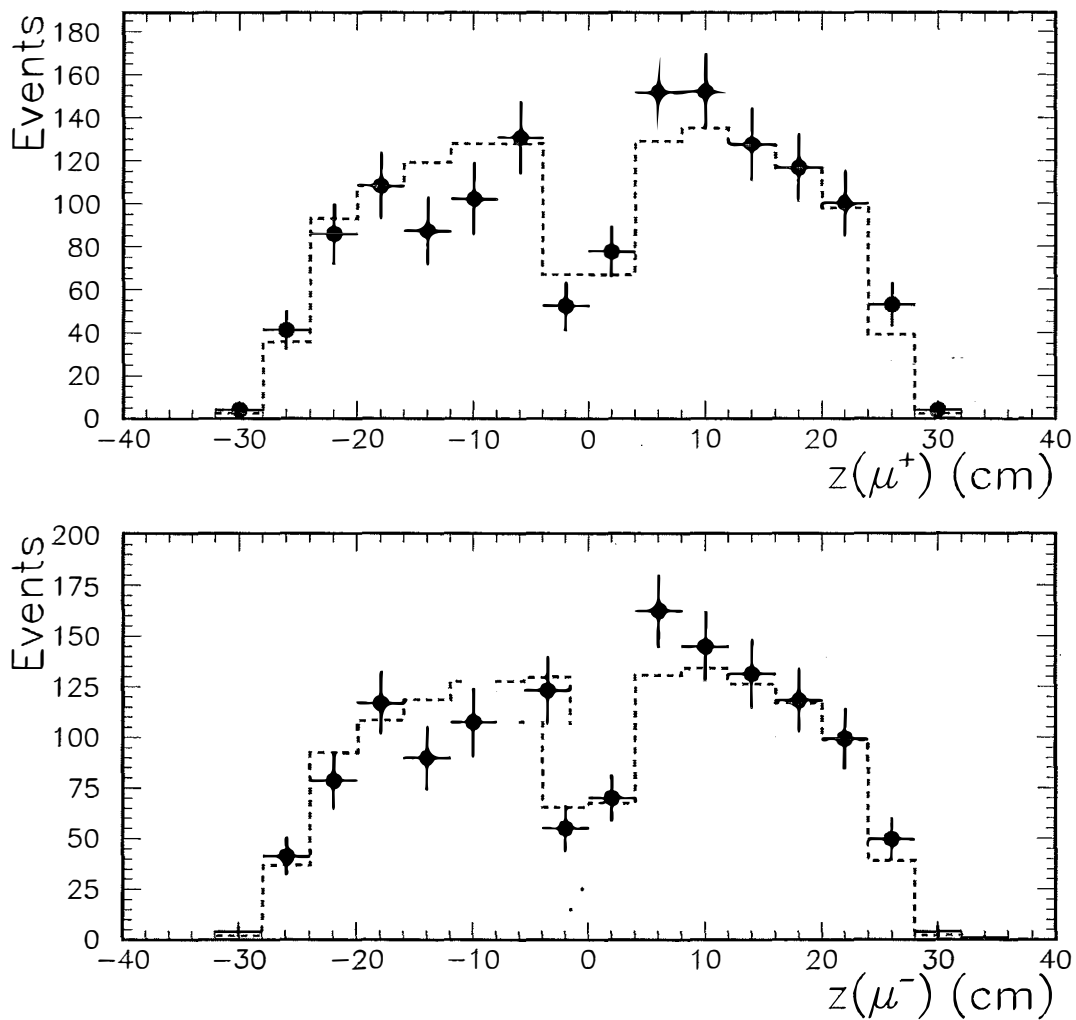
Figure 4-13: Comparison of the muons z distributions between data (background subtracted) in the low ct region (dark circles) and the tuned prompt Monte Carlo (dashed line).

112
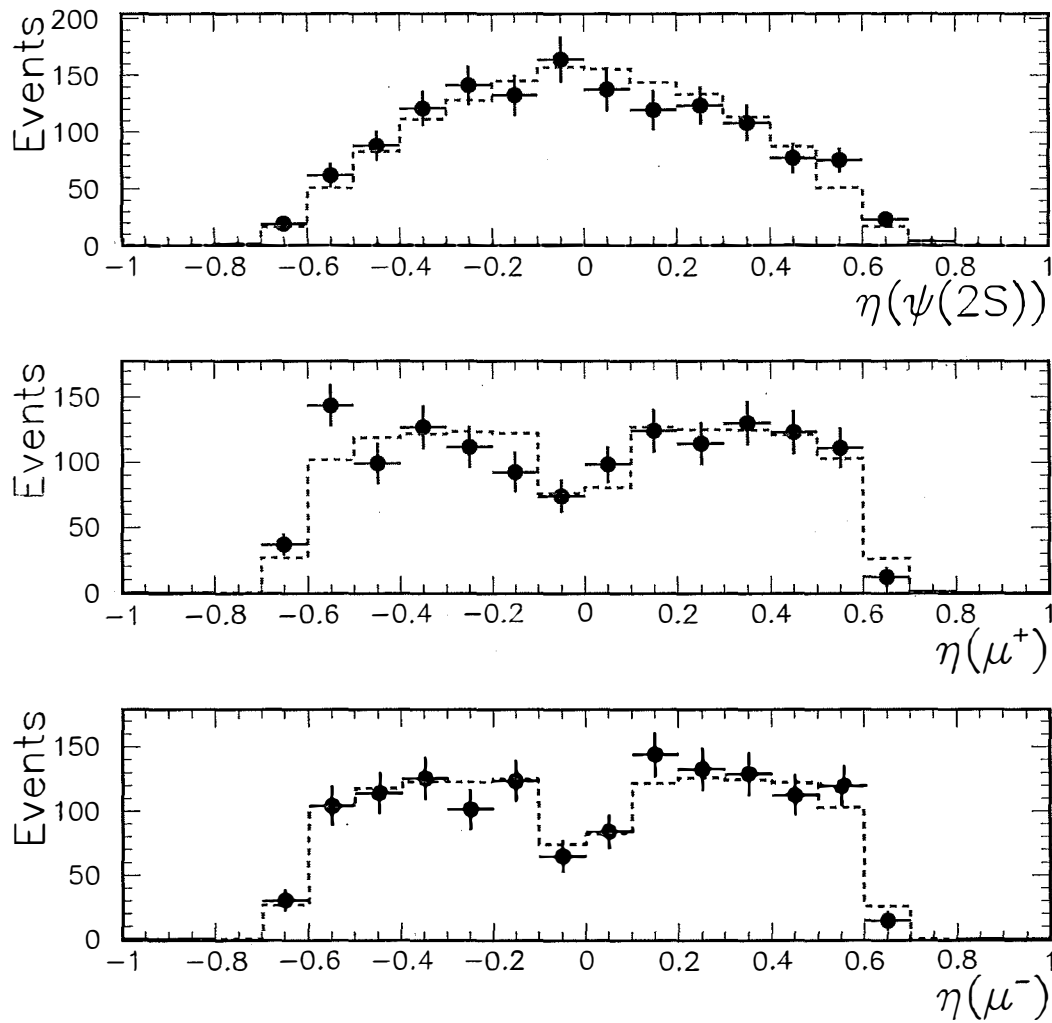
Figure 4-14: Comparison of the $\psi(2S)$ and the muons η distributions between data (background subtracted) in the low ct region (dark circles) and the tuned prompt Monte Carlo (dashed line).
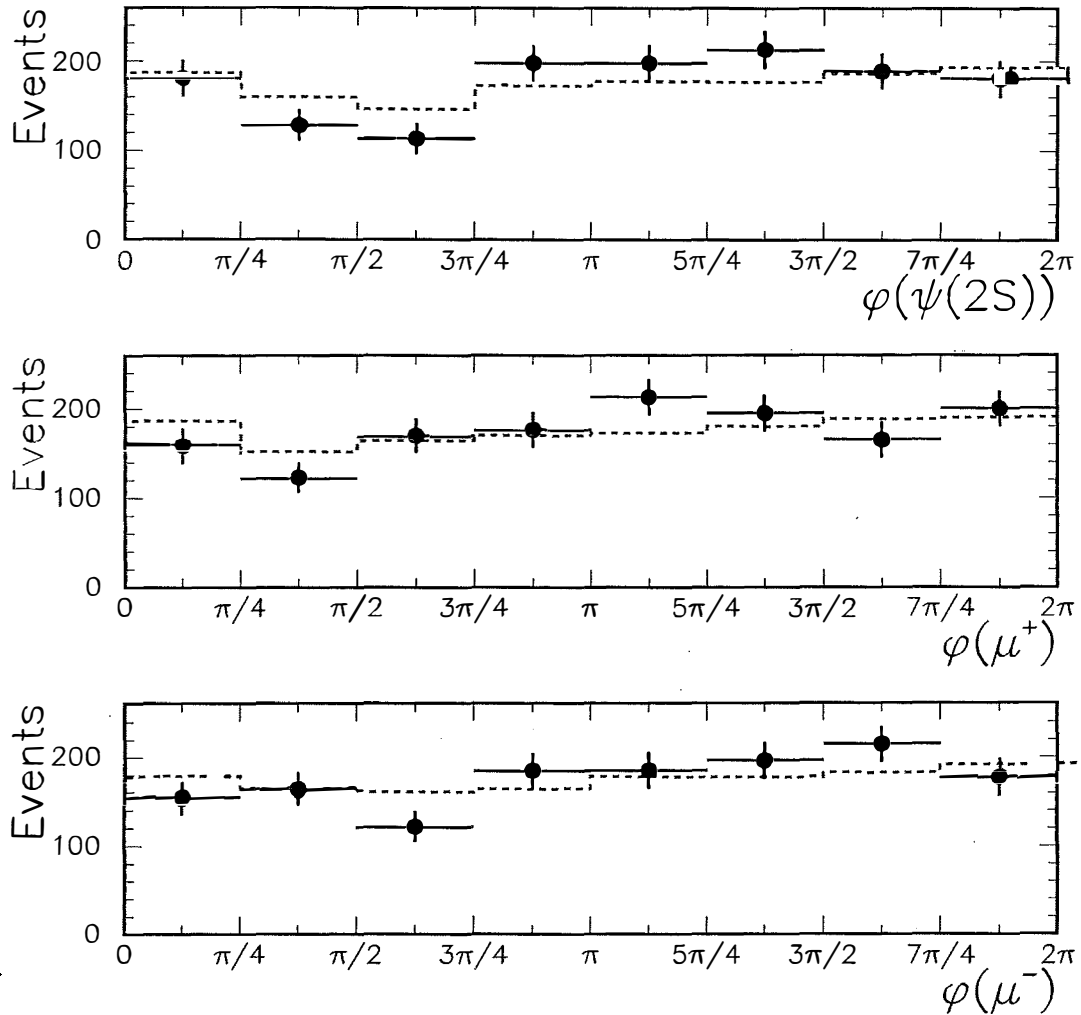
Figure 4-15: Comparison of the $\psi(2S)$ and the muons ϕ distributions between data (background subtracted) in the low ct region (dark circles) and the tuned prompt Monte Carlo (dashed line).
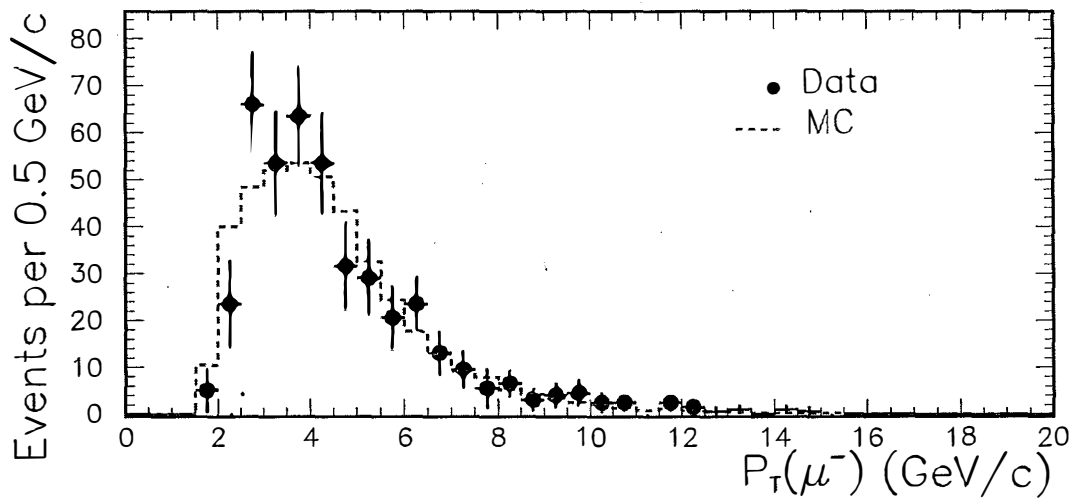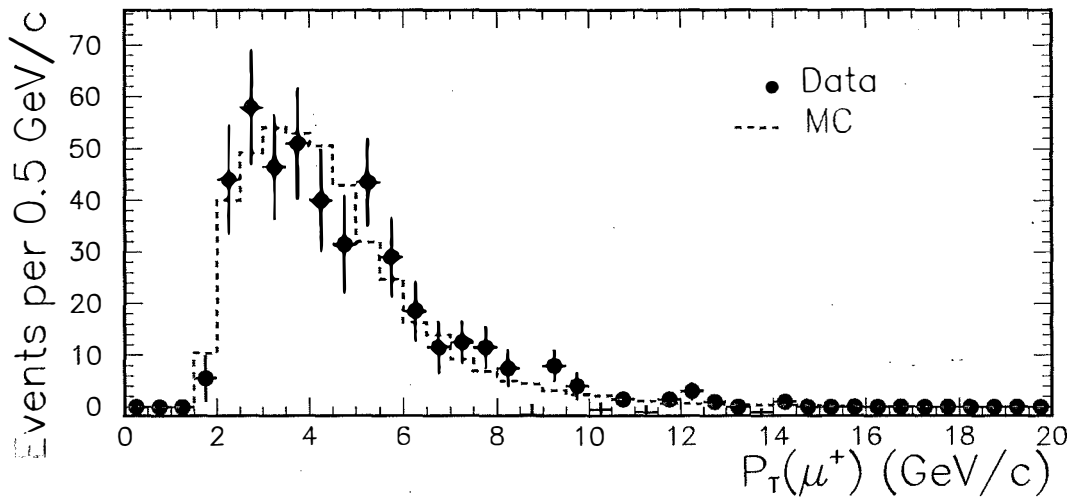
Figure 4-16: Comparison of the muons P_T distributions between data (background subtracted) in the high ct region (dark circles) and the tuned B-decay Monte Carlo (dashed line).
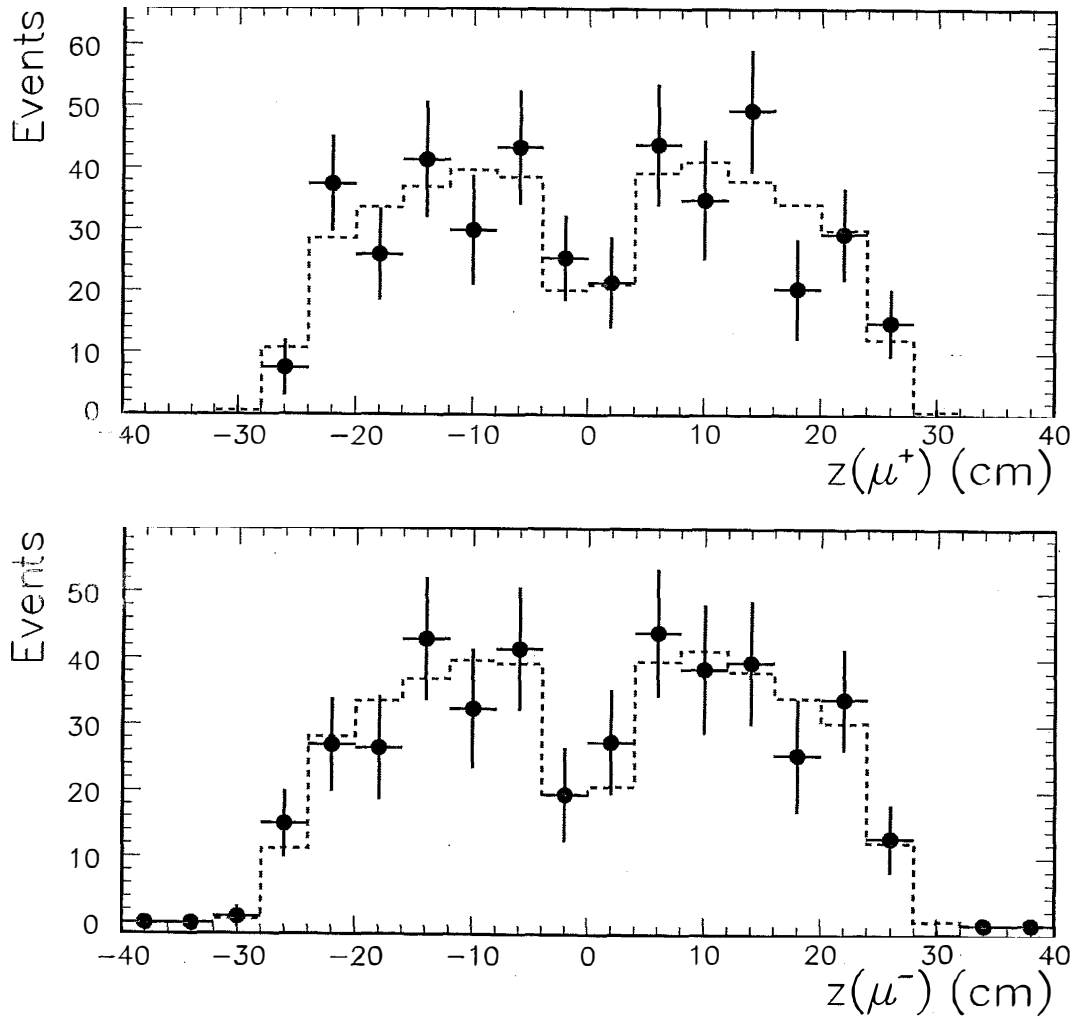
Figure 4-17: Comparison of the muons z distributions between data (background subtracted) in the high ct region (dark circles) and the tuned B-decay Monte Carlo (dashed line).
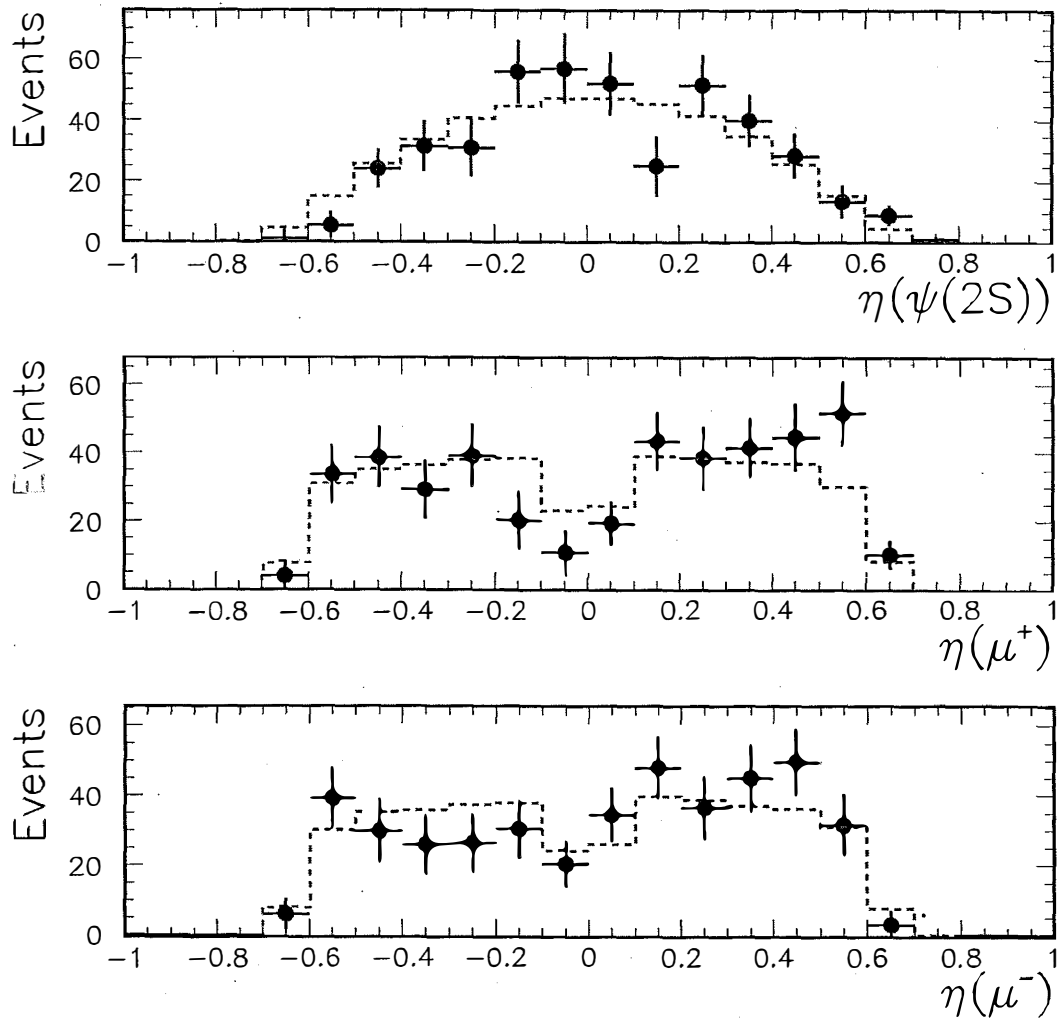
Figure 4-18: Comparison of the $\psi(2S)$ and the muons η distributions between data (background subtracted) in the high ct region (dark circles) and the tuned B-decay Monte Carlo (dashed line).
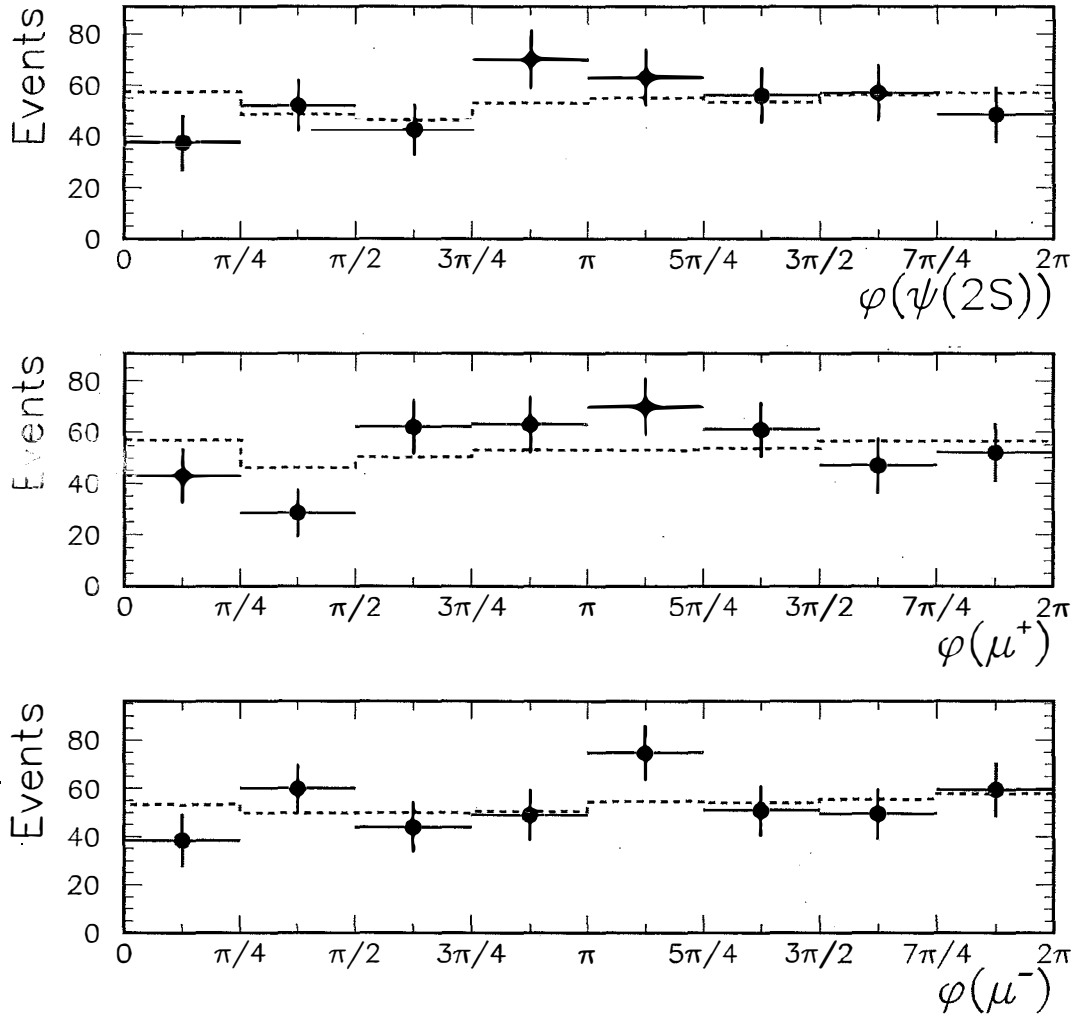
Figure 4-19: Comparison of the $\psi(2S)$ and the muons ϕ distributions between data (background subtracted) in the high ct region (dark circles) and the tuned B-decay Monte Carlo (dashed line).

Chapter 5

Lifetime Fit

As discussed in Chapter 1, $\psi(2S)$ mesons arise in $p\bar{p}$ collisions from both prompt pro-
duction and B decays. The two production mechanisms may yield, a priori, different
polarizations to $\psi(2S)$ and therefore the polarizations must be measured separately
for the two sources. Experimentally, prompt $\psi(2S)$ mesons are produced essentially at
the primary vertex, while $\psi(2S)$ mesons from B decays are characterized by displaced
secondary vertices due to the large proper decay length of B mesons ($ct \approx 450$ μm).
Therefore, the relative fractions of the prompt and the B-decay components in the
$\psi(2S)$ data sample can be determined by analyzing the proper decay length distribu-
tion of the $\psi(2S)$ mesons.

5.1   Primary Vertex

Primary vertex refers to the interaction point of the proton and anti-proton beams.
A precise knowledge of the primary vertex is clearly important to the calculation
of decay lengths resulting from displaced secondary vertices. The longitudinal (z)
coordinate of the primary vertex is determined on an event by event basis, while the
transverse ($x - y$) coordinates are obtained using a run-averaged[1] approach.

The z coordinate of a primary vertex is located using the information provided
by the VTX detector (see Section 2.2.3.2). A cluster of track segments reconstructed

---

[1] A "run" refers to a continuous data collection period, typically lasting several hours.

in the VTX detector are extrapolated to the beamline and fitted with the hypothesis that they originate from a common vertex. The intersection at the beamline gives the z position of the primary vertex.

During the later stages of Run 1B, the Tevatron was operated at higher instantaneous luminosities[2]. This resulted in higher primary vertex multiplicities. Events in Run 1B have an average of ≈ 2.5 primary vertices, about two times higher than that in Run 1A. This is usually not a problem as the VTX has a z resolution of about 1 mm and can differentiate multiple primary vertices in an event. In the events with more than one primary vertex, the vertex nearest in z to the reconstructed $\psi(2S)$ candidate is used.

The transverse $(x-y)$ coordinates of the primary vertices in an event are calculated using the measured run-averaged beam position. Over the course of a single data-taking run, the transverse beam profile was found to be quite stable, varying less than 10 μm in either the x or y directions[67]. Using a run-averaged beam position instead of reconstructing it independently for each event also avoids bias caused by fluctuations in track multiplicities and event topologies in individual events. For example, in B events, the presence of decay products of the long-lived B mesons can shift the $x - y$ locations of the reconstructed primary vertices[3].

The run-averaged beam position is obtained by combining the SVX and CTC information of all the tracks collected in a single run. Figure 5-1 shows the beam profile for a sample run. It indicates that the beam is not in general parallel to the z axis of the CDF detector. The beam slope is typically 6μm/cm in x and -3μm/cm in y[67]. The slopes and intercepts of the run-averaged beam position are combined with the event-by-event z locations of the vertices in an event to determine the transverse positions of those vertices. Using this algorithm, the uncertainties on the transverse beam positions are dominated by the size of the beam, which is Gaussian distributed

---

[2]Typical peak luminosity was 16×10^{30}cm^{-2}/s in Run 1B.

[3]In principle, the z locations of the primary vertices can also be shifted. However, most of the B mesons produced in CDF have large transverse momenta, and thus travel largely in the transverse plane. Furthermore, the CDF detector has better resolution in the $x - y$ plane than in z direction, making any transverse shift more important.

with a width of 40 μm in both transverse directions.

5.2   Measurement of ct

The $\psi(2S)$ mesons from B decays are characterized by displaced secondary vertices. This is because at the energy scale of the Tevatron, B mesons are produced with considerable transverse momenta and will often travel distances of the order of 1 mm before decaying. The decay point is called the secondary vertex, to be distinguished from the primary vertex where a B meson is produced. The distance between the primary vertex and the secondary vertex is the decay length, as illustrated in Figure 5-2.

Due to its very small lifetime ($\approx 10^{-21}$ s), the $\psi(2S)$ meson from B decays essentially decays at the secondary vertex. In our case, therefore, the secondary vertex can be determined by extrapolating the two tracks left by the decayed muons back to their point of intersection. In order to obtain an accurate measurement of the decay length, both muons are required to be reconstructed in the SVX. Each muon track is also required to have at least 3 hits in the SVX. As described in Section 2.2.3.1, the SVX detector measures tracking information in the transverse plane with a resolution of ≈ 40 μm. This indicates that a precise measurement of the transverse decay length is indeed possible.

The proper decay length, ct, of a B meson is related to the transverse decay length L_{xy} as follows:

$$ct = \frac{cL_{xy}}{P_T(B)/m(B)} \tag{5.1}$$

where $m(B)$ and $P_T(B)$ are the mass and the transverse momentum of the B meson. One caveat is that we only reconstruct the $\psi(2S)$ meson, not the B meson, and therefore $P_T(B)$ is not known. Nevertheless, the $\psi(2S)$ meson takes most of the momentum of the B meson, and the variation on this momentum fraction is not large. Therefore, we can still use the $\psi(2S)$ quantities to calculate the proper decay length:

$$ct = \frac{cL_{xy}}{[P_T(\psi(2S))/m(\psi(2S))] \cdot F_{corr}(P_T(\psi(2S)))} \tag{5.2}$$

121
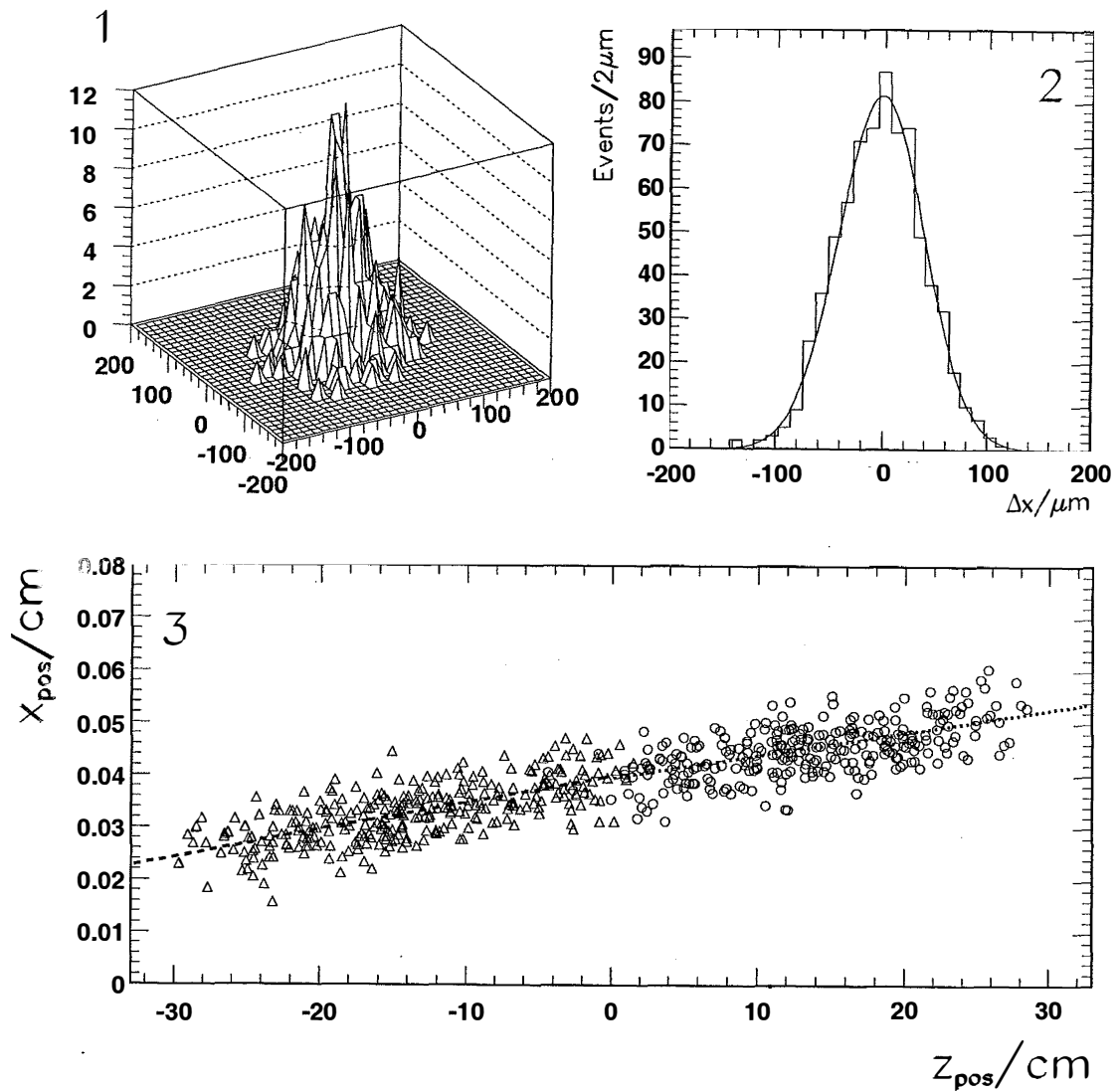
Figure 5-1: Beam profile for a sample run as measured by the SVX. (1) shows the distribution of primary vertices in the $x - y$ plane, after correcting for the spread in z position. (2) shows the beam profile projected onto the x-axis. (3) shows the movement of the beam in the x direction as z changes.

where $m(\psi(2S))$ and $P_T(\psi(2S))$ are the reconstructed $\psi(2S)$ mass and transverse momentum. Here F_{corr} is a correction factor to account for the fact that we are using $P_T(\psi(2S))$ instead of $P_T(B)$. This correction factor is calculated by averaging over Monte Carlo events of $B \to \psi(2S)X$ decays over a given P_T region[8]:

$$F_{corr}(P_T(\psi(2S))) = \left\langle \frac{P_T(B)/m(B)}{P_T(\psi(2S))/m(\psi(2S))} \cos\phi \right\rangle, \qquad (5.3)$$

where ϕ is the angle between the $\psi(2S)$ direction and the B direction in the transverse plane as depicted in Figure 5-2. In Figure 5-3, the correction factor is plotted as a function of the $\psi(2S)$ P_T. It has only a slight dependence at low P_T and quickly plateaus to a value of about 78%. A distribution of the correction factor, for $10 < P_T(\psi(2S)) < 11$ GeV/c as an example, is displayed in Figure 5-4. This shows the variation on F_{corr} is not large.

5.3 Fitting the ct Distribution

An unbinned likelihood fit [68] is used to fit the ct distributions. To determine the background shape, the ct distribution of events in the sidebands of the mass distribution is used. 100 MeV/c^2 regions above and below the mass peak are used as sidebands. The background is modeled by a Gaussian and three exponential functions. The Gaussian function represents the prompt background component such as punch-through fake muons coming from the primary vertex. Prompt background events have decay times consistent with zero lifetime. However, their reconstructed ct's differ from zero by a Gaussian smearing due to the detector resolution. The three exponentials describe the long-lived background component which can arise, for example, from decay-in-flight muons associated with displaced tracks. Since long-lived background events tend to have positive ct, the exponential describing the $ct > 0$ region has a different slope from that describing the $ct <$ region. The background functional form B_k used for the fit can thus be schematically written as:

$$B_k = (1-f_+-f_--f_{sym})G(ct; \rho\sigma)+f_+E(ct; \lambda_+)+f_-E(ct; \lambda_-)+f_{sym}E(ct; \lambda_{sym}) \quad (5.4)$$

123
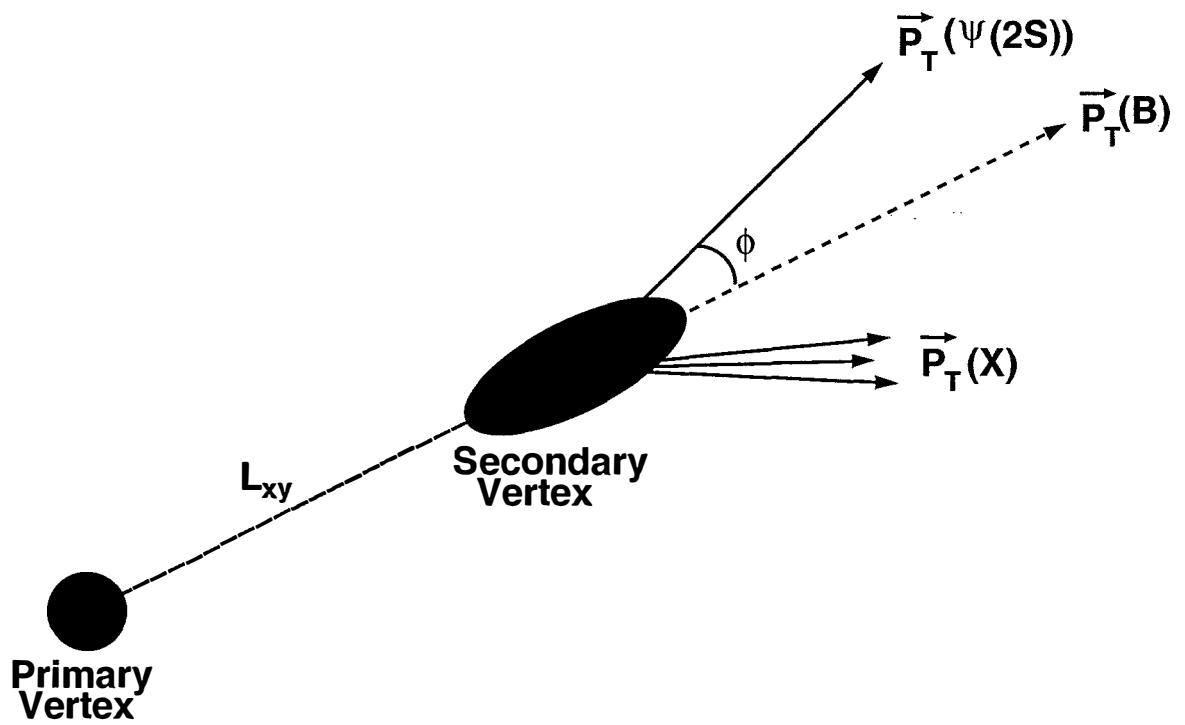
Figure 5-2: A sketch showing the variables used to define the transverse decay length, L_{xy}, in the $x - y$ plane.
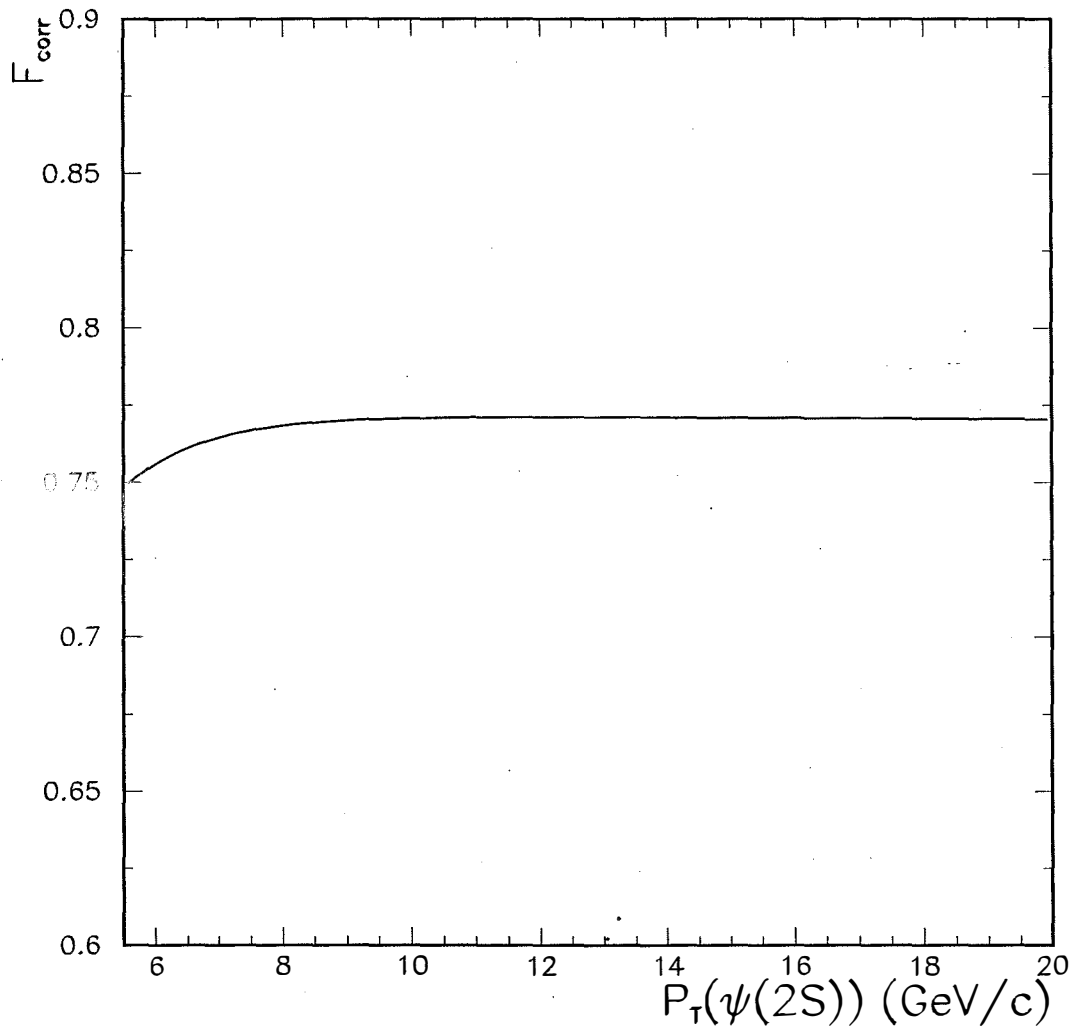
Figure 5-3: The Monte Carlo correction factor F_{corr} as a function of $\psi(2S)$ P_T. F_{corr} relates the proper decay length (ct) calculated with the $\psi(2S)$ quantities to the true ct of the B meson.
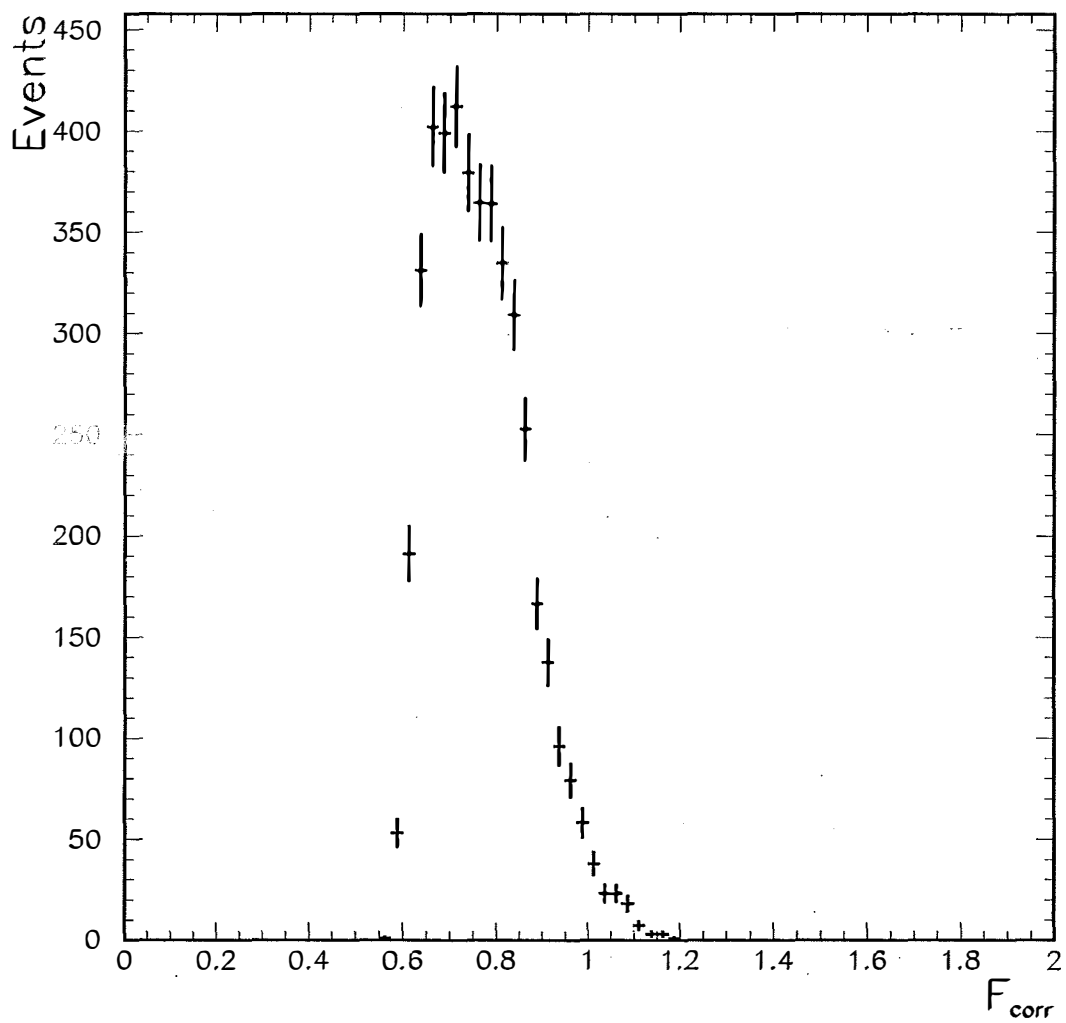
Figure 5-4: F_{corr} distribution for $10 < P_T(\psi(2S)) < 11$ GeV/c. This is an example showing that the variation on the correction factor is not large.

where $G(x; \sigma) = \frac{1}{\sqrt{2\pi}\sigma} e^{-\frac{x^2}{2\sigma^2}}$ and $E(x, \lambda) = \frac{1}{\lambda} e^{-\frac{|x|}{\lambda}}$. The error on measured ct is indicated by σ, and ρ is a factor to scale the measured error such that the error correctly accounts for the measurement uncertainty. The parameters f_+, f_- and f_{sym} are the background fractions in the positive, negative and symmetric exponentials, with λ_+, λ_- and λ_{sym} their corresponding lifetimes.

The functional form for the $\psi(2S)$ signal S_i consists of two terms, one for prompt $\psi(2S)$ and one for $\psi(2S)$ from B decays:

$$S_i = (1 - f_B)R(ct) + f_B \int_0^\infty d\overline{ct} E(\overline{ct}; ct_0) R(ct - \overline{ct}) \tag{5.5}$$

where $R(x) = (1 - f_{tail})G(x; \rho\sigma) + f_{tail}\frac{1}{2}E(x; \lambda_{tail})$ is the resolution function used to describe the ct smearing caused by the detector resolution. The prompt component is parameterized by the resolution function, while the B-decay component is represented by an exponential convoluted with the resolution function. The parameters f_{tail} and λ_{tail} are the fraction and lifetime of the non-Gaussian tails in the resolution function, with f_{tail} fixed to be 2%. The parameter f_B is the B fraction and ct_0 is the average B lifetime. We use a fixed value of $ct_0 = 0.0438$ cm, obtained from the CDF measurement of average B lifetime[68].

In the signal region, the total fitted function T is then given by

$$T = f_S S_i + (1 - f_S)B_k \tag{5.6}$$

where f_S is the purity of the signal region. The range of the signal region is chosen to maximize $S^2/(S + B)$, where S(B) is the number of signal (background) events. It varies from a 60 MeV/c^2 mass window around the $\psi(2S)$ mass at low P_T to a 94 MeV/c^2 mass signal region at high P_T.

The likelihood function used in the fit is defined as:

$$\mathcal{L} = \left(\prod_{i=1}^{N_{SR}} T(ct_i) \right) \cdot \left(\prod_{i=1}^{N_{SB}} B_k(ct_i) \right) \cdot P(N_{SR}; N_{SR}^{fit}) \cdot P(N_{SB}; N_{SB}^{fit}) \tag{5.7}$$

where N_{SR} (N_{SB}) is the number of events in the signal region (sideband region). N_{SR}^{fit} and N_{SB}^{fit} are the fitted numbers of events in the signal and sideband regions respectively. $P(N; \mu)$ is the Poisson probability to observe N events when, on average,

μ events are expected. Both the ct distributions in the signal and sideband regions are fitted simultaneously.

Figure 5-5 shows the result of the fit for events with both muons reconstructed in the SVX. The parameters obtained from the fit are listed in Table 5.1.

	$5.5 < P_T \leq 7$	$7 < P_T \leq 9$	$9 < P_T \leq 20$
f_S	0.604 ± 0.014	0.650 ± 0.017	0.641 ± 0.020
N_{SR}^{fit}	$758. \pm 37.$	$464. \pm 27.$	$448. \pm 28$
f_B	0.206 ± 0.023	0.268 ± 0.031	0.352 ± 0.035
ρ	1.023 ± 0.031	1.008 ± 0.045	1.091 ± 0.046
λ_{tail}	0.050 ± 0.028	0.070 ± 0.044	0.061 ± 0.041
f_+	0.108 ± 0.015	0.176 ± 0.024	0.235 ± 0.030
λ_+	0.065 ± 0.007	0.059 ± 0.006	0.061 ± 0.007
f_-	0.066 ± 0.016	0.063 ± 0.019	0.062 ± 0.022
λ_-	0.047 ± 0.007	0.053 ± 0.011	0.050 ± 0.011
f_{sym}	0.284 ± 0.037	0.307 ± 0.047	0.179 ± 0.047
λ_{sym}	0.013 ± 0.002	0.012 ± 0.002	0.012 ± 0.004

Table 5.1: The parameters obtained from the lifetime fit for the three $\psi(2S)$ P_T bins.

5.4   Prompt Fractions

Fitting the ct distribution enables us to calculate the fractions of pure prompt, B-decay, and background components in a given region of ct. We can subsequently determine the relative purity by taking a ratio of "signal" to "background". For the prompt (B) component, the "signal" is defined as prompt (B) and the "background" is defined as the generic background plus the B (prompt) component. Figure 5-6 shows the relative purity as a function of ct. The prompt component peaks near zero whereas the B-decay component peaks at higher ct. There is a cross-over near $ct = 0.01$ cm. We can now define two ct regions, one from $ct^{bot} = -0.1$ cm to $ct^{cut} = 0.01$
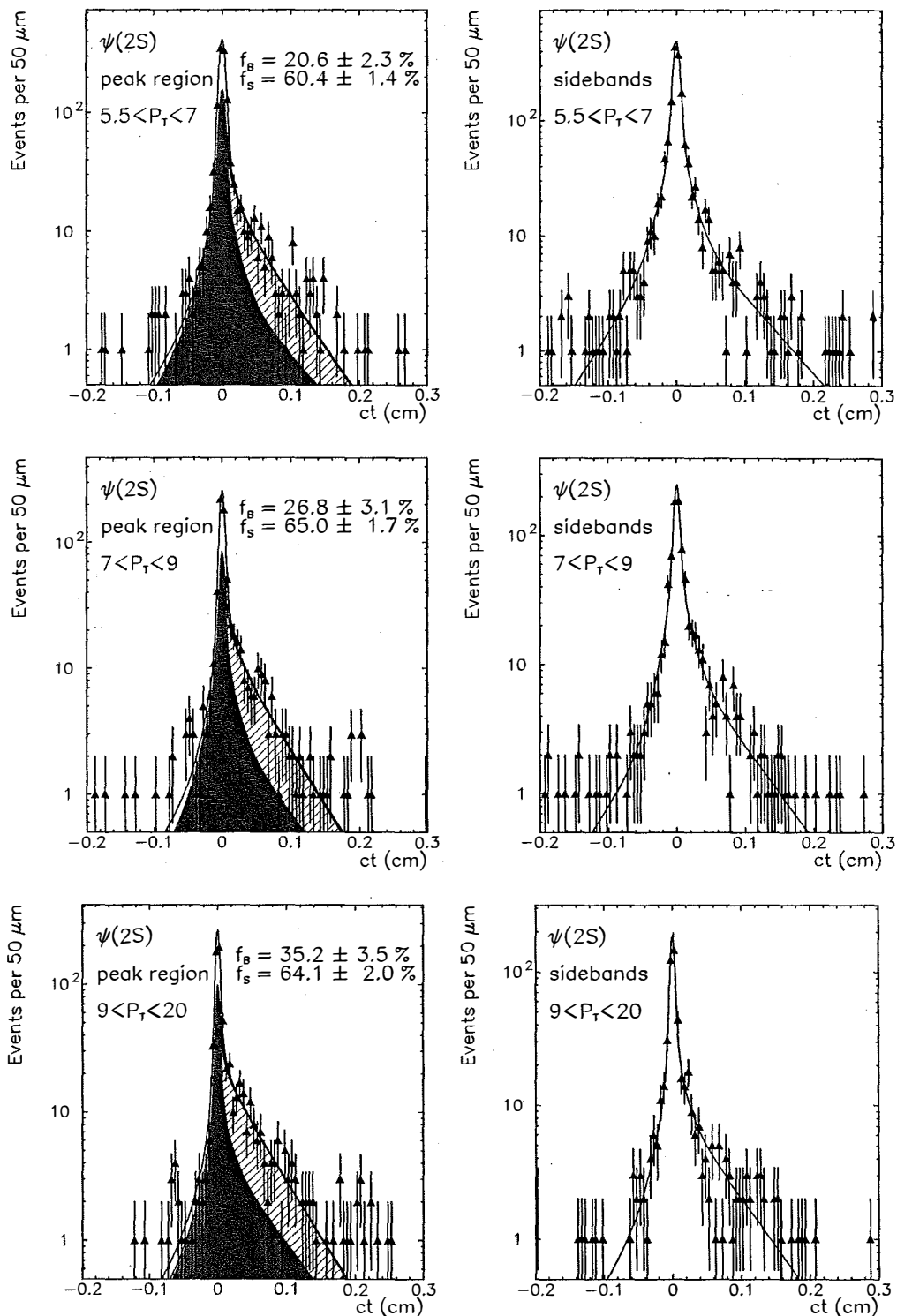
Figure 5-5: $\psi(2S)$ ct distributions overlaid with fit results for the three P_T bins. In the signal region (left plots), the solid region is the background shape (right plots) and the hashed region is the excess of the B-decay component over the background. The solid line represents the total function. The parameter f_B is the B fraction as defined in Equation (5.5) and f_S is the purity of the signal region as defined in Equation (5.6).

cm, and another from $ct^{cut} = 0.01$ cm up to $ct^{top} = 0.3$ cm. The first region is dominated by the prompt component and we call it "low ct" and use the symbol "$-$" to denote it. The second region is dominated by B-decay component and we call it "high ct", and denote it by "$+$". This provides us two optimal samples to fit for polarization.

The prompt fractions in the low and high ct regions can be determined by numerically integrating the parameterizations in the ct fits (Equation 5.5). The prompt fraction in the low ct region, p_-, is given by:

$$p_- = \frac{(1 - f_B)u_1}{(1 - f_B)u_1 + f_B v_1}, \tag{5.8}$$

where the numbers u_1 and v_1 are the integrals of the prompt and B-decay components in the region:

$$u_1 = \int_{ct^{bot}}^{ct^{cut}} R(ct) dct \tag{5.9}$$

$$v_1 = \int_{ct^{bot}}^{ct^{cut}} \int_0^\infty d\overline{ct} E(\overline{ct}; ct_0) R(ct - \overline{ct}) dct. \tag{5.10}$$

The prompt fraction in the high ct region, p_+, is calculated in a similar fashion:

$$p_+ = \frac{(1 - f_B)u_2}{(1 - f_B)u_2 + f_B v_2} \tag{5.11}$$

where u_2 and v_2 are the corresponding integrals in the high ct region:

$$u_2 = \int_{ct^{cut}}^{ct^{top}} R(ct) dct \tag{5.12}$$

$$v_2 = \int_{ct^{cut}}^{ct^{top}} \int_0^\infty d\overline{ct} E(\overline{ct}; ct_0) R(ct - \overline{ct}) dct. \tag{5.13}$$

The values of p_- and p_+ for different $\psi(2S)$ P_T ranges are tabulated in Table 5.2. These fractions indicate a purity of $\approx 90\%$ in each sample. These will be used to account for the prompt and B-decay contributions in the polarization fit which will be discussed in the next chapter.
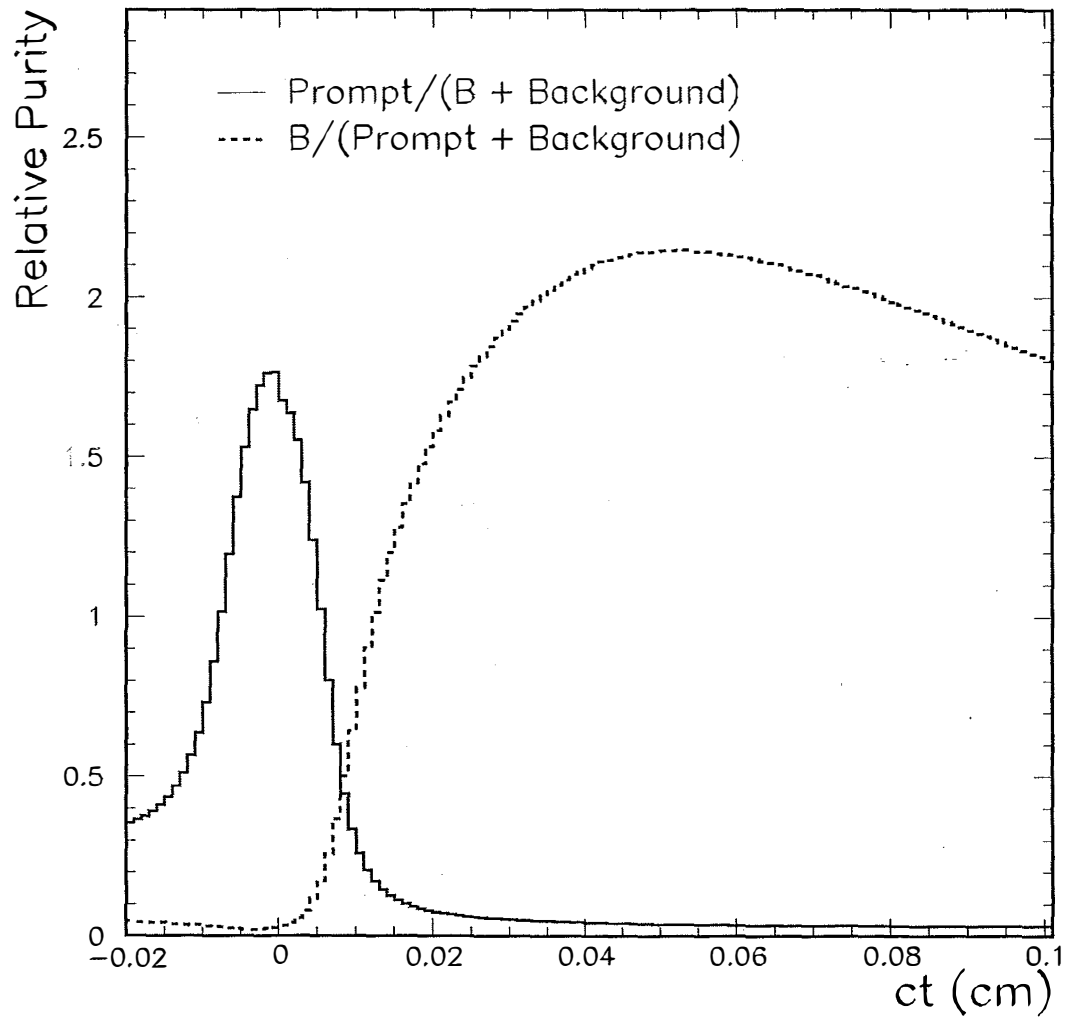
Figure 5-6: Ratio of signal fraction to background fraction for the $\psi(2S)$ mesons from prompt production and B decays as a function of ct.

P_T	p_-	p_+
5.5-7	0.95±0.01	0.14±0.02
7-9	0.93±0.02	0.11±0.02
9-20	0.90±0.02	0.08±0.02

Table 5.2: Prompt fractions in the low and high ct regions for the three $\psi(2S)$ P_T bins.

Chapter 6

Fitting Technique

The polarization of the $\psi(2S)$ meson, based on $\psi(2S) \rightarrow \mu^+\mu^-$ decays, is measured using a helicity basis (Appendix A). The helicity angle θ^* is calculated for the positive muon and the $|\cos\theta^*|$[1] distribution is constructed by fitting the dimuon invariant mass distributions in each $|\cos\theta^*|$ bin to determine the $\psi(2S)$ event yield in that bin. This was described in Chapter 3. The detector acceptance and trigger efficiencies in $|\cos\theta^*|$ are derived using Monte Carlo simulation, as discussed in Chapter 4. In Chapter 5, we showed how the fractions of the prompt and the B-decay components in the $\psi(2S)$ data samples are determined by fitting the proper decay length distribution of the $\psi(2S)$ mesons. With all these ingredients available, we are ready to determine the polarization by fitting the $|\cos\theta^*|$ angular distribution.

In the early stage of the analysis, we investigated a maximum-likelihood fit in order to make the maximal use of the available statistics. However, toy Monte Carlo experiments showed that a χ^2 fitting method gives comparable uncertainty on the fitted value of the polarization to that using the maximum-likelihood fit. This indicates that the loss in information due to the binning in $|\cos\theta^*|$ is negligible. Another advantage of using the χ^2 fitting method is that a modeling of the background events is not required. Therefore, we use the χ^2 fitting method to extract the polarization

---

[1] Because of the limited statistics in the $\psi(2S)$ data sample, we use 10 bins in the absolute value of $\cos\theta^*$. The symmetry of the angular distribution is verified in the J/ψ data which have higher statistics.

from the $|\cos\theta^*|$ angular distribution.

This chapter describes the details of the fitting procedure. The fit results and systematics are discussed in the next chapter.

6.1   The χ^2 Function

The χ^2 function is constructed by comparing the difference between the number of observed $\psi(2S)$ candidates $N_k^{obs}(x_i)$ and the number of events predicted from theory $N_k^{pred}(x_i)$ against the measurement uncertainty $\sigma_k(x_i)$:

$$\chi^2 = \sum_{k=1}^{2} \sum_{i=1}^{L} \frac{(N_k^{obs}(x_i) - N_k^{pred}(x_i))^2}{\sigma_k(x_i)^2},$$ (6.1)

where x_i is the variable representing the center of each $|\cos\theta^*|$ bin. The parameter L stands for the ten $|\cos\theta^*|$ bins used in the analysis, whereas k is the sample index that runs over both the low and high ct samples. Since each sample is not pure, the contributions from the prompt production ($P(x_i)$) and from B decays ($B(x_i)$) are considered in calculating the number of predicted events:

$$N_k^{pred}(x_i) = N_k^{Total}[p_k P(x_i) + (1 - p_k)B(x_i)].$$ (6.2)

The two components are weighted by their relative fractions, where p_k is the prompt fraction in each sample. N_k^{Total} is the total number of the observed signal events and is used to normalize the prediction to the measurement. The probability density functions, $P(x_i)$ and $B(x_i)$, are obtained from the product of the normalized angular distribution $\omega(x; \alpha)$ and the acceptance[2] with proper normalization:

$$P(x_i) = \frac{\omega(x_i; \alpha_P)A_P(x_i)}{\sum_j \omega(x_j; \alpha_P)A_P(x_j)}$$ (6.3)

$$B(x_i) = \frac{\omega(x_i; \alpha_B)A_B(x_i)}{\sum_j \omega(x_j; \alpha_B)A_B(x_j)}.$$ (6.4)

---

[2]We recall that, in this thesis, acceptance refers to the *effective* acceptance that includes the geometric and kinematic acceptance of the detector as well as the reconstruction efficiency.

$A_P(x_i)$ and $A_B(x_i)$ represent the acceptance parameterizations of $\psi(2S)$ meson produced promptly or via B decays respectively, while α_P and α_B denote their polarizations. The two polarizations are the fit parameters. The normalized $\cos\theta^*$ angular distribution is derived in Appendix A as:

$$\omega(x; \alpha) = \frac{3}{2(3+\alpha)}(1 + \alpha x^2).\qquad(6.5)$$

The measurement uncertainty $\sigma_k(x_i)$ in the χ^2 (Equation 6.1) has two sources. The major component is due to the statistical uncertainty on the $\psi(2S)$ event yield from fitting the mass distribution in data. This uncertainty is added in quadrature with a small statistical error in the Monte Carlo acceptance parameterization.

The χ^2 function is minimized using the MINUIT fitting package[69]. A test of this χ^2 fitter with toy Monte Carlo samples is described in Appendix C.

The acceptance parameterizations in Equations (6.3) and (6.4) assume no explicit dependence on the polarizations. However, these parameterizations are found to depend on the polarizations through the input $\psi(2S)$ P_T spectra. This issue is addressed in the next section.

6.2 Iterative Fit

An iterative fitting procedure is implemented to account for the fact that the input $\psi(2S)$ P_T spectra used to generate the acceptances depend on the values of the polarization. This effect may be significant, especially in the measurement for the $9 < P_T \leq 20$ bin, due to its large bin size.

The acceptance in $\cos\theta^*$ can be analytically expressed as:

$$A(\cos\theta^*; \alpha) = \frac{\int \frac{d\sigma}{dP_T}(\alpha)\omega(\cos\theta^*; \alpha)A'(P_T, \cos\theta^*)dP_T}{\int \frac{d\sigma}{dP_T}(\alpha)\omega(\cos\theta^*; \alpha)dP_T}\qquad(6.6)$$

where $\frac{d\sigma}{dP_T}(\alpha)$ is the input P_T spectrum, $\omega(\cos\theta^*; \alpha)$ is the normalized angular distribution, and $A'(P_T, \cos\theta^*)$ is the acceptance in P_T and $\cos\theta^*$, with other kinematic variables integrated out. The angular distributions can be taken out of the integrals and cancel because they are independent of P_T. Thus, the acceptance in $\cos\theta^*$ is

135

independent of the polarization used to generate the angular distribution, but it can still depend on α through $d\sigma/dP_T$:

$$A(\cos\theta^*;\alpha) = \frac{\int \frac{d\sigma}{dP_T}(\alpha)A'(P_T,\cos\theta^*)dP_T}{\int \frac{d\sigma}{dP_T}(\alpha)dP_T}. \tag{6.7}$$

As described in Chapter 4, the input P_T spectrum is determined by calculating the differential cross section from the Run1A data:

$$\frac{d\sigma}{dP_T}(\alpha) = \frac{dN}{dP_T}(\alpha_D)\frac{1}{A(P_T;\alpha)}\frac{1}{\mathcal{B}\cdot\int\mathcal{L}dt} \tag{6.8}$$

where dN/dP_T is the number of $\psi(2S)$ candidates in P_T bins, $A(P_T;\alpha) = \int\omega(\cos\theta^*;\alpha)A'(P_T,\cos\theta^*)d\cos\theta^*$ is essentially the P_T acceptance, $\mathcal{B}$ is the branching fraction for $\psi(2S) \to \mu^+\mu^-$ and $\int\mathcal{L}dt$ is the integrated luminosity. At the time of the Run 1A $d\sigma/dP_T$ measurement, the polarization in the data, α_D, was unknown. Thus a unpolarized P_T acceptance $A(P_T;\alpha=0)$ was used, and the variation in $d\sigma/dP_T$ due to α varying between -1 and 1 was assigned as a systematic uncertainty. Figure 6-1 shows the P_T acceptance for three different values of polarization $\alpha = -1, 0$, and 1. We see that the acceptance for $\alpha = -1$ is larger than that of $\alpha = 0$ throughout the shown $\psi(2S)$ P_T range. But the increase in acceptance is smaller at high P_T than at low P_T, as reflected in the negative slope of the acceptance ratio $A(P_T;\alpha=-1)/A(P_T;\alpha=0)$ shown in the top plot of Figure 6-2. The opposite trend holds for the comparison between the acceptance for $\alpha = 1$ and $\alpha = 0$. The polarization dependence in $d\sigma/dP_T$ is therefore clearly seen.

Substituting equation (6.8) to equation (6.7) and canceling the common terms, we have

$$A(\cos\theta^*;\alpha) = \frac{\int \frac{dN}{dP_T}(\alpha_D)\frac{1}{A(P_T;\alpha)}A'(P_T,\cos\theta^*)dP_T}{\int \frac{dN}{dP_T}(\alpha_D)\frac{1}{A(P_T;\alpha)}dP_T}. \tag{6.9}$$

The integral in the denominator gives a normalization constant, C, which does not affect the shape of the $\cos\theta^*$ acceptance. Thus,

$$A(\cos\theta^*;\alpha) = \frac{1}{C}\int \frac{dN}{dP_T}(\alpha_D)\frac{1}{A(P_T;\alpha)}A'(P_T,\cos\theta^*)dP_T. \tag{6.10}$$

This indicates that the polarization used to generate the P_T acceptance will affect the $\cos\theta^*$ acceptance. As stated earlier, the input P_T spectrum was determined from

136
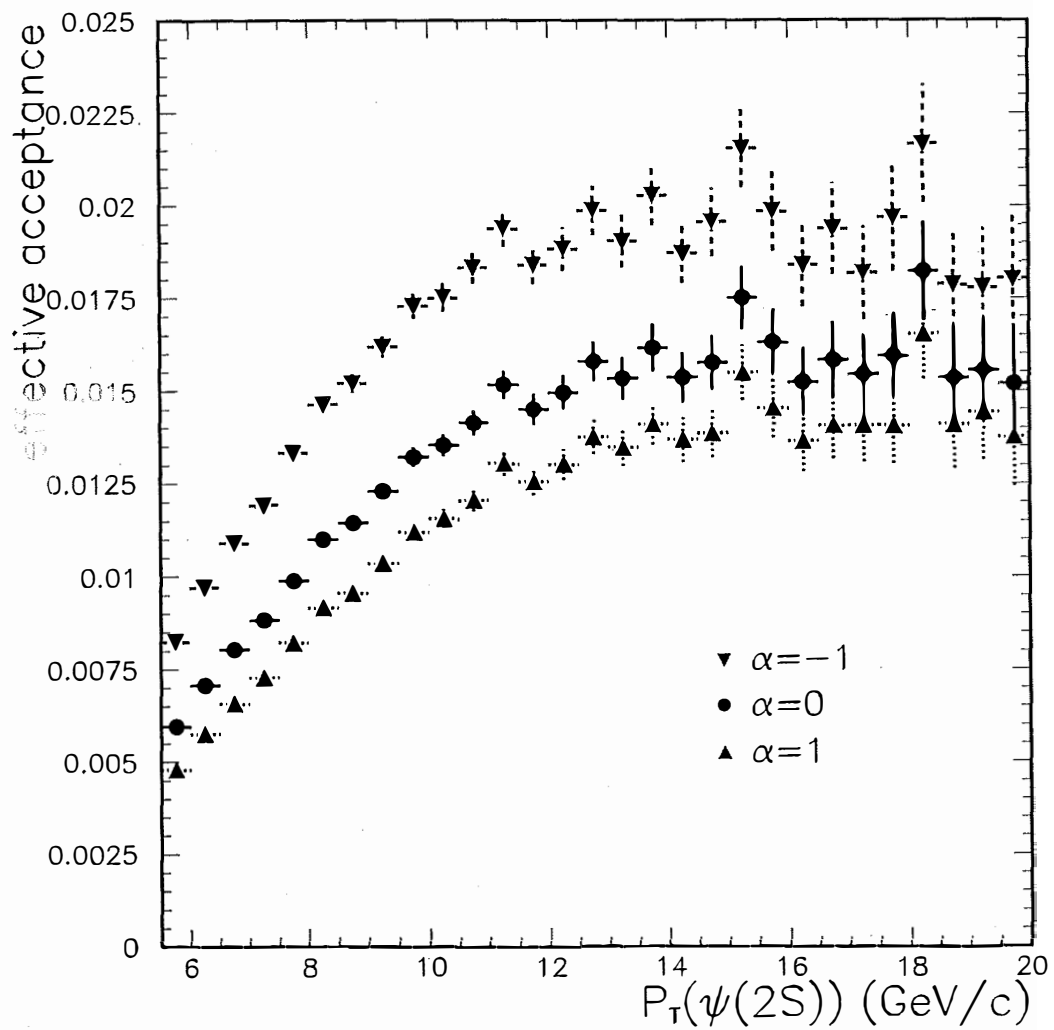
Figure 6-1: The $\psi(2S)$ P_T acceptance for three different polarizations.
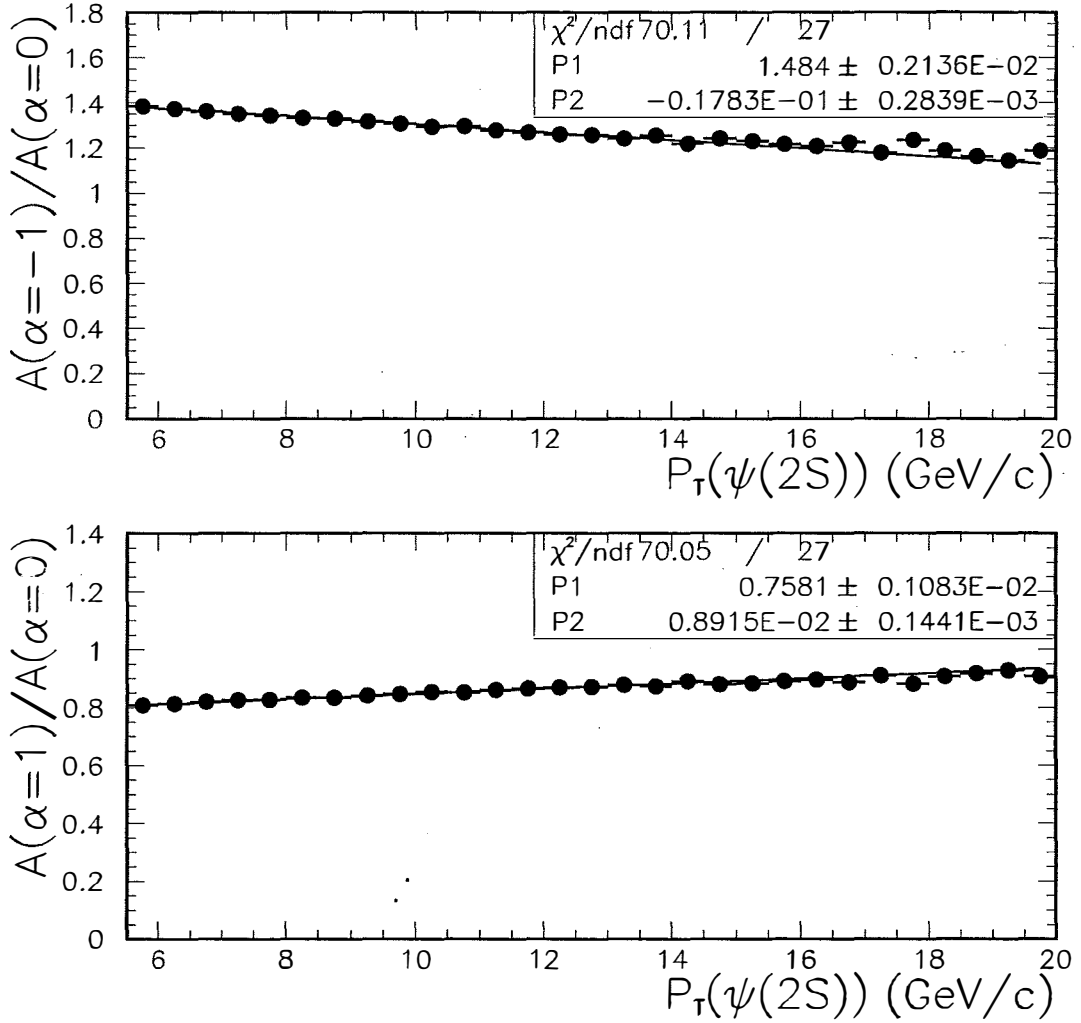
Figure 6-2: $\psi(2S)$ P_T acceptance ratio for $A(P_T; \alpha = -1)/A(P_T; \alpha = 0)$ (top) and $A(P_T; \alpha = 1)/A(P_T; \alpha = 0)$ (bottom). Each distribution is fitted with a linear parameterization: $P1 + P2 \cdot P_T$.

Run1A data with a unpolarized P_T acceptance $A(P_T; \alpha = 0)$. Therefore, in order to extract the true polarization α_D in the data, we need to use the fitted polarization to correct the input P_T spectrum and the corresponding $\cos\theta^*$ acceptance, and then redo the fit. This process should be iterated until the fitted polarization converges to α_D.

We point out that another way to determine α_D is by fitting the P_T and $\cos\theta^*$ distributions simultaneously. Nevertheless, due to the limited event yield of the $\psi(2S)$ sample used for this analysis, we do not have sufficient statistics for a reasonable binning of the events in both P_T and $\cos\theta^*$. Therefore, we opt for the iterative method.

To find what weight should be used in the correction, we rewrite Equation(6.10) as:

$$A(\cos\theta^*; \alpha) = \frac{1}{C} \int \frac{dN}{dP_T}(\alpha_D) \frac{1}{A(P_T; \alpha = 0)} \frac{A(P_T; \alpha = 0)}{A(P_T; \alpha)} A'(P_T, \cos\theta^*) dP_T. \quad (6.11)$$

This suggests that, by applying a weight, $r = A(P_T; \alpha = 0)/A(P_T; \alpha)$, to each event in the Monte Carlo sample that is generated with $A(P_T; \alpha = 0)$, we can obtain the $\cos\theta^*$ acceptance for arbitrary α. Thus we do not need to generate multiple Monte Carlo samples, one for each value of α. This saves time and also avoids statistical fluctuations from smearing out the effect we try to correct for.

To determine the weight r, we realize that $A(P_T; \alpha) = \int \omega(\cos\theta^*; \alpha) A'(P_T, \cos\theta^*) d\cos\theta^*$, which can be calculated by summing the events passing the acceptance:

$$A(P_T; \alpha) = \frac{2}{N} \sum_{i=1}^{N} \omega(\cos\theta_i^*; \alpha), \qquad (6.12)$$

where N is the number of Monte Carlo events that pass the acceptance. The factor of 2 is introduced to account for the physical range of integrating $\cos\theta^*$ from -1 to 1. The resulting sum has an implicit dependence on $\psi(2S)$ P_T. Therefore, the ratio of P_T acceptances of an arbitrary α to that of $\alpha = 0$ can be expressed as:

$$\frac{1}{r} = \frac{\sum_{i=1}^{N} \omega(\cos\theta_i^*; \alpha)}{\sum_{i=1}^{N} \omega(\cos\theta_i^*; \alpha = 0)}. \qquad (6.13)$$

Substituting $\omega(\cos\theta^*; \alpha)$ into Equation (6.13) and with some algebraic simplifications,

we obtain:

$$\frac{1}{r} = \frac{3}{3+\alpha}(1 + \frac{\alpha}{N}\sum_{i=1}^{N}\cos^2\theta_i^*). \tag{6.14}$$

Notice that the summation in Equation (6.14) depends on $\psi(2S)$ P_T implicitly. We plot the ratios of P_T acceptances for various values of α (from -1 to 1 with a step size of 0.1) to that of $\alpha = 0$ and find that they can be well parameterized with linear fits. The two extreme cases for $\alpha = -1$ and 1 are shown in Figure 6-2. This implies the sum in Equation (6.14) has a linear dependence on P_T and can be expressed in the following functional form:

$$\frac{1}{r} = \frac{3}{3+\alpha}(1 + \alpha(mP_T + c)), \tag{6.15}$$

where m and c are the slope and the intercept of the linear parameterization. From the linear fit for $\alpha = -1$ in the top plot of Figure 6-2, we have

$$\frac{1}{r} = 1.484 - 0.018P_T. \tag{6.16}$$

Comparing the coefficients of the linear term in P_T and the constant term in Equation (6.15) and Equation (6.16), we obtain

$$\begin{cases} m = 0.0119 \pm 0.0002 \\ c = 0.0107 \pm 0.0014. \end{cases}$$

The errors of the parameters are small and will have negligible effects on the iterative fit results.

Thus, the ratio of P_T acceptance can be expressed as follows:

$$\frac{1}{r} = \frac{3}{3+\alpha}((1 + 0.0107\alpha) + 0.0119\alpha P_T). \tag{6.17}$$

Setting $\alpha = 1$, we have

$$\frac{1}{r} = 0.758 + 0.009P_T, \tag{6.18}$$

which is consistent with the fitted values of a linear parameterization to $A(P_T; \alpha = 1)/A(P_T; \alpha = 0)$, as shown in the bottom plot of Figure 6-2. The validity of Equation (6.17) is further verified by checking empirically that it holds for other values of α between -1 and 1.

140

Therefore, once we have a fitted value of α, we can determine the weight to correct the unpolarized Monte Carlo from:

$$r(P_T; \alpha) = \frac{3 + \alpha}{3} \frac{1}{(1 + 0.0107\alpha) + 0.0119\alpha P_T}, \qquad (6.19)$$

where P_T is the $\psi(2S)$ P_T for each event. The reweighting process is carried out on the fly inside the fitter. Subsequently, it outputs a new fitted value of α, which is in turn input to the fitter for iteration. The iteration continues until the output value α^{out} is equal to the input value α^{in}.

The fit results of the prompt and B-decay $\psi(2S)$ polarizations are presented in the next chapter.

Chapter 7

Measurement of the $\psi(2S)$ Polarization

7.1 Results

Having described the fitting technique in the preceding chapter, we now present the results of fitting the $\psi(2S)$ polarizations for prompt production and B decays. This is followed by a discussion of the systematic uncertainties on the results. We will then conclude and discuss the implications of our measurement. An outlook on future prospects of measuring quarkonium polarizations at the Tevatron ends the chapter.

7.1 Results

Using the χ^2 fitter described in Section 6.1, the data $\cos\theta^*$ distributions in the two ct regions are fitted simultaneously to extract the prompt polarization (α_P) and the B-decay polarization (α_B) for $\psi(2S)$ mesons. The fitting process is iterated until the extracted polarizations converge. Tables 7.1, 7.2 and 7.3 show the convergence of the iterative fits for α_P and α_B in the three $\psi(2S)$ P_T bins. As described in Section 6.2, α^{in} is the input polarization used to calculate the $\cos\theta^*$ acceptance, whereas α^{out} is the fitted polarization in each iteration. The first iteration uses $\alpha^{in} = 0$ in the acceptance calculation.

The iterative fitting procedure is seen to converge quickly – less than five iterations for each P_T bin. In general, the shifts in the fitted α's between the first and the last

iteration	α_P^{in}	α_P^{out}	α_B^{in}	α_B^{out}
1	0.0	-0.0790	0.0	-0.2566
2	-0.0790	-0.0792	-0.2566	-0.2580
3	-0.0792	-0.0792	-0.2580	-0.2580

Table 7.1: Convergence of iterative fits for the $\psi(2S)$ polarizations from prompt production and B decays in $5.5 < P_T \leq 7$ GeV/c.

iteration	α_P^{in}	α_P^{out}	α_B^{in}	α_B^{out}
1	0.0	0.4983	0.0	-1.6809
2	0.4983	0.5003	-1.6809	-1.6844
3	0.5003	0.5002	-1.6844	-1.6844
4	0.5002	0.5002	-1.6844	-1.6844

Table 7.2: Convergence of iterative fits for the $\psi(2S)$ polarizations from prompt production and B decays in $7 < P_T \leq 9$ GeV/c.

iterations are small. The shifts in the last P_T bin are slightly larger than those in the first two P_T bins, as expected from the larger bin size in the $9 < P_T \leq 20$ GeV/c range. The overall small shifts for all three P_T bins indicate that P_T and $\cos\theta^*$ are only weakly correlated.

The final results of polarization fits for the three different P_T bins are summarized in Table 7.4. To make sure the fits converge properly, the χ^2 function in all cases are checked to have the correct parabolic behavior in the polarization parameter spaces. The statistical uncertainties on the fitted polarizations are provided by the MINUIT fitting package[69] as the change in the polarization values required to changes the χ^2 function values by 1. The α_B in the second P_T bin of $\psi(2S)$ lies outside the physically allowed range $-1 \leq \alpha \leq 1$. Since we do not limit the fitted value of α to be within this range, the value of the α_B is consistent with a downward fluctuation of one standard deviation. The correlation coefficients for the fits vary between -0.1 and -0.2, indicating small correlation between α_P and α_B. This is attributed to the

143

iteration	α_P^{in}	α_P^{out}	α_B^{in}	α_B^{out}
1	0.0	-0.5299	0.0	0.2605
2	-0.5299	-0.5418	0.2605	0.2663
3	-0.5418	-0.5421	0.2663	0.2664
4	-0.5421	-0.5421	0.2664	0.2664

Table 7.3: Convergence of iterative fits for the $\psi(2S)$ polarizations from prompt production and B decays in $9 < P_T \leq 20$ GeV/c.

high purity in each ct sample. The χ^2 per degree of freedom, also shown in Table 7.4, is reasonable for all the fits.

P_T (GeV/c)	α_P	α_B	χ^2/dof
5.5-7	-0.08±0.63	-0.26±1.26	0.99
7-9	0.50±0.76	-1.68±0.55	0.61
9-20	-0.54±0.48	0.27±0.81	0.73

Table 7.4: $\psi(2S)$ polarization for prompt and B-decay production in the three $\psi(2S)$ P_T bins.

Figure 7-1 displays the measured $\psi(2S)$ $|\cos\theta^*|$ distributions for the three P_T bins in the low ct region with their polarization fits overlaid. The fits agree well with the distribution of events in the data. The corresponding fits for the high ct region are shown in Figure 7-2. Here the agreement between the data distributions and the fits are not as good, because of more scattering in data points due to the lower statistics in the high ct samples.

As described in Chapter 1, the main parameter of interest in this analysis is the polarization for prompt $\psi(2S)$ mesons. The implication of our α_P measurement in testing the predictions from the NRQCD formalism will be discussed in Section 7.3.
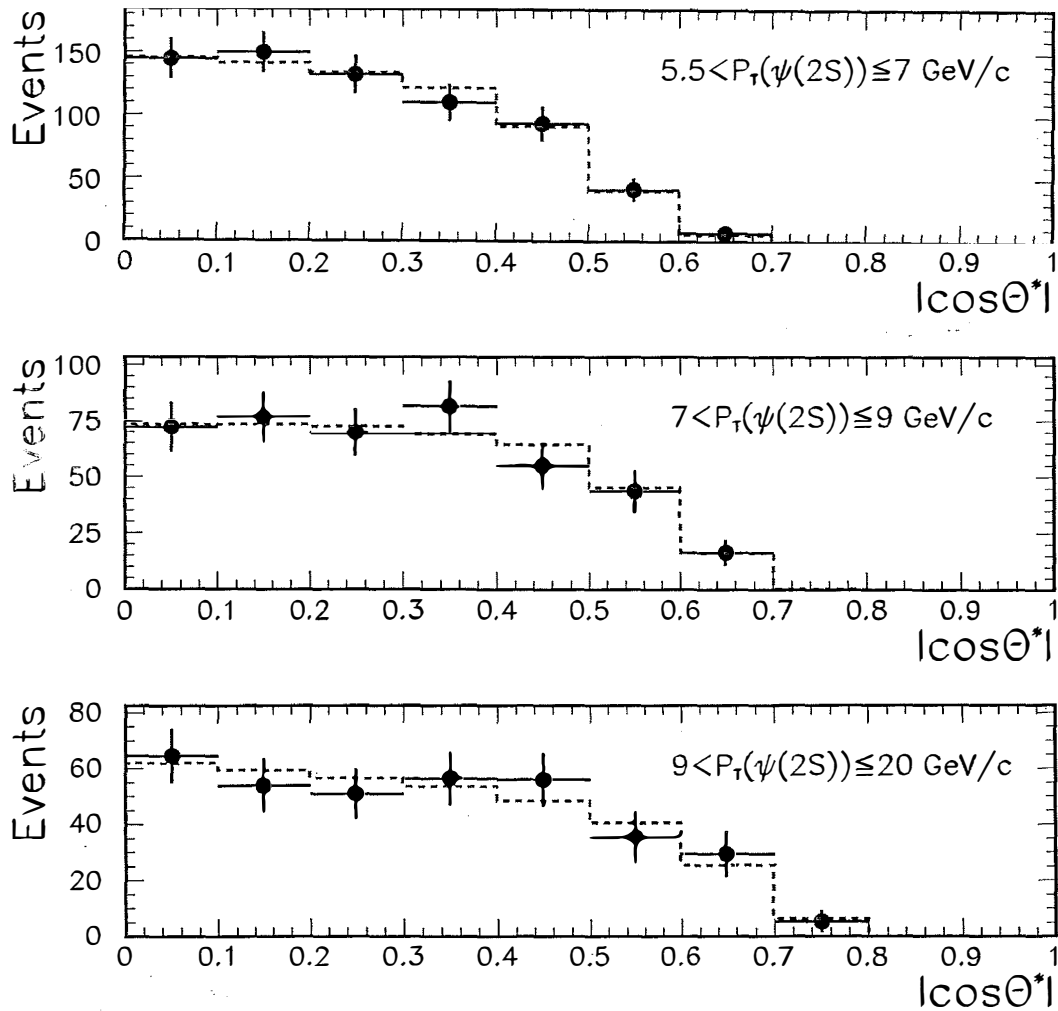
Figure 7-1: The $\psi(2S)$ $|\cos\theta^*|$ distributions in the *low ct* region with their polarization fits (dashed line) overlaid for the three P_T ranges.
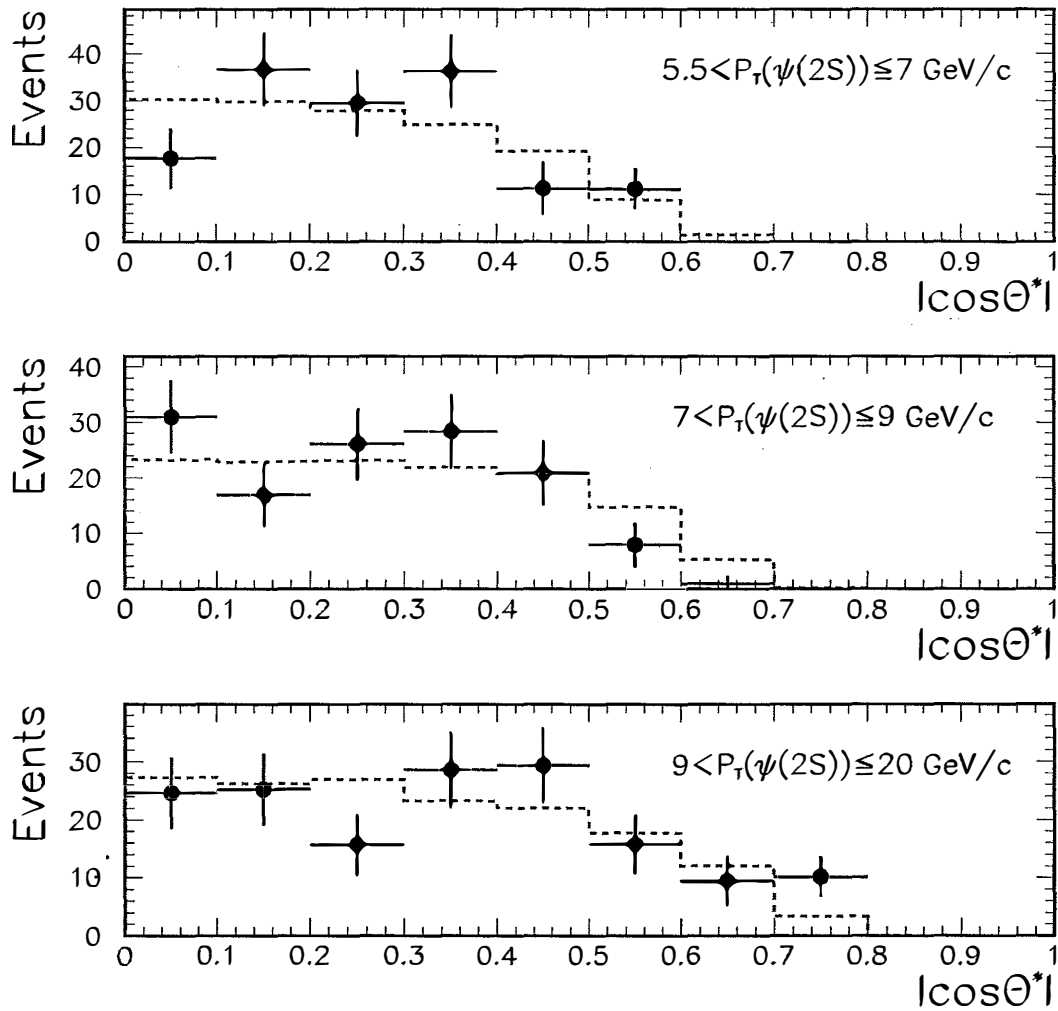
Figure 7-2: The $\psi(2S)$ $|\cos\theta^*|$ distributions in the *high ct* region with their polarization fits (dashed line) overlaid for the three P_T ranges.

7.2 Systematics

We study three categories of systematic uncertainties on the polarization measurement. One is the event yield uncertainty resulting from the mass fits in the $\cos\theta^*$ bins. Another is the uncertainty on the $\cos\theta^*$ acceptance due to the tuning of the Monte Carlo P_T distribution. The last one is the uncertainty on the fraction of prompt $\psi(2S)$ from the determination of f_B in the ct fits. They are discussed in the following sections.

We do not include the systematic uncertainty due to the parameterization of the trigger efficiencies. This effect is found to be significant only for low transverse momenta of the $\psi(2S)$ meson. For $P_T(\psi(2S)) > 5.5$ GeV/c, as is the case in this analysis, the uncertainty on the polarization due to the trigger efficiency is negligible.

7.2.1 Mass Fit

To study the systematics arising from the fit of the data mass distributions, the mass widths are fixed to their $\pm 1\sigma$ values and the fits are redone. The resulting event yields are used to fit for the polarization. The observed shifts in the α's are then used as an estimate of the systematic errors.

As discussed in Section 3.5, in the $9 < P_T(\psi(2S)) \leq 20$ GeV/c bin, the mass width also depends on $|\cos\theta^*|$. Monte Carlo scaling factors were used to account for the dependence. To evaluate the systematic uncertainty due to these scaling factors, the points in the plot of mass width dependence (see Figure 3-2) are varied by $\pm 1\sigma$ and the scaling factors are recalculated. This variation results in negligible changes in the event yields and subsequently the polarizations.

7.2.2 Monte Carlo P_T Tuning

As described in Section 4.5, the $\psi(2S)$ P_T distributions of the Monte Carlo samples were tuned so that they would be in agreement with those in the data. This was necessary because the P_T spectrum from the differential cross section measurement extends only up to 17 GeV/c. The Monte Carlo P_T distribution was first parameter-

ized by an exponential $e^{-\frac{P_T}{b}}$, where the parameter b controls the slope of the fall-off. High P_T events were then thrown away to tune the distribution to follow $e^{-\frac{P_T}{b'}}$, where $b' = b + \delta b$. To assess the uncertainty associated with this tuning method, the parameter δb is varied by $\pm 1\sigma$. The resulting $\cos\theta^*$ acceptances are used to fit for the polarizations. Changes in the polarizations from their central values are taken as systematic errors.

7.2.3   B Fraction

The B fractions from the ct fits (see Chapter 5) are varied by $\pm 1\sigma$ and the corresponding changes in the prompt fractions p_- and p_+ are determined. The new values are used in the polarization fits. Shifts in α_P and α_B are used as systematic uncertainty.

7.2.4   Total Systematic Uncertainty

The three sources of systematic uncertainties are added in quadrature to form the total systematic uncertainty. Table 7.5 gives a summary of the systematic uncertainties. Overall, the systematic uncertainties are much smaller than the statistical uncertainties.

	$5.5 < P_T \leq 7$		$7 < P_T \leq 9$		$9 < P_T \leq 20$	
Source	$\Delta\alpha_P$	$\Delta\alpha_B$	$\Delta\alpha_P$	$\Delta\alpha_B$	$\Delta\alpha_P$	$\Delta\alpha_B$
mass width	0.02	0.04	0.01	0.12	0.00	0.03
P_T tuning	0.01	0.02	0.02	0.01	0.04	0.05
f_B	0.00	0.00	0.03	0.03	0.01	0.01
Total	0.02	0.04	0.04	0.12	0.04	0.06

Table 7.5: Systematic uncertainties in the $\psi(2S)$ polarization measurement. The unit of P_T is GeV/c.

7.3 Conclusions and Discussions

Using the decay mode $\psi(2S) \to \mu^+ \mu^-$, we have measured the $\psi(2S)$ polarization in $p\bar{p}$ collisions at the center of mass energy of $\sqrt{s} = 1.8$ TeV. This is a first measurement of the polarization of a quarkonium state at a hadron collider. The $\psi(2S)$ polarization from prompt production and B decays for the three P_T bins are summarized in Table 7.6.

P_T (GeV/c)	α_P	α_B
5.5-7	$-0.08 \pm 0.63 \pm 0.02$	$-0.26 \pm 1.26 \pm 0.04$
7-9	$0.50 \pm 0.76 \pm 0.04$	$-1.68 \pm 0.55 \pm 0.12$
9-20	$-0.54 \pm 0.48 \pm 0.04$	$0.27 \pm 0.81 \pm 0.06$

Table 7.6: The $\psi(2S)$ polarization for prompt and B-decay production in the three $\psi(2S)$ P_T bins. The first error is statistical and the second error is systematic.

In Figure 7-3, the prompt $\psi(2S)$ polarization is plotted versus P_T. Also shown are the theoretical predictions from NRQCD calculations[21, 44]. The measurement has large statistical uncertainties. But it appears to not support the NRQCD predication that the $\psi(2S)$ is transversely polarized at high P_T. Figure 7-4 shows the $\psi(2S)$ polarization from B decays versus P_T.

Recently, CDF[70, 71] has also performed the polarization measurement for J/ψ mesons from prompt production and B decays. The top plot in Figure 7-5 shows the measured values of prompt polarization versus P_T. Since prompt J/ψ can come from decays of the higher charmonium states χ_{c1}, χ_{c2}, and $\psi(2S)$, the measured polarization contains contributions due to these feed-downs. The band is the corresponding theorectical predications from the NRQCD factorization formalism[44]. Again, the predicted transverse polarization at high P_T is not seen in the measurement. The bottom plot in Figure 7-5 shows the measured J/ψ polarization from B decays versus P_T. The measurement is consistent with the NRQCD predications[45] that the polarization lies in the range -0.33 to 0.05.

149
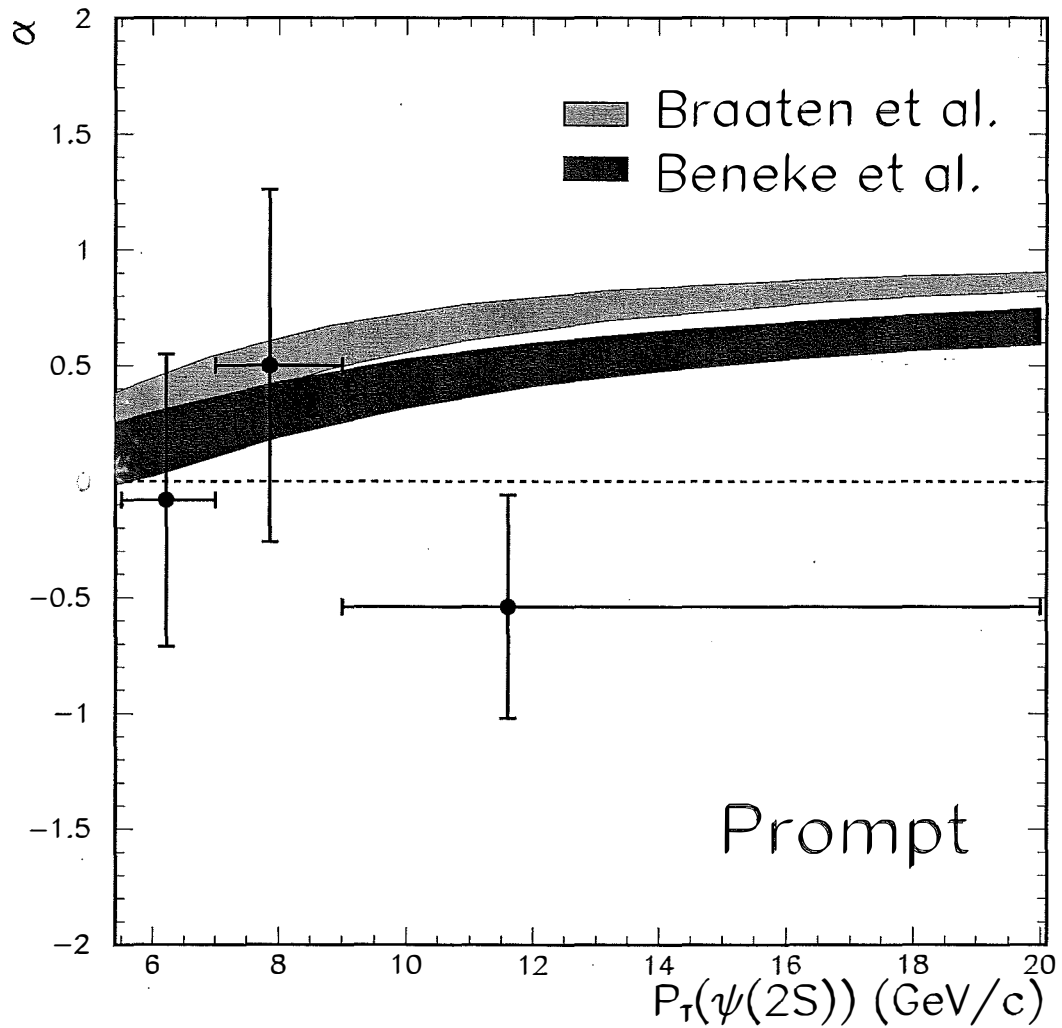
Figure 7-3: The fitted polarization of $\psi(2S)$ mesons from prompt production in three P_T bins. Error bars denote statistical and systematic uncertainties added in quadrature. The bands are NRQCD factorization predications[21, 44].
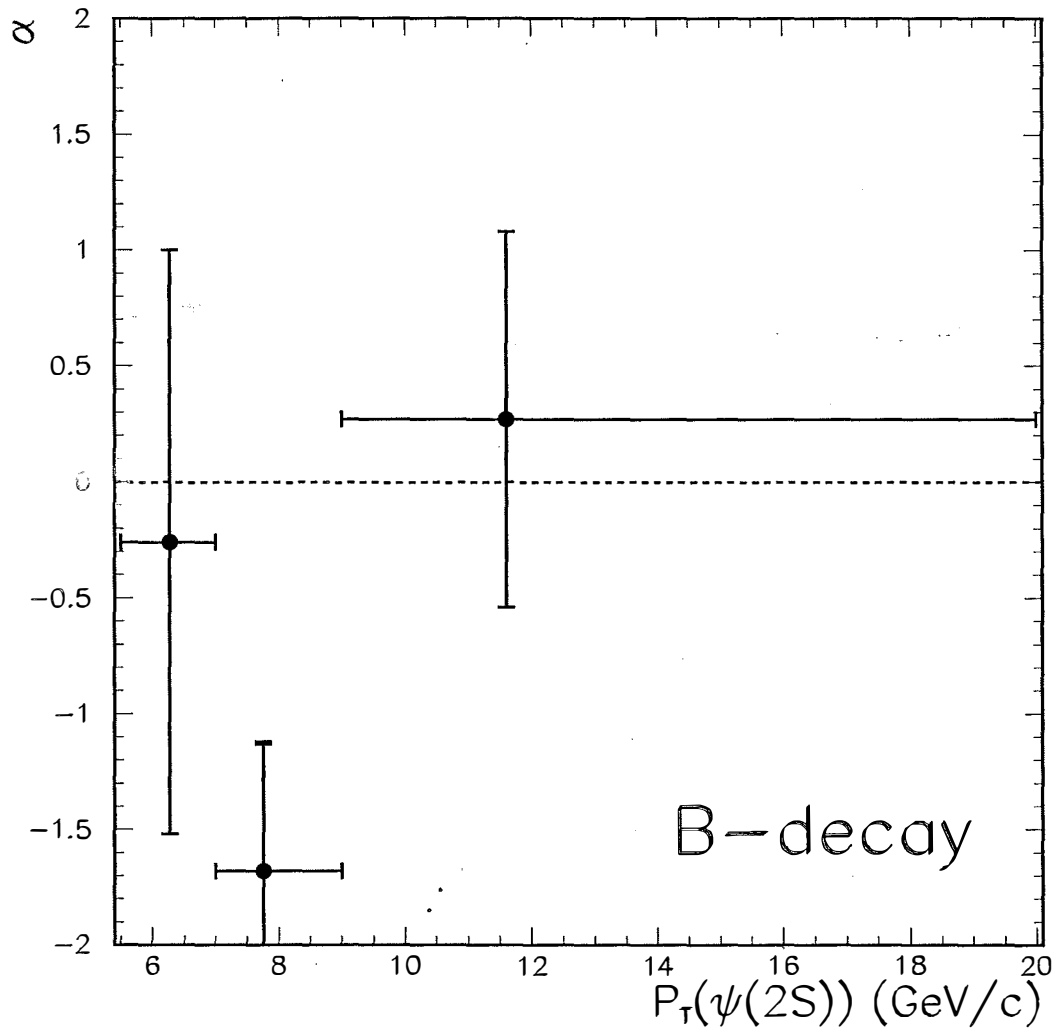
Figure 7-4: The fitted polarization of $\psi(2S)$ mesons from B decays in three P_T bins. Error bars denote statistical and systematic uncertainties added in quadrature.
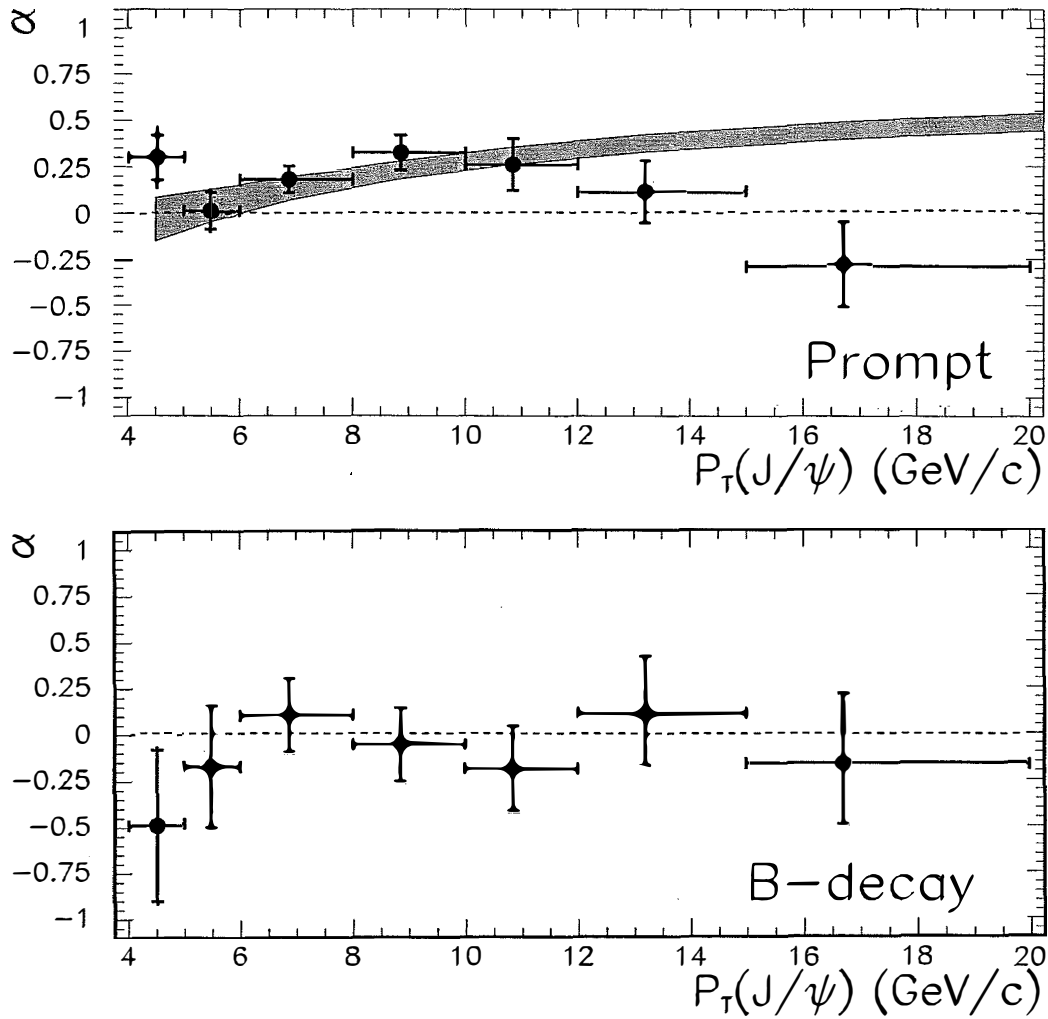
Figure 7-5: The fitted polarizations of J/ψ mesons from prompt production and B decays. The ticks on the vertical error bars denote the statistical uncertainty alone; the full vertical error bars include the systematic uncertainty added in quadrature. The band shows an NRQCD predication[44] which takes the feed-down from higher charmonium states into account.

The CDF measurements of charmonium polarization are limited by statistics, especially for the $\psi(2S)$. However, the appearance of no significant prompt polarization at high P_T is rather puzzling. There is no obvious way to depolarize the $\psi(2S)$ at high P_T. As discussed in Section 1.3.1, depolarization effects due to QCD radiation and the non-fragmentation processes have been considered and estimated to be small[21]. In the case of J/ψ, the polarization contributions from higher charmonium states feed-downs have been taken into account and the resulting predications[44] still show a rising transverse polarization at high P_T. In principle, NRQCD predictions presuppose QCD, factorization, spin symmetry, and the convergence of the α_s and v^2 expansion. Failure of the NRQCD predictions would indicate one of these four assumptions is failing.

There are suggestions[44, 72] that the factorization approach may not be applicable in the charmonium production. This is possible in that the charm quark mass scale, which characterizes the energy scale of the perturbative regime in the production mechanism, is not large enough to be separated from the lower energy scales of the non-perturbative hadronization regime. Subsequently, these two regimes of the charmonium production mechanism may not really be factorized. Another possibility is that the spin symmetry is badly violated. This could happen if the emitted gluons during the hadronization of the $c\bar{c}$ pair are not sufficiently soft. As a result, the transverse polarization of the $c\bar{c}$ pair would not necessarily be conserved as the pair hadronizes to become a charmonium state. To date, the complete QCD higher order corrections are not available. These corrections, being spin-symmetry breaking, could change the scenario significantly.

These issues remain to be resolved and they present a challenge to our understanding of charmonium production in the NRQCD factorization framework.

7.4   Outlook

Charmonium polarization will remain an interesting component in the study of quarkonium production mechanisms. The apparent disagreement between the CDF data and

the NRQCD predictions on prompt charmonium polarization at high transverse momentum has brought in new excitement to the field. At the same time, it means more work needs to be done, both experimentally and theoretically.

Our measurements are based on the Run I data with an integrated luminosity of 110 pb^{-1}. The Tevatron is scheduled to start taking data again in 2001 (Run II). It will provide an expected 20 times increase in integrated luminosity, or 2 fb^{-1} in the first two years. The CDF detector is currently being upgraded[73] for the new run. The increased acceptance of the SVX detector and the lower P_T threshold of the dimuon trigger will more than double the event yield, compared with that of Run I. CDF also intends to record events with two electrons with thresholds similar to the dimuon trigger. The upgraded CMX detector will extend its azimuthal acceptance. The combined increase in integrated luminosity and detector acceptance will result in effectively $\approx$ 50 times more statistics in Run II. This is equivalent to a projected factor of $\approx$ 7 reduction in statistical uncertainties on the measured polarizations. The reduction is important since the current polarization measurements are statistically limited, especially in the $\psi(2S)$. Higher statistics also allows the polarization measurements to be extended to higher P_T regime. This is particularly useful in the upsilon system[74] in order to see the expected transverse polarization. Higher statistics and more precisely measured polarizations of charmonium states will improve the cross section measurements as well. This in turn will allow more accurate extraction of the NRQCD matrix elements, thus facilitating the test of their universality across different experiments.

The D0 detector is also being upgraded[75]. The installation of a solenoid will significantly improve the momentum resolution of muon tracks, while the installation of a silicon vertex detector will allow the separation of the prompt and B-decay components of charmonia. Therefore D0 can provide important confirmation of the charmonium polarization results obtained in CDF.

In addition to hadronic colliders, charmonium polarization measurements have also been suggested in LEP[76], CLEO[77], and at HERA for photo-production[78] as well as lepto-production[79].

Quarkonium physics will remain an exciting area for the years to come. In particular, polarization will continue to be a useful tool in testing our understanding of the quarkonium production mechanisms. Future experiments and theoretical work provide promising prospects of unfolding the mystery behind quarkonium production.

Appendix A

Spin Formalism

A comprehensive review of spin formalisms can be found in reference [80]. The production and decay of the ψ meson is analyzed using the helicity basis. Figure A-1 shows the helicity basis frame in which the z axis is defined as along the ψ direction in the overall center of mass (Lab frame) and the y axis is the production plane normal.
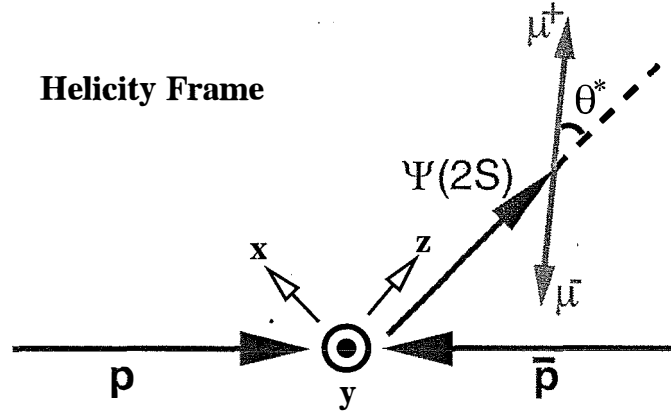
Figure A-1: Sketch showing the coordinate system in the helicity frame.

The normalized angular distribution for the process $\psi \to \mu^+ \mu^-$ is given by

$$I(\Omega) = \left(\frac{2J+1}{4\pi} \right) \sum_{mm'} \rho^J_{mm'} \sum_\lambda \mathbf{D}^{J*}_{m\lambda}(\phi^*, \theta^*, 0) \mathbf{D}^J_{m'\lambda}(\phi^*, \theta^*, 0) \mathbf{g}^J_\lambda \qquad (A.1)$$

where $\Omega = (\theta^*, \phi^*)$ describes the direction of the μ^+ in the ψ rest frame with respect to the direction of ψ in the Lab frame. $\rho^J_{mm'}$ is the production density matrix for a ψ with spin J and m and m' are the magnetic quantum numbers. $\mathbf{D}^J_{m'\lambda}(\phi^*, \theta^*, 0)$ is

the rotation matrix and $\mathbf{g}_\lambda^J$ is the decay amplitude. $\lambda = \lambda_{\mu^+} - \lambda_{\mu^-}$, where λ_μ 's are the helicities of the two muons.

There are various constraints on the density matrix $\rho_{mm'}^J$ which serve to reduce the number of parameters. Hermiticity requires

$$\rho^J = \rho^{J*}. \tag{A.2}$$

Parity conservation gives the following relation

$$\rho_{mm'}^J = (-1)^{m-m'} \rho_{-m-m'}^J. \tag{A.3}$$

We also have the trace condition:

$$\sum_{m=m'} \rho_{mm'}^J = 1. \tag{A.4}$$

The spin of the decaying particle ψ is $J = 1$, which means $\rho_{mm'}$ is a 3×3 matrix. The above conditions imply that $\rho_{11}^1 = \rho_{-1-1}^1 = \frac{1}{2}(1 - \rho_{00}^1)$. The matrix is therefore characterized by two real elements $(\rho_{00}, \rho_{1,-1})$ and one complex element (ρ_{10}).

The decay amplitudes $\mathbf{g}_\lambda^J$ are also constrained by the trace condition:

$$\sum_\lambda \mathbf{g}_\lambda^J = 1. \tag{A.5}$$

A further simplification is possible by assuming μ^+ is 100% right handed with helicity $\lambda_{\mu^+} = +\frac{1}{2}$ and that the μ^- is 100% left handed with helicity $\lambda_{\mu^-} = -\frac{1}{2}$. This is valid because the muons in the rest frame of the ψ are relativistic. Hence $\lambda = 1$ and there is only a single ψ decay amplitude g_1^1. The trace condition implies $g_1^1 = 1$.

Using the above constraints and substituting the corresponding $\mathbf{D}$ functions into equation (A.1), we have

$$I(\Omega) = \left(\frac{3}{4\pi}\right) \left[\frac{1}{4}(1 + \cos^2 \theta^*) + \frac{\rho_{00}}{4}(1 - 3\cos^2 \theta^*) + \frac{\rho_{1-1}}{2} \sin^2 \theta^* \cos 2\phi^* + \frac{\text{Re}\{\rho_{10}\}}{\sqrt{2}} \sin 2\theta^* \cos \phi^* - \sqrt{2}\text{Im}\{\rho_{10}\} \sin \theta^* \sin \phi^*\right]. \tag{A.6}$$

This can be further simplified by integrating over ϕ^*[1]

$$I(\cos \theta^*) = \frac{3}{2} \left[\frac{1}{4}(1 + \cos^2 \theta^*) + \frac{\rho_{00}}{4}(1 - 3\cos^2 \theta^*)\right]. \tag{A.7}$$

[1]It is valid to integrate the angular distribution over ϕ^* because the effective acceptance of the

157

Defining the polarization $\alpha = \frac{1-3\rho_{00}}{1+\rho_{00}}$, we obtain the angular distribution:

$$I(\cos\theta^*) = \frac{3}{2(\alpha+3)}(1 + \alpha\cos^2\theta^*). \tag{A.8}$$

An unpolarized ψ would have $\alpha = 0$ whereas $\alpha = 1$ and -1 correspond to fully transverse and longitudinal polarizations. The angular distributions for these three different values of polarizations are shown in Figure A-2. Note that these distributions correspond to the generated ones, i.e. they do not include the effective acceptance of the kinematic requirements of the analysis. The effect of the acceptance on the angular distribution is discussed in Section 4.4.
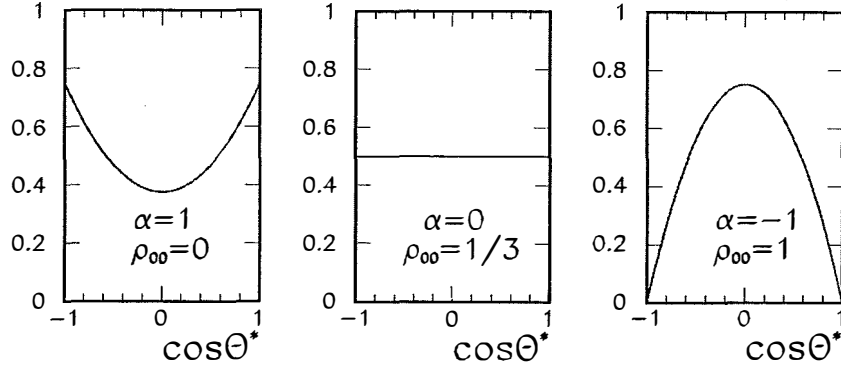
Figure A-2: The $\cos\theta^*$ angular distributions for $\alpha = 1, 0$, and -1.

kinematic requirements of the analysis is checked to not introduce residual ϕ^* dependence after integration. Due to the periodic symmetry of the effective acceptance in ϕ^*, the integral of the $\cos\phi^*$ term with the acceptance applied vanishes. The integrals of the $\cos 2\phi^*$ and $\sin\phi^*$ terms with the acceptance applied do not vanish. But the former is found to be negligibly small and the latter does not depend on ϕ^*.

Appendix B

Level 2 Dimuon Triggers

The following is a description of the four Level 2 dimuon triggers that constitute the data sample for this analysis.

- CMU_CMU_ONE_CFT_1A: Run 1A trigger. Required one Level 2 CMU cluster[1], with a second Level 1 CMU stub. This trigger was dynamically prescaled, as a function of the instantaneous luminosity.

- CMU_CMU_TWO_CFT_1B: Run 1B trigger. Required two Level 2 CMU clusters which must be noncontiguous. If one cluster is in the $+z$ region of the CDF detector and the other cluster is in the $-z$ region, then the two clusters are required to have different ϕ values. This trigger was not prescaled.

- CMU_CMU_ONE_CFT_1B: Run 1B trigger. Required one Level 2 CMU cluster, with a second Level 1 CMU stub. This trigger was dynamically prescaled, and had a higher nominal P_T threshold than the CMU_CMU_ONE_CFT_1A.

- CMU_CMU_SIX_TOW_1B: Run 1B trigger. Required one Level 2 CMU cluster which was formed by merging two adjacent CMU clusters together. The resulting single cluster spanned six or more calorimeter towers. This trigger was

---

[1]A Level 2 muon cluster consists of a Level 1 muon stub with a matched CFT track and the associated calorimeter towers.

dynamically prescaled. The original motivation was to compensate for losses due to the non-contiguity requirement imposed in the CMU_CMU_TWO_CFT_1B.

Appendix C

Testing the χ^2 Fitter with a Toy Monte Carlo

To test the χ^2 fitter (Section 6.1), toy Monte Carlo samples generated with known values of polarization are fed into the fitter. The distributions of the fitted polarizations and their pulls are examined. The pull is defined as the difference between the input polarization and the fitted value divided by the error from the fit. Any bias would clearly reflect biases in the fitting procedure.

For simplicity, only one type of signal (prompt) is used. This means both k and p_k are set to 1 in Section 6.1. Signal toy Monte Carlo events are generated with mass equal to 3.686 GeV/c^2, the world-average[5] value of the $\psi(2S)$ mass, and $\cos\theta^*$ according to the angular distribution with a known polarization α:

$$\omega(\cos\theta^*; \alpha) = \frac{3}{2(3+\alpha)}(1 + \alpha\cos^2\theta^*).\tag{C.1}$$

Background events are generated with a flat distribution in mass, and with $\cos\theta^*$ distributed according to an angular distribution:

$$\omega_B(\cos\theta^*; a, b) = \frac{1}{2}[1 + aP_2(\cos\theta^*) + bP_4(\cos\theta^*)],\tag{C.2}$$

where $P_2(\cos\theta^*)$ and $P_4(\cos\theta^*)$ are the Legendre polynomials:

$$P_2(\cos\theta^*) = \frac{1}{2}(3\cos^2\theta^* - 1)\tag{C.3}$$

161

$$P_4(\cos\theta^*) = \frac{1}{8}(35\cos^4\theta^* - 30\cos^2\theta^* + 3). \tag{C.4}$$

The parameters a and b are obtained from fitting the $\cos\theta^*$ distribution in data side-bands and found to have values of 1.71 and 0.65 respectively. Only even Legendre polynomials are used as the background $\cos\theta^*$ distribution is observed to be symmetric about 0. The $\cos\theta^*$ distributions are further sampled according to the acceptance histograms, displayed in Figure C-1. The acceptance histograms are obtained from full Monte Carlo simulations with detector simulation, as described in Chapter 4. The $d\sigma/dP_T$ from Run 1A $\psi(2S)$ cross section analysis is used as the input P_T spectrum for signal, and a P_T parameterization of $\psi(2S)$ candidates in data sidebands is used for background. The events passing the selection cuts are then binned in $\cos\theta^*$ to form the effective acceptance parameterizations.

The signal and background distributions are generated to have the same total number of events (4212 for the integrated P_T range) in the signal region and side-bands as in the data. The relative composition is simulated by using the $\psi(2S)$ signal fraction ($f_S = 0.53$) measured in the data. A sideband subtraction in $\cos\theta^*$ is performed to determine this $\psi(2S)$ candidate yield. The uncertainties in the sidebands and signal region are propagated and used as the measurement error σ in the χ^2 fitter.

Due to the acceptance, bins at large $|\cos\theta^*|$ have few events. This can induce a bias in the fit as the number of events will start to deviate from being Gaussian distributed. It also implies that the square root of the number of events may no longer be a good estimate of the event yield uncertainty. We try to reduce this "non-Gaussian" effect by using the corresponding 1 sigma error in the Poisson distribution function as the event yield uncertainty.

One thousand experiments for each α $(1, 0.5, 0, -0.5, -1)$ with fixed values of $a = 1.71$ and $b = 0.65$ are generated and fitted with the χ^2 fitter.

The distributions of the α_{Fitted} and the pull are shown in Figure C-2 and C-3 respectively. They are fitted to a Gaussian distribution,

$$\frac{N}{\delta x\sqrt{2\pi}\sigma}\exp\left[-\frac{1}{2}(\frac{x-\mu}{\sigma})^2\right] \tag{C.5}$$

where x can stand for either α_{Fitted} or the pull, and δx is the bin width of the

corresponding distribution. The parameters N, μ, and σ are the area, the mean, and the width of the Gaussian distribution respectively. The fitted values of these parameters for the α_{Fitted} and the pull distributions are listed in Tables C.1 and C.2. The mean of α_{Fitted} shows a negative bias which increases as α increases. The worst case ($\alpha = 1$) is about 3σ low. But the absolute bias is an order of magnitude smaller than the r.m.s.. The mean values of the pull distributions also reflect a negative bias. The widths are consistent with 1, indicating an overall proper estimate of the fit error.

Compared with the large statistical uncertainty in α, the bias we see from the toy Monte Carlo tests is negligibly small.

α_{input}	N	μ	σ
1.0	955.1±31.1	0.94±0.02	0.54±0.01
0.5	964.7±31.1	0.45±0.02	0.47±0.01
0.0	974.4±31.3	-0.02±0.02	0.46±0.01
-0.5	967.4±31.1	-0.53±0.01	0.40±0.01
-1.0	983.7±31.4	-0.99±0.01	0.35±0.01

Table C.1: Results of fitting the α distributions from the toy Monte Carlo experiments to a Gaussian. The "α_{input}" column represents the five different input values of the polarization used in the experiments. The parameters N, μ, and σ correspond to the area, the mean, and the width of the Gaussian.
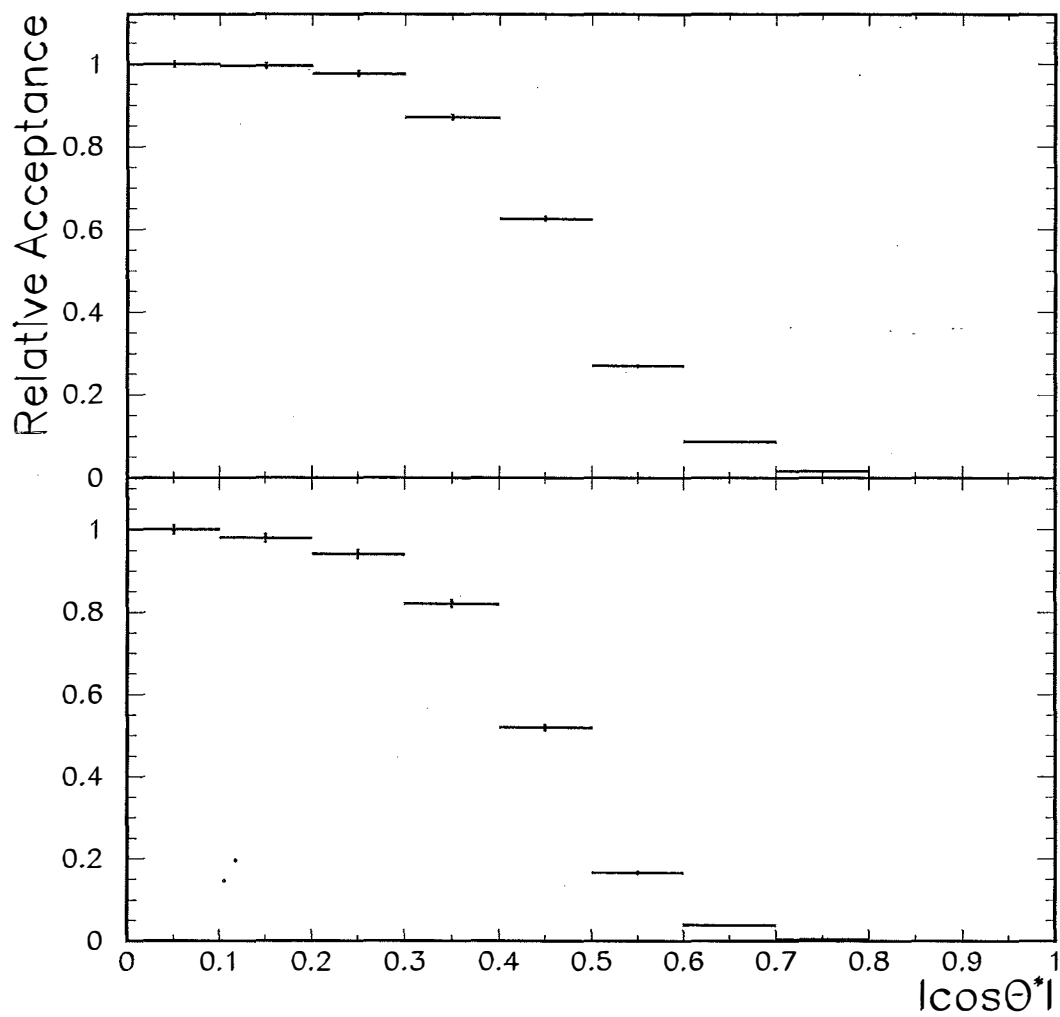
Figure C-1: Effective signal acceptance(top) and background acceptance in side-bands(bottom).
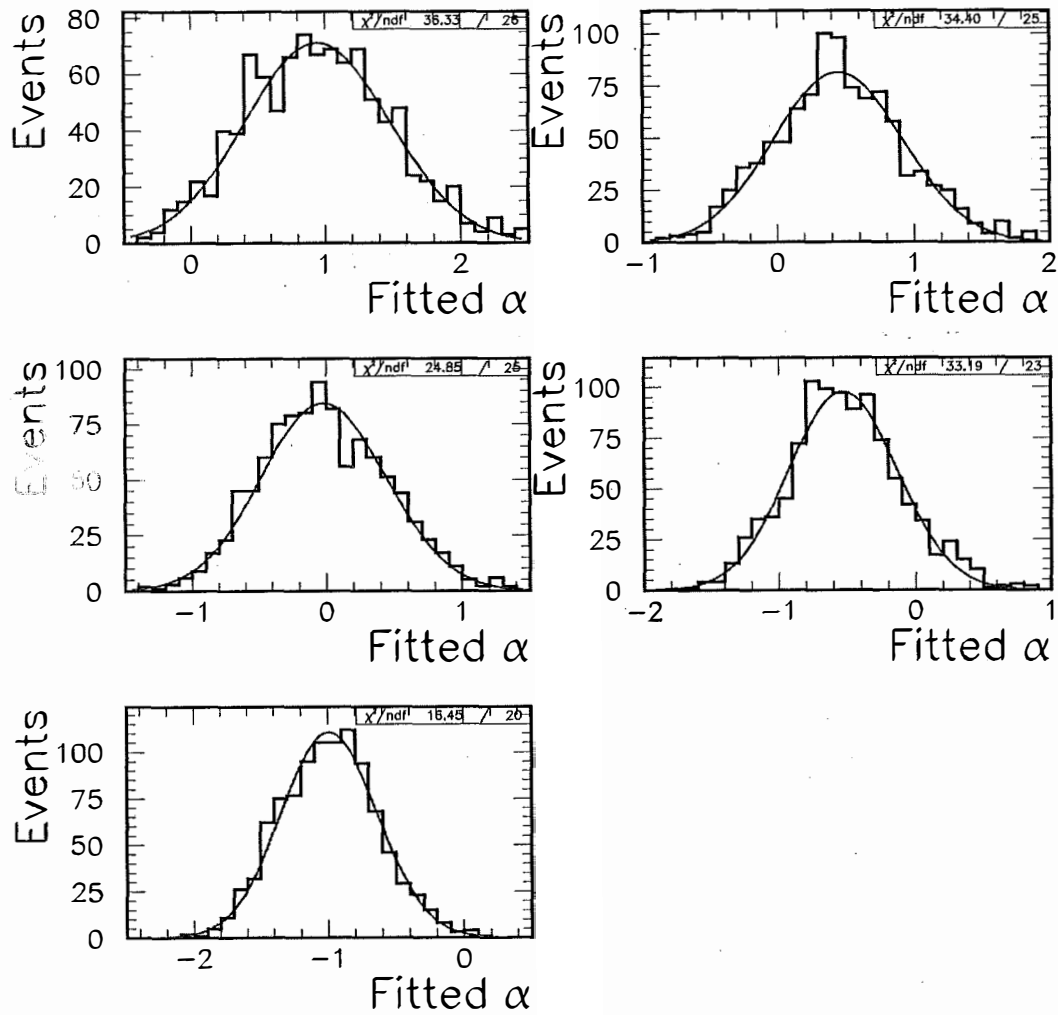
Figure C-2: Fitted α distributions for different values of polarization(α=1, 0.5, 0, -0.5, -1).
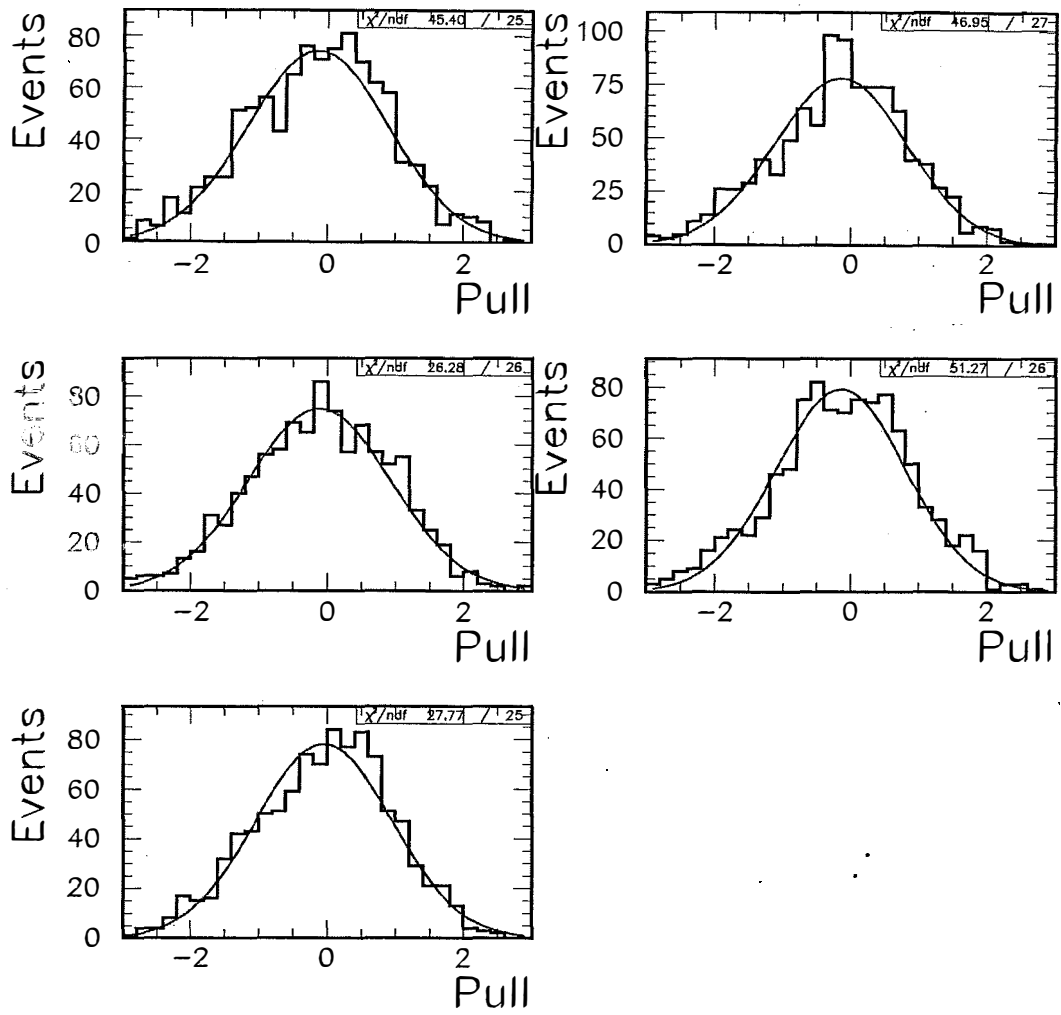
Figure C-3: Pull distributions for different values of polarization(α=1, 0.5, 0, -0.5, -1).

α_{input}	N	μ	σ
1.0	955.8±31.1	-0.14±0.03	1.03±0.03
0.5	950.1±30.9	-0.15±0.03	0.97±0.03
0.0	972.5±31.3	-0.12±0.03	1.04±0.03
-0.5	943.8±30.8	-0.15±0.03	0.95±0.03
-1.0	971.3±31.3	-0.04±0.03	0.99±0.02

Table C.2: Results of fitting the pull distributions from the toy Monte Carlo experiments to a Gaussian. The "α_{input}" column represents the five different input values of the polarization used in the experiments. The parameters N, μ, and σ correspond to the area, the mean, and the width of the Gaussian.

Bibliography

[1] J. Aubert et al., Phys. Rev. Lett. **33**, 1406 (1974).

[2] J. Augustin et al., Phys. Rev. Lett. **33**, 1404 (1974).

[3] S. Glashow, J. Iliopoulos, and L. Maiani, Phys. Rev. D **2**, 1285 (1970).

[4] G. Abrams et al., Phys. Rev. Lett. **33**, 1452 (1974).

[5] C. Caso et al., Eur. Phys. J. C **15**, 1 (2000).

[6] E. Braaten, S. Fleming, and T.C. Yuan, Ann. Rev. Nucl. Part. Sci. **46**, 197 (1996).

[7] K. Byrum, Proceedings of the XXVII International Conference on High Energy Physics (1994);
T. Daniels, Proceedings of the Eighth Meeting of the Division of Particles and Fields of the American Physical Society (hep-ex/9412013).

[8] CDF Collaboration, F. Abe et al., Phys. Rev. Lett. **79**, 572 (1997);
T. Daniels, Ph.D. dissertation, Massachusetts Institute of Technology, (1997).

[9] C.-H. Chang, Nucl. Phys. B **172**, 425 (1980);
R. Baier and R. Rückl, Phys. Lett. B **102**, 364 (1981);
R. Baier and R. Rückl, Zeit. Phys. C **19**, 251 (1983).

[10] R. Barbieri, R. Gatto, and E. Remiddi, Phys. Lett. B **61**, 465 (1976);
R. Barbieri, M. Caffo, and E. Remiddi, Nucl. Phys. B **192**, 61 (1981).

[11] E. Braaten and T. Yuan, Phys. Rev. Lett. **71**, 1673 (1993);
E. Braaten and T. Yuan, Phys. Rev. D **52**, 6627 (1995).

[12] J.C. Collins and D.E. Soper, Ann. Rev. Nucl. Part. Sci. **37**, 383 (1987).

[13] M. Cacciari and M. Greco, Phys. Rev. Lett. **73**, 1586 (1994);
E. Braaten, M.A. Doncheski, S. Fleming, and M. Mangano, Phys. Lett. B **333**, 548 (1994);
D.P. Roy and K. Sridhar, Phys. Lett. B **339**, 141 (1994).

[14] I. Rothstein, hep-ph/9911276 (1999).

[15] G.T. Bodwin, E. Braaten, and G.P. Lepage, Phys. Rev. D **46**, 1914 (1992);
G.T. Bodwin, E. Braaten, T.C. Yuan, and G.P. Lepage, Phys. Rev. D **46**, 3703 (1992).

[16] W.E. Caswell and G.P. Lepage, Phys. Lett. B **167**, 437 (1986).

[17] G.T. Bodwin, E. Braaten, and G.P. Lepage, Phys. Rev. D **51**, 1125 (1995), Erratum ibid. **55**, 5853 (1997).

[18] G.A. Schuler, Int. J. Mod. Phys. A **12**, 3951 (1997).

[19] E. Braaten and S. Fleming, Phys. Rev. Lett. **74**, 3327 (1995).

[20] P. Cho and A.K. Leibovich, Phys. Rev. D **53**, 6203 (1996).

[21] M. Beneke and M. Krämer, Phys. Rev. D **55**, 5269 (1997).

[22] G.T. Bodwin, D.K. Sinclair, and S. Kim, Phys. Rev. Lett. **77**, 2376 (1996).

[23] M.A. Sanchis-Lozano, hep-ph/9907497 (1999).

[24] M. Cacciari and M. Krämer, Phys. Rev. Lett. **76**, 4128 (1996).

[25] H1 Collaboration, S. Aid et al., Nucl. Phys. B **472**, 3 (1996).

[26] ZEUS Collaboration, J. Breitweg et al., Z. Phys. C **76**, 599 (1997).

[27] B.A. Kniehl and G. Kraemer, Eur. Phys. J. C **6**, 493 (1999).

[28] K. Sridhar, A.D. Martin, and W.J. Stirling, Phys. Lett. B **438**, 211 (1998).

[29] M. Beneke, I.Z. Rothstein, and M.B. Wise, Phys. Lett. B **408**, 373 (1997).

[30] H. Fritzsch, Phys. Lett. B **67**, 217 (1977);
F. Halzen, Phys. Lett. B **69**, 105 (1977);
F. Halzen and S. Matsuda, Phys. Rev. D **17**, 1344 (1978);
M. Gluck, J. Owens, and E. Reya, Phys. Rev. D **17**, 2324 (1978).

[31] J.F. Amundson, O.J.P. Eboli, E.M. Gregores, and F. Halzen, Phys. Lett. B **390**, 323 (1997); Phys. Lett. B **372**, 127 (1996);
O.J.P. Eboli, E.M. Gregores, and F. Halzen, Phys. Lett. B **451**, 241 (1999).

[32] NA14 Collaboration, R. Barate et al., Z. Phys. C **33**, 505 (1987);
P. Roudeau (NA14), Nucl. Phys. Proc. Suppl. B **7**, 273 (1989).

[33] P. Nason, S. Dawson, and R.K. Ellis, Nucl. Phys. B **303**, 607 (1988); **327**, 49 (1989).

[34] B.A. Kniehl and G. Kramer, Phys. Rev. D **60**, 014006 (1999).

[35] J. Binnewies, B.A. Kniehl, and G. Kramer, Phys. Rev. D **58**, 034016 (1998).

[36] C. Peterson, D. Schlatter, I. Schmitt, and P.M. Zerwas, Phys. Rev. D **27**, 105 (1983).

[37] CLEO Collaboration, R. Balest et al., Phys. Rev. D **52**, 2661 (1995).

[38] H.L. Lai, J. Huston, S. Kuhlmann, F. Olness, J. Owens, D. Soper, W.K. Tung, and H. Weerts, Phys. Rev. D **55**, 1280 (1997).

[39] A.D. Martin, R.G. Roberts, W.J. Stirling, and R.S. Thorne, Eur. Phys. J. C **4**, 463 (1998); Phys. Lett. B **443**, 301 (1998).

[40] A. Brandenburg, O. Nachtmann, and E. Mirkes, Z. Phys. C **60**, 697 (1993).

[41] C. Biino et al., Phys. Rev. Lett. **58**, 2523 (1987);

   E537 Collaboration, C. Akerlof et al., Phys. Rev. D **48**, 5067 (1993);

   J.G. Heinrich, et al., Phys. Rev. D **44**, 1909 (1991).

[42] P. Cho and M.B. Wise, Phys. Lett. B **346**, 129 (1995).

[43] M. Beneke and I.Z. Rothstein, Phys. Lett. B **372**, 157 (1996), Erratum ibid. **389**, 789 (1996).

[44] E. Braaten, B.A. Kniehl, and J. Lee, hep-ph/9911436 (1999).

[45] S. Fleming, O.F. Hernandez, I. Maksymyk, and H. Nadeau, Phys. Rev. D **55**, 4098 (1997).

[46] S. Fleming and I. Maksymyk, Phys. Rev. D **54**, 3608 (1996).

[47] M.A. Sanchis-Lozano and B. Cano-Coloma, hep-ph/9611264.

[48] M. Beneke and I.Z. Rothstein, Phys. Rev. D **54**, 2005 (1996); **54**, 7082 (1996).

[49] G. Carron et al., Stochastic Cooling Tests in ICE, Phys. Lett. B **77**, 353 (1978);

   D. Möhl, G. Petrucci, L. Thorndahl, and S. van der Meer, Physics and Technique of Stochastic Cooling, Phys. Rep. **58**, 73 (1980);

   S. van der Meer, Stochastic Cooling in the CERN Antiproton Accumulator, IEEE Trans. Nucl. Sci. **28**, 1994 (1981).

[50] CDF Collaboration, F. Abe et al., Nucl. Inst. and Meth. A **271**, 387 (1988) and references therein.

[51] S. Tkaczyk et al., The CDF Silicon Vertex Detector, Nucl. Inst. Meth. A **342**, 240 (1994);

   D. Amidei et al., The Silicon Vertex Detector of the Collider Detector at Fermilab, Nucl. Inst. Meth. A **350**, 73 (1994);

   P. Azzi et al., SVX', the New CDF Silicon Vertex Detector, Nucl. Inst. Meth. A **360**, 137 (1995).

[52] C. Newman-Holmes et al., Measurement of the Magnetic Field of the CDF Magnet, Nucl. Inst. Meth. A **274**, 443 (1989).

[53] F. Bedeschi et al., Design and Construction of the CDF Central Tracking Chamber, Nucl. Inst. Meth. A **271**, 35 (1988).

[54] G. Ascoli et al., CDF Central Muon Detector, Nucl. Inst. Meth. A **271**, 218 (1988).

[55] D. Frei, Multiple Scattering of Central Muons, CDF Note 1430 (1991).

[56] CDF Collaboration, F. Abe et al., Phys. Rev. D **50**, 5550 (1994).

[57] G.W. Foster, et al., A Fast Hardware Track Finder for the CDF Central Tracking Chamber, Nucl. Inst. Meth. A **271**, 277 (1988).

[58] C.E. Anway-Wiese, Offline Muon Matching Cuts, CDF Note 1986 (1993).

[59] J.P. Marriner, Secondary Vertex Fit with (optional) Mass Constraints and (optional) Pointing Constraints, CDF Note 1996 (1993).

[60] P. Avery, K. Read, and G. Trahern, QQ: A Monte Carlo Generator, Internal Software Note CSN-212, Cornell University, (1985);
J.D. Lewis and P. Avery, CLEOMC: The CDF Interface to the CLEO Monte Carlo (QQ), CDF Note 2724 (1994).

[61] M. Shapiro et al., A User's Guide to QFL, CDF Note 1810 (1992).

[62] S.P. Pappas, DIMUTG: Dimuon Trigger Simulation for Run 1B, CDF Note 3537 (1996).

[63] A. Warburton, Ph.D. dissertation, University of Toronto, (1997).

[64] S.P. Pappas, J.D. Lewis, and G. Michail, Run 1B Low P_T Central Dimuon Trigger Efficiencies, CDF Note 4076 (1997).

[65] J.D. Lewis and K.T. Pitts, A Summary of CFT Operation in Run 1, CDF Note 3999 (1997).

[66] F. DeJongh, Level 3 Dimuon Efficiency for Run 1A, CDF Note 1984 (1993).

[67] H. Wenzel et al., Beamlines, CDF Note 3334 (1995);
H. Wenzel, The Primary Interaction Vertex, CDF Note 4066 (1997).

[68] CDF Collaboration, F. Abe et al., Phys. Rev. Lett. **71**, 3421 (1993);
CDF Collaboration, F. Abe et al., Phys. Rev. D **57**, 5382 (1998).

[69] F. James and M. Roos, "MINUIT" A System for Function Minimization and Analysis of the Parameter Errors and Correlations, Comput. Phys. Commun. **10**, 343 (1975).

[70] R. Cropp et al., A measurement of prompt J/ψ polarization, CDF Note 5029 (1999).

[71] G. Bauer et al., Measurement of the J/ψ Polarization from an Analysis of the decay $J/\psi \to \mu^+\mu^-$, CDF Note 5030 (1999).

[72] J.K. Mizukoshi, hep-ph/9911384.

[73] CDF Collaboration, F. Abe et al., FERMILAB-Pub-96/390-E (1996).

[74] G. Feild et al., Upsilon Cross Section Measurements in Run 1B. CDF Note 5027 (1999).

[75] D0 Collaboration, B. Abbott et al., FERMILAB-Pub-96/357-E (1996).

[76] S. Baek, P. Ko, J. Lee, and H.S. Song, Phys. Rev. D **55**, 6839 (1997).

[77] E. Braaten and Y-Q. Chen, Phys. Rev. Lett. **76**, 730 (1996).

[78] M. Beneke, M. Kramer, and M. Vanttinen, Phys. Rev. D **57**, 4258 (1998).

[79] T. Mehen and S. Fleming, Phys. Rev. D **57**, 1846 (1998).

[80] S.U. Chung, Spin Formalisms, CERN 71-8.